DISSERTATION

submitted to the

Faculty of Chemistry and Earth Sciences

of the University of Heidelberg, Heidelberg, Germany

in partial fulfilment of the requirements for the degree of

Doctor of Natural Sciences (Dr. rer. nat.)

submitted by

Viktoriia Nedashkivska (M.Sc. Physics)

born in Kyiv, Ukraine

Supervisor: Dr. Pavel A. Levkin and Prof. Dr. Michael Grunze

Oral examination: 21 November 2014

DISSERTATION

Zur Erlangung der Doktorwürde

Der Naturwissenschaftlich-Mathematischen

Gesamtfakultät der

Ruprecht-Karls-Universität Heidelberg

vorgelegt von

Viktoriia Nedashkivska (M.Sc. Physics)

Geboren in Kiew, Ukraine

Supervisor: Dr. Pavel A. Levkin und Prof. Dr. Michael Grunze

Tag der mündlichen Prüfung: 21 November 2014

Preparation, characterization and applications of micro-rough polymethacrylate surfaces

This dissertation was carried out at the

Department of Applied Physical Chemistry

Heidelberg University

Referees:

Prof. Dr. Michael Grunze

Prof. Dr. Hans-Robert Volpp

Abstract

Superhydrophobic surfaces have numerous important practical applications in research and industry. These materials have been widely used for production of self-cleaning, anti-icing, anti-corrosive, non-adhesive, anti-biofouling coatings and surfaces. The phase separation method of producing porous polymer films is a simple and cheap approach that allows producing materials with desired physical and chemical properties, such as polymer globule size, porosity, hydrophobicity or hydrophilicity and surface functional groups. Additionally, the surface can be also later functionalized using available surface modification techniques. However, so far, due to the not optimal surface topography the produced surfaces have exhibited large contact angle hysteresis which limits their practical applications. The goals of this PhD thesis were to: (1) develop a method for the preparation of superhydrophobic polymer surfaces with high water contact angles and low contact angle hysteresis; (2) to characterize the produced surfaces; (3) to investigate the effect of the surface topography and hierarchy on the surface wettability; (4) and to explore their properties in microfluidic and biological applications.

The task to design surfaces with outstanding surface characteristics requires understanding of the influence of the surface topography on the wettability. Due to the ease of production, porous poly(2-hydroxyethylmethacrylate-*co*-ethylene dimethacrylate) (polyHEMA) and poly(butyl methacrylate-*co*-ethylene dimethacrylate) (polyBMA) surfaces with different surfaces topographies prepared for these studies. The polymer surfaces with protruded and grooved surface topography were prepared simultaneously by photopolymerization in a mold consisting of two glass slides. However, due to the breakage of the polymer film during separation, surfaces with characteristic protruded and grooved topography were made. Photografting of the polyHEMA surfaces with 2,2,3,3,3-pentafluoropropyl methacrylate (PFPMA) resulted in the formation of a complex hierarchical structure. The surface functional groups of polyHEMA could be modified through consecutive esterification and thiol-yne reaction. Influence of the surface topography, hierarchy and chemistry on the surface wettability were investigated by Scanning Electron Microscopy (SEM), confocal optical profiler and water contact angle measurements.

Recently, microfluidic devices attracted a lot of attention as they allow handling of small liquid volumes and miniaturization of the measurement systems. In this thesis, open microfluidic channels based on the Laplace micro-pump were prepared by photografting PFPMA on the grooved polyHEMA surface creating superhydrophilic micro-channel surrounded by superhydrophobic borders. The working principle of the passive Laplace micro-pump in the produced micro-channel was investigated. The formation of a laminar flow in the absence of an external force was studied. Additionally, the kinetics of the flow in the micro-channels with different dimension was examined.

The ability to control stem cell differentiation shows great promise for numerous applications such as stem cell therapy, treatment of diabetes, Parkinson and Alzheimer diseases and many other. However, it is a complex process that depends on both the physical and chemical cues. In this thesis, polyHEMA surfaces with different roughness and surface chemistry were used to investigate the influence of the surface

properties on the stem cell differentiation. Retardation of stem cell differentiation for over three weeks of culture on the micro-rough surfaces was shown.

Zusammenfassung

Superhydrophobe Oberflächen finden zahlreiche wichtige Anwendungen in der Forschung und Industrie. Sie werden vielfach für die Herstellung von selbstreinigenden, Anti-Eis-, Anti-Korrosions-Beschichtungen, nicht-klebendenden und Anti-Fouling-Beschichtungen und -oberflächen verwendet. Die Phasentrennungsmethode zur Herstellung von porösen Polymerfilmen ist einfach und preiswert. Mit Hilfe dieser Methode können die physikalischen und chemischen Eigenschaften von Materialien eingestellt werden. So zum Beispiel die Größe der Polymerglobuli, die Porosität, Hydrophobizität oder Hydrophilizität und die funktionellen Gruppen an einer Oberfläche. Darüber hinaus kann die Oberfläche später auch noch mit zur Verfügung stehenden Oberflächenmodifikationsmethoden funktionalisiert werden. Allerdings zeigen die bisher hergestellten Oberflächen eine starke Kontaktwinkelhysterese, aufgrund einer nicht optimale Oberflächentopographie, die den praktischen Einsatz dieser Oberflächen limitiert. Im Rahmen der vorliegenden Doktorarbeit sollten: 1. eine Methode zur Herstellung von Polymeroberflächen mit hohen Wasserkontaktwinkeln und geringer Kontaktwinkelhysterese entwickelt werden, 2. die hergestellten Oberflächen charakterisiert werden, 3. der Effekt der Oberflächentopographie und -hierarchie auf das Benetzungsverhalten der Oberfläche untersucht werden und 4. ihre Eigenschaften in mikrofluidischen und biologischen Anwendungen erforscht werden.

Es besteht eine große Nachfrage nach Oberflächen mit herausragenden Oberflächeneigenschaften. Aufgrund ihrer einfachen Herstellbarkeit wurden poröse Poly(2-hydroxyethylmethacrylat-co-ethylen dimethacrylat) (polyHEMA) und Poly(butyl methacrylat-co-ethylen dimethacrylat) (polyBMA) Oberflächen mit verschiedenen Oberflächentopographien für die vorliegenden Studien durch das "lift-off" Verfahren hergestellt. Die Polymeroberflächen mit Erhebungen und Furchen wurden parallel in nur einem Formwerkzeug bestehend aus zwei Glasobjektträgern durch Photopolymerisation hergestellt. Diese Polymeroberflächen mit Erhebungen und Furchen entstehen, da der Polymerfilm durch die Teilung (der Objektträger) bricht. Photografting der polyHEMA Oberflächen mit 2,2,3,3,3-Pentafluoropropyl methacrylat (PFPMA) führte zur Bildung von komplexen hierarchischen Strukturen. Die funktionellen Gruppen der polyHEMA Oberfläche konnten durch Veresterung und eine anschließende Thiol-Alkin-Reaktion modifiziert werden.

Der Einfluss der Oberflächentopographie, -hierarchie und –chemie auf das Benetzungsverhalten der Oberfläche wurde mit Rasterkraftelektronenmikroskopie (REM), Rauigkeits- und Wasserkontaktwinkelmessungen untersucht. In letzter Zeit haben mikrofluidische Geräte große Aufmerksamkeit auf sich gezogen, da sie die Handhabung kleinster Volumina und die Miniaturisierung von Messsystemen erlauben. In dieser Arbeit wurden offene mikrofluidische Kanäle basierend auf der Laplace Mikropumpe durch Photografting von PFPMA an die polyHEMA Furchen präpariert. Dadurch entstanden superhydrophile Mikrokanäle umgeben von superhydrophoben Grenzen. Das Arbeitsprinzip der passiven Laplace Mikropumpe wurde in den hergestellten Mikrokanälen untersucht. Es konnten sowohl die Erzeugung eines Flusses ohne äußere Kraft als auch die Bildung eines laminaren und Aufwärtsflusses gezeigt

werden. Desweiteren wurde die Kinetik des Flusses in Mikrokanälen mit verschiedenen Dimensionen untersucht.

Die Stammzelldifferenzierung ist in zahlreichen Anwendungen wichtig, wie z.B. der Zelltherapie, der Behandlung von Diabetes, Parkinson, Alzheimer und viele mehr. Es ist jedoch ein komplexer Prozess, der sowohl von physikalischen als auch von chemischen Reizen abhängt. In dieser Arbeit wurde der Einfluss der Oberflächenrauigkeit und –chemie auf die Stammzellendifferenzierung untersucht. Dazu wurden polyHEMA Oberflächen mit unterschiedlicher Rauigkeit und Oberflächenchemie eingesetzt. Ebenso wurde die Verzögerung der Differenzierung der Stammzellen zu mehr als drei Wochen der Kultivierung auf den mikrorauen Oberflächen wurde gezeigt.

Acknowledgements

This work was performed in the group of Dr. Pavel Lavekin, at the Institute of Toxicology and Genetics (ITG) at the Karlsruhe Institute of Technology (KIT) Campus North in Eggenstein-Leopoldshafen and Applied Physical Chemistry, Heidelberg University. It was funded through the Helmholtz Association's Initiative and Networking Fund (grant VH-NG-621).

I am grateful to all the people without whom this work would not have been possible:

To Dr. Pavel Levkin, for the numerous heated discussions, for providing me the opportunity to work on this interesting project and expanding my knowledge in the completely new to me fields.
To my advisor Prof. Dr. Michael Grunze, I am appreciative of the constant support, the constructive and always enlightening scientific discussions that brought me closer to the finishing of this work, and finally for the review of this thesis. Many thanks also to Prof. (apl.) Dr. Hans-Robert Volpp, for kindly agreeing to be the second referee of this work.
To my lab members: Linxian Li, Junsheng Li, Alexander Efremov, Erica Ueda, Girish Shankar, Xin Du, Wenquian Feng, Anna Popova, Danuta Kuzmich and Konstantin Demir for the support and shared experience of working together. I am particularly grateful to Junsheng for his time and help with running experiments, to Alexander for his innovative ideas and collaborative work, and for countless discussions.
To Dr. Ping Zhang, for being an excellent collaborator as well as for his time and effort for running cell experiments.
To Mona Jaggy and Dr.Tatjana Austenreich, for their collaborative work, helpful discussions and expertise in the stem cell field.
To my other collaborators over the years: Dr. Jörg Overhage, Nikola Strempel, Janine Strehmel from IFG institute in KIT.

Finally, I would like to thank my family and friends for their constant support and motivation, especially in the hard times. I am glad that you are part of my life.

List of Figures

Figure 1.1: Schematic depiction of water contact angle and contact angle hysteresis 1
Figure 1.2: SEM images of surface morphology of plants 2
Figure 1.3: Theoretical models of surface wetting 3
Figure 1.4: The apparent contact angle dependence on the intrinsic contact angle 5
Figure 1.5: Transition from Cassie-Baxter to Wenzel state 6
Figure 1.6: Droplet advancing from rough spot onto a smooth field 7
Figure 1.7: Morphology and water contact angles of hierarchical surfaces 9
Figure 1.8: Apparent contact angles for Wenzel and Cassie-Baxter states vs roughness geometry parameters 10
Figure 1.9: Schematic description of the two-step moulding approach via capillary force lithography 12
Figure 1.10: Schematic example of the self-assembly process and the produced surface. 12
Figure 2.1: Structures of the modification and fluorination chemicals. 15
Figure 2.2: Scheme of the activation, modification, and fluorination of the glass plates. 15
Figure 2.3: Chemical structure of the utilized polymerization initiators, porogens, monomers, and cross-linker. 16
Figure 2.4. Scheme of the initiation process by DMPAP and polymerization of HEMA and EDMA 18
Figure 2.5: Schematic description of the polymer film preparation in the mold by the UV-initiated photopolymerization 18
Figure 2.6: Scheme of an initiation process by benzophenone and photografting of the polyHEMA surfaces with PFPMA 19
Figure 2.7: Schematic description of the chemical modification of the grooved spolyHEMA surfaces with alkyne, 1-decanethiol, cysteamine, 1H,1H,2H,2H-perfluorodecanethiol. 20
Figure 3.1: Examples bicontinuous structure and porous polymer film prepated by phase separation process.. 25
Figure 3.2: Surface morphology images by SEM of the protruded and grooved polyHEMA surfaces 27
Figure 3.3: Surface linear profile showing height deviations relative to the mean line for protruded and grooved polyHEMA surfaces 29
Figure 3.4: Smooth polyHEMA surface characterization by SEM and WCA measurement. 30
Figure 3.5: Photographs of water droplets spreading and adsorbing on the protruded and grooved polyHEMA surfaces. 31

Figure 3.6: Smooth polyHEMA surface characterization after photografting with PFPMA 31
Figure 3.7: SEM images of protruded and grooved polyHEMA surfaces before and after photografting with PFPMA 32
Figure 3.8: Comparison of the wettability of protruded and grooved polyHEMA surfaces after photografting with PFPMA. 33
Figure 3.9: Comparison of the wettability of protruded and grooved polyBMA surfaces. 35
Figure 3.10: SEM images of the grooved polyHEMA surface 1-decanethiol modified and perfluorodecanethiol modified, photografted with PFPMA 37
Figure 3.11: Topography maps of the grooved polyHEMA surfaces. 39
Figure 3.12: Dependence of the average surface roughness of the grooved polyHEMA surfaces on the 1-decanol content in the polymerization mixture 39
Figure 3.13: Particle size distribution for grooved polyHEMA surfaces.....40
Figure 3.14: Dependence of the polymer globule size of the grooved polyHEMA surfaces on the 1-decanol content in the polymerization mixture.....41
Figure 3.15: Topography maps of the smooth polyHEMA surface before and after photografting with PFPMA. 42
Figure 3.16 Topography maps of the grooved HC polyHEMA surface before and after photografting with PFPMA.. 42
Figure 3.17: Schematic description of the Laplace pump system. 44
Figure 3.18: Images showing the flow of rhodamine solution in the linear 1000 μm wide channel and S-channel 1000 μm wide channel. 46
Figure 3.19: Images showing the upwards flow of rhodamine solution in the micro-channel with tilt angle of ~14° 46
Figure 3.20: Images of the T-channel with 10 mm circular outlet the simultaneous addition of the rhodamine and water and creation of the laminar flow 48
Figure 3.21: Images of the liquid flow in the micro-channels with 5 inlets and 10 cm circular outlet of three and five water dye solutions mixing 49
Figure 3.22: Schematic depiction of the measurement of flow velocity.....50
Figure 3.23: Graphs of the dye flow velocity in the channels with 5 cm length, 1000 μm width and outlet circle of 5mm, 10mm, 15 mm. 51
Figure 3.24: Graphs of the dye flow velocity in the channels for micro-channel with 10 mm outlet circle for 500 μm and 1000 μm channel width for different dye solution volumes 52
Figure 3.25: Initial flow velocity of the dye for micro-channel with 10 mm outlet circle for 500 μm and 1000 μm channel width.....53
Figure 3.26: Actin cytoskeleton-focal adhesion feedback loop and schematic description of the cell movement.. 55

Figure 3.27: Topograpy maps of polyHEMA micro-rough, nano-rough, smooth surfaces. 58
Figure 3.28: The fluorescent microscopy images and respective quantification of cross-contamination between MLTy-mCherry and HeLa-EGFP cultured in adjacent rectangles for 3 days. 59
Figure 3.29: Time-lapse images of HeLa-EGFP cell colony on the micro-rough polyHEMA surfaces in superhydrophobic border vicinity.. 59
Figure 3.31: Five examples of the travelled cell paths (HeLa-EGFP) on the nano-rough, micro-rough and Petri dish surfaces. Comparison of the path length, displacement, speed and translocationof the cells (HeLa-EGFP) cultured on the nano-rough, micro-rough and Petri dish surfaces.....61
Figure 3.32: Mean squared displacement vs time interval for nano-rough, micro-rough polyHEMA surfaces and Petri dish surface for 24 hours 63
Figure 3.33: Mean squared displacement vs time interval for nano-rough, micro-rough polyHEMA surfaces and Petri dish surface for 0 to 6 hours' time interval and 12 to 18.2 hours' time interval.....64
Figure 3.34: Total mES cell number after each passage during 4 passages on micro-rough, nano-rough and smooth polyHEMA surfaces, as well as on the Gelatin and Petri dish surfaces. 66
Figure 3.35: Alkaline phosphatase staining of the mES cell after 4 passages cultured on the nano-rough and smooth polyHEMA surfaces.....67
Figure 3.36: Alkaline phosphatase staining of mES cells after four passages cultured on the micro-rough polyHEMA surfaces, Petri dish and gelatin. 68
Figure 3.37: Alkaline phosphatase staining of the mES cell after 4 passages cultured on the micro-rough polyHEMA surfaces, Petri dish and Gelatin, 10X magnification.....69
Figure 3.38: The expression of the stem cell pluripotency markers Oct3/4 and Nanog monitored by Western blotting. 69
Appendix Figure 5.1: Surface morphology of polyHEMA micro-rough, nano-rough, and smooth surfaces. Top row: high magnification SEM image. Scale bars 500 nm. Bottom row: low magnification SEM image. Scale bars are 5 μm 76
Appendix Figure 5.2: Formation of the filopodia by HeLa-EGFP cells cultured on the microrough surface 76
Appendix Figure 5.3: mES-Oct4-eGFP expressing cell lines on the micro-rough, nano-rough, smooth polyHEMA surfaces, on glass and on the feeder cells. 77
Appendix Figure 5.4: Percentage of the colonies of mES-Oct4-eGPF expressing cells after 3 days culturing on the micro-rough, nano-rough, smooth surfaces, on glass and on feeder cells...77
Appendix Figure 5.5: SEM images of the mES cells on the micro-rough, nano-rough, smooth, glass surfaces and on feeder cells. 78

Appendix Figure 5.6: mES cells on the micro-rough surface and on the feeder cells after 3 weeks 78
Appendix Figure 5.7: Percentage of the colonies of mES-Oct4-eGPF expressing cells after 3 days culturing on the micro-rough, micro-rough modified with decanethiol, micro-rough modified with aminethiol, on glass and on feeder cells. 78

List of Tables

Table 2.1. Composition of the polymerization mixtures for preparation of HEMA-EDMA surfaces with different morphology.....17
Table 2.2. Composition of the polymerization mixtures for preparation of BMA-EDMA surfaces with different morphology.....17
Table 3.1: Globule size for protruded and grooved polyHEMA surfaces produced using different polymerization mixtures.....28
Table 3.2: Roughness coefficients for protruded and grooved surfaces.....29
Table 3.3: Water contact angles of protruded and grooved polyHEMA surfaces after photografting with PFPMA.....34
Table 3.4: Water contact angles of protruded and grooved polyBMA surfaces.....36
Table 3.5: Water contact angles of grooved polyHEMA surfaces modified by photografting and chemically modified via thiol-yne reaction.....38

List of Abbreviations

HEMA	2-hydroxyethyl methacrylate
EDMA	ethylene glycol dimethacrylate
BMA	butyl methacrylate
PFPMA	2,2,3,3,3-pentafluoropropyl methacrylate
DMPAP	2,2-dimethoxy-2-phenylacetophenone
DIC	N,N'-diisopropylcarbodiimide
HA	HEMA-EDMA surface prepared from a mixture of 1 wt% DMPAP, 24 wt% of HEMA, 16 wt% of EDMA and 60 wt% of 1-decanol
HB	HEMA-EDMA surface prepared from a mixture of 1 wt% DMPAP, 24 wt% of HEMA, 16 wt% of EDMA, 10 wt% of cyclohexanol and 50 wt% of 1-decanol
HC	HEMA-EDMA surface prepared from a mixture of 1 wt% DMPAP, 24 wt% of HEMA, 16 wt% of EDMA, 20 wt% of cyclohexanol and 40 wt% of 1-decanol
HD	HEMA-EDMA surface prepared from a mixture of 1 wt% DMPAP, 24 wt% of HEMA, 16 wt% of EDMA, 30 wt% of cyclohexanol and 30 wt% of 1-decanol
BA	BMA-EDMA surface prepared from a mixture of 1 wt% DMPAP, 20 wt% of BMA, 30 wt% of EDMA and 50 wt% of 1-decanol
BB	BMA-EDMA surface prepared from a mixture of 1 wt% DMPAP, 20 wt% of BMA, 30 wt% of EDMA, 10 wt% of cyclohexanol and 40 wt% of 1-decanol
BC	BMA-EDMA surface prepared from a mixture of 1 wt% DMPAP, 20 wt% of BMA, 30 wt% of EDMA, 25 wt% of cyclohexanol and 25 wt% of 1-decanol
BD	BMA-EDMA surface prepared from a mixture of 1 wt% DMPAP, 20 wt% of BMA, 30 wt% of EDMA, 40% of cyclohexanol and 10 wt% of 1-decanol
WCA	Water Contact Angle
CAH	Contact Angle Hysteresis
SEM	Scanning Electron Microscopy
Ra	arithmetic mean deviation
Rq	root mean square deviation
Rp	maximum profile peak height
Rv	maximum profile valley depth
Rsk	skewness
Sa	average surface roughness

mES	mouse embryonic stem cells
AP	Alkaline Phosphatase staining

Table of Content

Abstract i
Zusammenfassung iii
Acknowledgements v
List of Figures vi
List of Tables x
Table of Content xiii
Chapter 1 1
Introduction 1
1.1 Surfaces and wetting 1
1.2 Superhydrophilicity and superhydrophobicity in nature 2
1.3 Theoretical models of surface wettability 3
1.4 Role of the surface hierarchy in wetting 8
1.5 Preparation of surfaces with hierarchical roughness 11
Chapter 2 14
Materials, methods and instruments 14
2.1 Chemicals and materials 14
2.2 Activation, modification, fluorination of the glass plates 15
2.3 Preparation of polymer films and patterns 16
2.3.1 Protruded and grooved micro-rough films 16
2.3.2 Smooth polyHEMA films 19
2.3.3 Nano-rough polyHEMA films 19
2.3.4 Photografting of the polyHEMA surfaces 19
2.3.5 Chemical modification of the grooved polyHEMA surfaces 20
2.4 WCA measurements 21
2.5 SEM measurement 21
2.6 DLS measurement 21
2.7 Roughness measurements 21
2.8 Measurement of water spreading in the micro-channels 22
2.9 Cancer cell experiment 22
2.9.1 Cell culture 22
2.9.2 Cell cross-contamination assay 23
2.9.3 Cell motility assay 23
2.10 Stem cell experiments 23
2.10.1 Cell culture 23

2.10.2 Cell lysis 24
2.10.3 Determination of the protein concentration 24
2.10.4 SDS-PAGE and Western blotting 24
2.10.5 Alkaline Phosphatase Staining 24
Chapter 3 25
Results and discussion 25
3.1 Superhydrophobicity of micro-rough protruded and grooved surfaces 25
3.1.1 Background 25
3.1.2 Experimental details 26
3.1.3 Surface properties of protruded and grooved surfaces 26
3.1.4 Roughness and polymer globule size of the grooved surfaces 38
3.1.5 Conclusions 43
3.2 Surface tension confined channels and Laplace micro-pump 44
3.2.1 Background 44
3.2.2 Experimental details 45
3.2.3 Generation of liquid flow using passive "Laplace pump" principle 45
3.2.4 Influence of the channel dimensions on the liquid flow 50
3.2.5 Conclusions 53
3.3 Cell behaviour on the rough surfaces 55
3.3.1 Background 55
3.3.2 Experimental details 57
3.3.3 Surface properties of the polyHEMA surfaces with different roughness 57
3.3.4 Cell motility assessment on the micro-rough grooved polyHEMA 58
3.3.5 Maintenance of stem cell pluripotency 65
3.3.6 Conclusions 71
Chapter 4 73
Conclusions and Outlook 73
Chapter 5 76
Appendix 76
Bibliography 82

Chapter 1

Introduction

1.1 Surfaces and wetting

Surface wetting is a fundamental interaction between liquid and a solid surface. Water contact angle (WCA) and contact angle hysteresis (CAH) are widely used for surface wettability characterization (Figure 1.1). The WCA is the angle between the planes tangent to the solid-liquid and liquid-vapour surfaces, where these two surfaces intersect. This intersection is called the contact line.

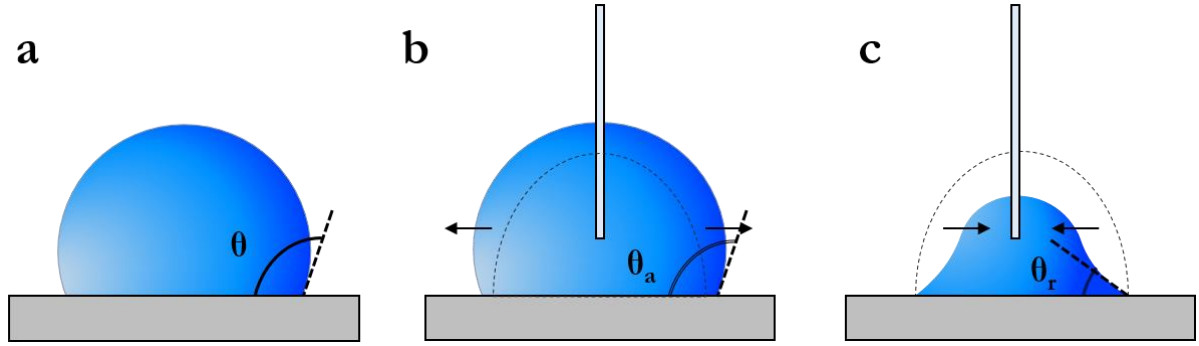

Figure 1.1: Water drop on a surface (a) with water contact angle θ, (b) advancing θ_a and (c) receding θ_r contact angles.

During the addition or removal of some liquid from the droplet or during droplet movement, the contact line will not advance or recede until the contact angle reaches the critical advancing or receding contact angle θ_a / θ_r. Difference between the advancing contact and receding contact is defined as contact angle hysteresis (CAH) [1]. CAH is usually related to the surface roughness, surface heterogeneity, and solution impurities adsorbing on the surface. For a droplet to move on a tilted surface, the droplet must both advance (on the downhill side) and recede (on the uphill side). Hence contact angle hysteresis is an important parameter for characterization of the surface wettability along with the static contact angle [2].

The contact angle measurement is the main method for the determination of the surface hydrophobicity. The most popular technique is the sessile drop measurement, where a small drop of liquid is placed on a surface. Advancing contact angle is measured when the volume of the droplet is increased and wetting line starts to advance. If afterwards the drop volume is decreased, the receding contact angle measured at the time point when the wetting line is receding. For a long time materials were commonly classified as hydrophobic (static WCA>90°) and hydrophilic (static WCA<90°) until in 1996 the terms superhydrophobicity and later superhydrophilicity were introduced [3]. And even up to today the discussion continues and remains open with various definitions being offered and used [4], [5].

1.2 Superhydrophilicity and superhydrophobicity in nature

The incredible ability of nature to adapt to the environment in the best manner is achieved through taking advantage of natural processes and diversity of the species. This was and still continues to be an object of great envy and admiration for the humankind. In the last decade, a variety of novel tools have emerged allowing us to understand the properties of natural systems and to create artificial surfaces based on the obtained knowledge [6], [7].

Superior wetting properties of some plant and animal surfaces were for a long time widely known yet unexplained phenomenon. A prominent example is lotus leaf *(Nelumbo nucifera)* which is symbol of the purity in the Buddhism due to its "self-cleaning" properties, but until report of Barthlott in 1997 [8] the reasons of such behaviour were unknown. In Barthlott's study, Scanning Electron Microscopy (SEM) was utilized to visualize surface morphology of the lotus leaf. From the SEM images, it can be clearly seen that the surface of the lotus is uniformly textured with 3–10 μm size protrusions and valleys, which are decorated with around 100 nm particles of a hydrophobic wax-like material (Figure 1.2). The combination of these special hierarchical surface structures and hydrophobic wax-like material is the reason for the superhydrophobicity of the lotus leaf with WCA of 162° and CAH of 3° [9].

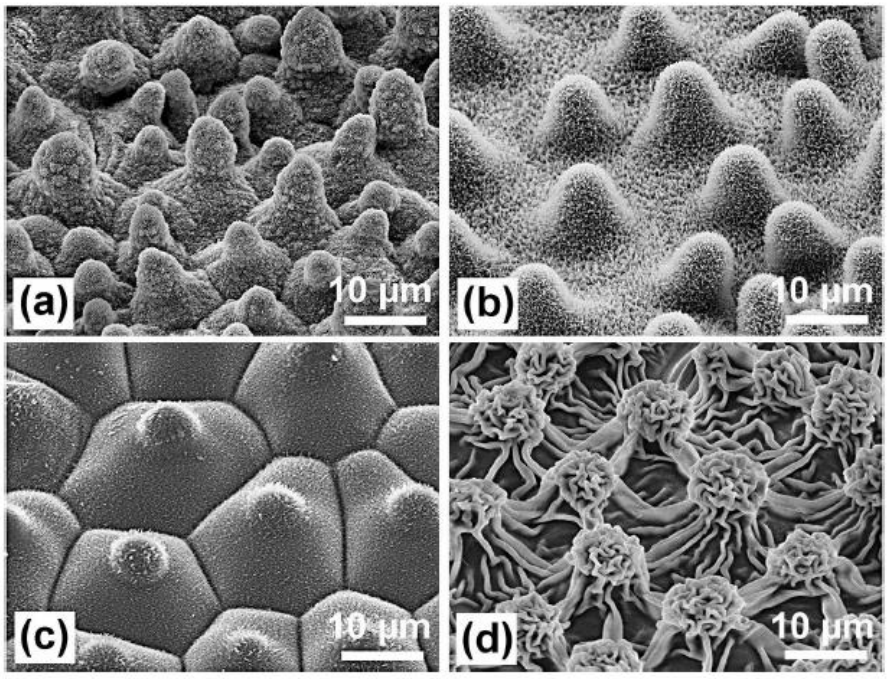

Figure 1.2: SEM images of plants: (a) lotus leaf (Nelumbo nucifera), (b) myrtle spurge (Euphoria myrsinites), (c) elephant ear (Colocasia esculenta) and (d) giant taro (Aloscasia macrorrhiza). From open access reference [9].

Since 1997 various studies appeared presenting surface morphology of various species [10]–[12]. For example, highly porous surface structure of mosses (*Rhacocarpus purourescens*, *Sphagnum* and others) allows them to quickly absorb rain or dew [13]. Their special surface structure also allows them to absorb water up

to 20 times more than their own weight [14]. Superhydrophobic legs covered with microsized needle-shaped setae and nanoscale groves is what allows water strider *(Gerris remigis)* to walk on the water surface [15].

Based on the obtained information [16]–[18], it can be concluded that in the nature superhydrophobicity is achieved mostly through hierarchical multiscale rough structures, whereas superhydrophilic plants usually exhibit highly porous texture. There are also a few exceptions to the specified pattern. For example, superhydrophobic systems were also achieved through so called "the pseudo-hierarchical surface" [19]. Therefore to fully explain these effects, it is necessary to understand the background and theory behind what happens at the contact of liquid and superhydrophobic surface.

1.3 Theoretical models of surface wettability

Formulated in 1805, Young's equation is the fundamental equation of the surface wetting [20]. It relates contact angle to the specific energies of the solid-liquid, solid-gas and liquid-gas interface for the ideal solid surface at thermodynamic equilibrium:

$$\cos\theta = \frac{\gamma_{SV} - \gamma_{SL}}{\gamma_{LV}} \qquad (1.1)$$

where θ is static contact angle, γ_{LV}, γ_{SL}, and γ_{SV} are interfacial free energies of the liquid-vapour, solid-liquid, and solid-vapour interfaces, respectively. Sometimes, θ is called intrinsic or Young's contact angle, as it represents inherent surface hydrophilicity or hydrophobicity.

The highest contact angle of a flat surface ever reported was 120° for a self-assembled monolayer of perfluorolauric acid absorbed on a platinum foil with the lowest critical surface energy of 5.6 mN/m [21]. Thus this model cannot explain observed high contact angles of some surfaces, due to the assumptions it imposes. Young's equation works only for flat and chemically homogeneous surfaces, but in reality very few solid surfaces are molecularly flat. The micro-defects are often produced on the surface of material during fabrication and they affect wetting by pinning a contact line.

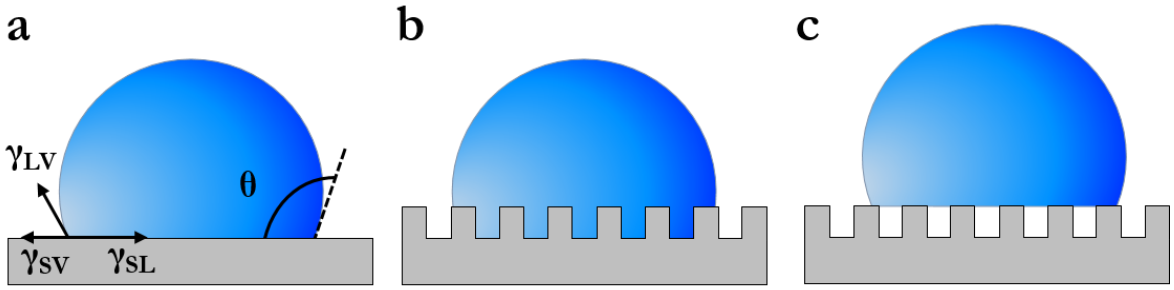

Figure 1.3: Theoretical models of surface wetting: (a) Young, (b) Wenzel, (c) Cassie-Baxter models

The limitations of the Young model were taken into account by the Wenzel model introduced in 1936 [22]. This model, unlike the Young's model, was formulated for a surface that has different topological

features such as cavities and bumps. Roughness factor r was introduced as parameter for characterization of such surfaces. It was defined as the ratio between the actual surface areas and the apparent (projected) surface area. This allowed to take into account increased wetted area of the rough surface compared to flat surface. Wenzel model assumes that during spreading, contact line follows all the topological features of the surface so that the liquid-air interface gets replaced by the solid-liquid interface of the same surface area. The Wenzel equation for the surface with a roughness factor can be expressed as following:

$$\cos\theta_W = r\ (\gamma_{SV} - \gamma_{SL})/\gamma_{LV} = r\cos\theta \qquad (1.2)$$

where θ_W is apparent contact angle and θ is intrinsic contact angle. When the surface is flat $r = 1$. For the rough surface $r > 1$, due to increased actual surface area to the apparent surface area. Hence according to the Wenzel equation (1.3) roughness amplifies hydrophobicity/hydrophilicity of a surface. For a surface with intrinsic contact angle $\theta > 90°$ (hydrophobic) $\cos\theta < 0$, $\cos\theta_W$ will be also negative and smaller by factor r and thus apparent contact angle θ_W will increase. For a surface with $\theta < 90°$ (hydrophilic) $\cos\theta > 0$, $\cos\theta_W$ will be positive and larger by factor r and thus apparent contact will decrease. As liquid adjusts to the surface roughness, the pinning of the contact line is particularly large. Hence the Wenzel state is characterized by the very low receding angles and a large contact angle hysteresis [23].

In 1944 Cassie and Baxter introduced a concept of the composite wetting state, which occurs when the liquid interface consists of two fractions liquid-solid and liquid-air [24]. For the surface rough enough, it is possible to trap air below the liquid and form so called Cassie-Baxter or "fakir" state. As a result, the drop sits on both solid and air interfaces and thus has a large apparent angle θ_{C-B}. The Cassie-Baxter equation for the heterogeneous interfaces can be written as following [24]–[26]:

$$\cos\theta_{C-B} = \varphi_1\cos\theta_1 + \varphi_2\cos\theta_2 = \varphi_1\cos\theta_1 - \varphi_2 \qquad (1.3)$$

where φ_1 is the total area of solid-liquid interface, θ_1 is contact angle on a smooth surface of material 1, φ_2 is the total area of liquid-air interface, and $\theta_2 = 180°$ since the second interface is air. For the surface consisting of solid-liquid fraction $(\varphi_1 = \varphi_{SL}, \theta_1 = \theta)$ and liquid-vapour $(\varphi_2 = \varphi_{LV} = 1 - \varphi_{SL}, \theta_2 = -1)$ fraction and implementing equation 1.3 the following equations emerge:

$$\cos\theta_{C-B} = \varphi_{SL}\cos\theta - (1 - \varphi_{SL}) = \varphi_{SL}\ (1 + \cos\theta) - 1 \qquad (1.4)$$

Presence of the air cushion in the Cassie-Baxter state leads to high contact angles and small contact angle hysteresis. This state results in superhydrophobic surfaces with properties such as reduced adhesion, water repellency, and bouncing of the water droplets [27]–[29].

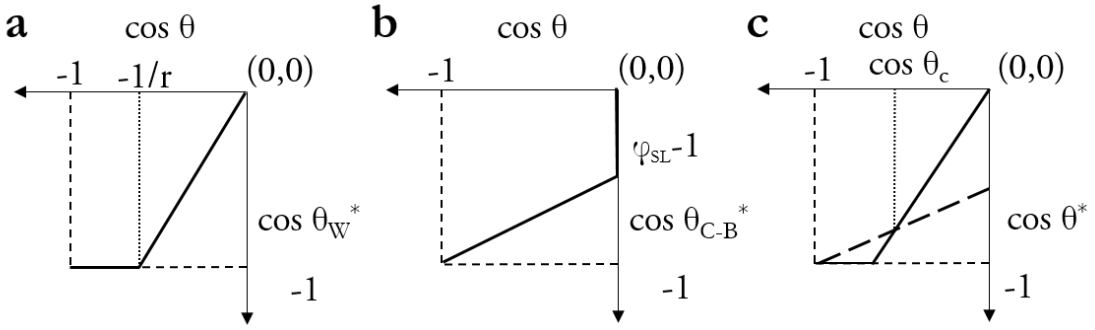

Figure 1.4: The apparent contact angle θ^* dependence on the intrinsic contact angle θ for the surface with $\theta \geq 90°$ exhibiting: (a) Wenzel (θ_W^*), (b) Cassie-Baxter (θ_{C-B}^*), (c) Wenzel (solid line) and Cassie-Baxter (dash line) states.

Wenzel and Cassie-Baxter models show how apparent contact angle θ^* is increased relative to the intrinsic contact angle θ. Figure 1.4 shows apparent contact angle as a function of intrinsic contact angle θ according to the Wenzel and Cassie-Baxter equations. According to the Wenzel formula, the maximum apparent contact angle $\theta = 180°$ is achieved when $\cos\theta = -1/r$. Similarly, the Cassie-Baxter equation shows apparent contact angle is $\cos\theta_{C-B} = \varphi_{SL} - 1$ when $\cos\theta = 0$ and is 180° only when θ is 180°. When plotted together Wenzel and Cassie-Baxter graphs intercept at critical angle θ_c, when $\theta_W = \theta_{C-B}$. This angle is given by the following equation:

$$\cos\theta_c = (1 - \varphi_{SL})/(r - \varphi_{SL}) \qquad (1.5)$$

For intrinsic contact angle θ lower than θ_c, Cassie-Baxter apparent contact angle θ^* is higher than Wenzel and when θ is higher than θ_c the situation is opposite. From the thermodynamical point of view, the drop with the lowest energy will be formed. Energy of a drop of given volume in equilibrium was calculated using energy minimization approach [30].

$$\frac{G}{\sqrt[3]{9\pi}V^{2/3}\gamma_{LV}} = (1 - \cos\theta^*)^{\frac{2}{3}}(2 + \cos\theta^*)^{\frac{1}{3}} \qquad (1.6)$$

where G is Gibbs free energy, V is droplet volume, γ_{LV} is interfacial free energy of liquid-vapour interface, $\theta^*$is apparent contact angle. The equation shows that energy of the droplet is increasing with θ^*. As the result, equilibrium state with lower apparent contact angle θ^*will have lower energy. Thus for $\theta < \theta_c$, Wenzel state will be more energetically favorable, while for $\theta < \theta_c$ Cassie-Baxter state will have lower energy.

The thermodynamic models show that Cassie-Baxter and Wenzel states represent two free energy minima, with usually one being favoured [31]. However it was reported that droplets on the surface do not necessary assume the state with absolute minimum energy. For example, when water droplet was smoothly deposited on the surface, formation of metastable Cassie-Baxter state has been observed. It was observed experimentally that the contact angle of a surface changes and the state of liquid/solid contact changes from Cassie-Baxter state into Wenzel state under pressure [32] or vertical vibration [33]. In addition, a fully reversible transition from one state to another could be achieved by using electrowetting and corrugated

surfaces [34]. Therefore both states could be formed and the transition from one to another is possible. When liquid is dispensed from above, the Cassie-Baxter sate is formed first, since it is the first physical contact that is encountered. However, formation of the drop in Cassie-Baxter state does not imply that the drop is in global minimum. In order to change to the state of lower energy the drop should overcome an energy barrier. Various criteria were proposed such as contact line density [35], energy barrier [36], spacing factor [37], and size of the water droplet [38] to predict transition from Cassie-Baxter to Wenzel state.

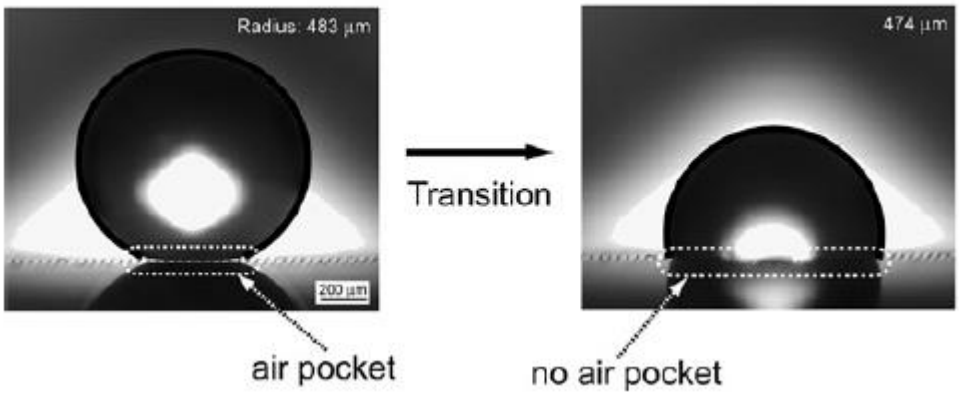

Figure 1.5: Water droplet on patterned Si surface coated with PF3. Image reprinted from [38] with permission from Elsevier, Copyright 2007.

For example, if the droplet is dispensed on the array of pillars it can form Cassie-Baxter state. However if the sag of the drop is much greater than the depth of cavity, then the droplet will contact the bottom of the cavities. As the result of the transition the drop will form Wenzel state. This criteria can be written by following expression:

$$(\sqrt{2}P - D)^2/R \geq H \qquad (1.7)$$

where diameter D is diameter, H is height of the pillar, and P is pitch between the pillars. An experimental study showed that the measured critical radius where transition occurs, was in good agreement with the proposed criteria (Figure 1.5). It was also shown that the geometrical shape of the surface texture affects the wetting regime [39].

As was mentioned before, contact angle hysteresis is an important parameter for the characterization of the surface hydrophobicity. Prediction and understanding of the contact angle hysteresis is an interesting yet difficult task as its value depends on local surface roughness and chemical inhomogeneity [33], [40]–[43]. For example, Gao and McCarthy [42] view contact hysteresis as the kinetic effect and a reflection of the activation energy required for the drop movement from one metastable state to another. This approach is useful for qualitative prediction of the hysteresis.

Tadmor [44] showed theoretically that equilibrium contact angle θ_{eq} can be calculated from advancing θ_a and receding θ_r contact angles. It was later experimentally confirmed [45].

$$\cos\theta_{eq} = \frac{R_a \cos\theta_a + R_r \cos\theta_r}{R_a + R_r} \qquad (1.8)$$

$$R_a = \frac{\sin^3\theta_a}{2 - 3\cos\theta_a + \cos^3\theta_a}$$

$$R_r = \frac{\sin^3\theta_r}{2 - 3\cos\theta_r + \cos^3\theta_r}$$

Theoretical models for prediction of hysteresis utilize assumption that contact angle hysteresis consists of two parts – adhesion hysteresis term (as it is known that adhesion work for separating the surfaces is smaller than energy obtained for surfaces during contact) and pinning term, H_r [37], [46]. The first term is proportional to the solid-liquid area $(1 - \varphi_s)$ and cosines of advancing and receding angles are related to those of smooth surface θ_{a0}, θ_{r0}. Using equation 1.6:

$$\cos\theta_a - \cos\theta_r = r\,(1 - \varphi_{LV})(\cos\theta_{a0} - \cos\theta_{r0}) + H_r \qquad (1.9)$$

This equation shows that increasing the fraction of liquid-vapour area leads to an increase of the contact angle and a decrease of the contact angle hysteresis $(\varphi_{LV} \to 1, \cos\theta \to -1, \theta \to \pi, \cos\theta_a - \cos\theta_r \to 0)$.

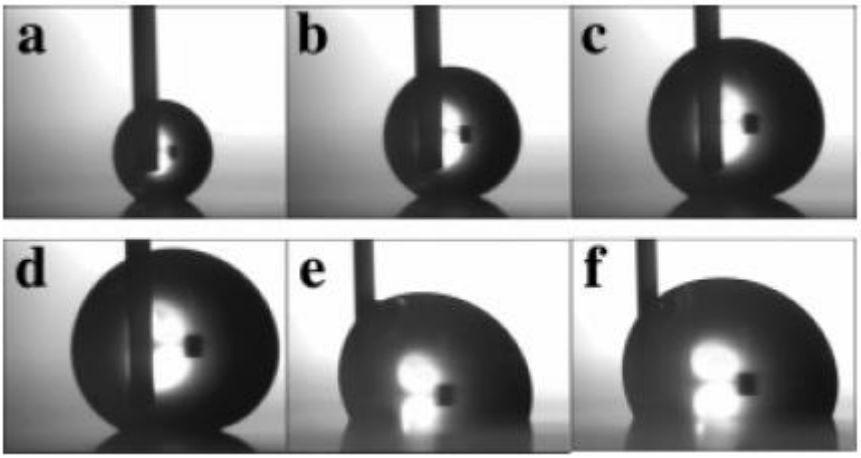

Figure 1.6: Selected frames of a videotapes of a droplet advancing from rough spot onto a smooth field. Reprinted from [47] with permission from American Chemical Society, Copyright 2007.

Recently, applicability and validity of Wenzel and Cassie-Baxter theories were questioned. Extrand et al. [48] and Gao et al. [47], showed that events at the contact line, and not over the liquid-solid interface area, determine and control contact angles. For example, the droplet advancing from the rough spot to the smooth part of the surface will show higher contact angle on the rough part of the surface and lower on the smooth (Figure 1.6.). Some reports also showed that three-phase contact line affects contact angle dependency on the area fraction [49]. This findings were highly disputed and the discrepancies between Cassie-Baxter theory and experiments were attributed to the incorrect choice of surface area fractions [50] and the nonuniformity of the surface roughness [51]. Formation of the thin precursor film should be also taken into consideration as it may promote pinning of the triple line [52]. It was proven that Wenzel and Cassie-Baxter equations are only valid when the size of the droplet is sufficiently larger than roughness or chemical heterogeneity of the surface [53]. It was stated that local events at the three-phase contact line

determine actual contact angles. Whereas global conditions at the solid-liquid interfacial area determine the most stable apparent CA, which is predicted by the Wenzel and Cassie-Baxter equations [54]. Results from many experiments showed Wenzel and Cassie-Baxter equations are valid for most cases, but should be used with caution and aware of the assumptions imposed [55], [56].

It is important to note that Young, Wenzel and Cassie-Baxter equations describe macroscopic contact angles. But the actual angle at microscale and nanoscale can be quite different. Long-distance Van der Waals adhesion forces create disjoining pressure [57] and lead to the thin water layer formation at the surface. As a result, shape of the droplet near the contact line transforms from spherical shape into the precursor layer, thus nanoscale contact angle is smaller than apparent angle. Formation of thin water α-films (absorption) and β-films (wetting) on a hydrophilic surface is quite common [58].

1.4 Role of the surface hierarchy in wetting

A plethora of natural superhydrophobic surfaces exhibit characteristic hierarchical surface morphology [16]. Elimination of the drops of different sizes, for example rain and dew, could be one of the possible uses of the two-scale roughness in nature. Experimental studies of the superhydrophobicity of the flat, microstructured and hierarchical surfaces suggest that presence of not only micro- but also nanostructures ensured not only high static contact angles, but also low hysteresis and sliding angle. For example, Bhushan et al. produced surfaces with micro and nanostructures and observed that compared to microstructured, hierarchical surfaces have lower contact angle hysteresis as well as adhesion force (Figure 1.7) [59]. However the impact of the two-scale roughness on hydrophobicity is more complicated and condition-dependent.

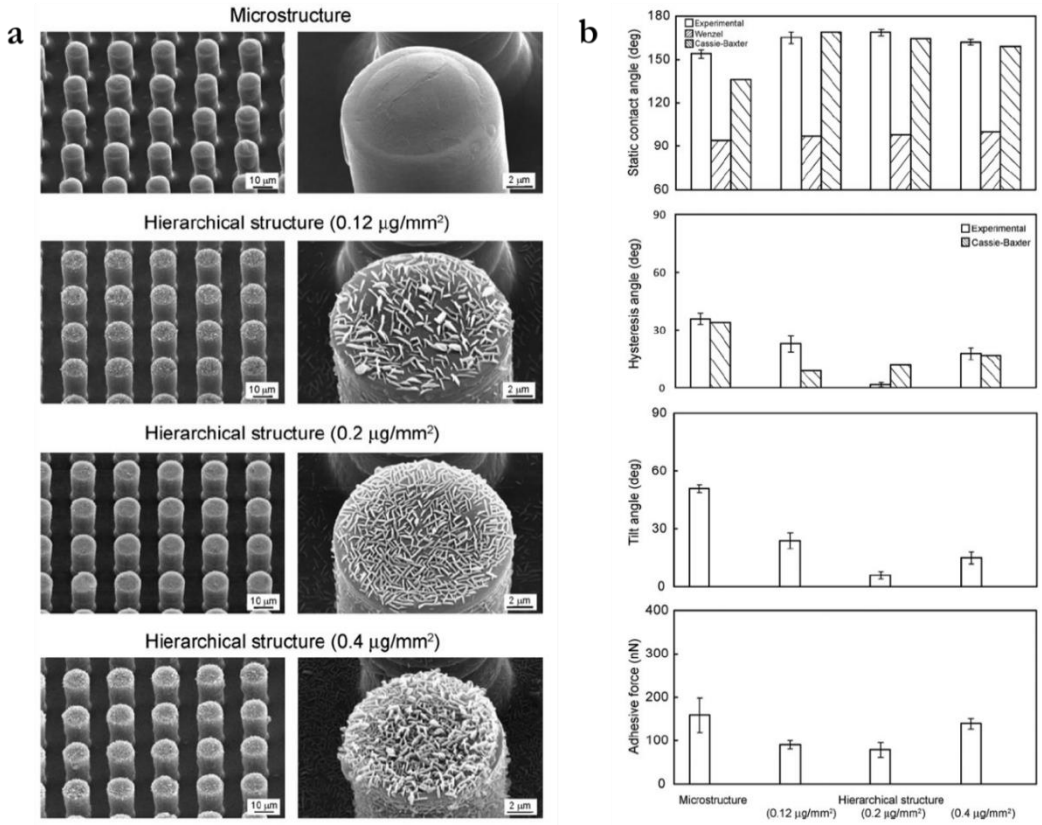

Figure 1.7: Characterization of the hierarchical surfaces with (a) SEM showing surface morphology of microstructured and hierarchical structure, (b) contact angle, hysteresis, tilt and adhesion force for microstructured and hierarchical surfaces. Reprinted from [59] with RSC permission, Copyright 2008.

In order to understand the outstanding properties of the lotus leaf, a paraboloid model was used as an approximation of the lotus leaf surface [60]. It was shown that in the Wenzel state, as the distance between protrusions get larger, the paraboloids need to be steeper in order to reach a sufficiently high contact angle. This might not be plausible as the high steepness leads to mechanical vulnerability. In contrast, the wet area does not depend on the paraboloid distance (only if the distance is not too large) in Cassie-Baxter state. The hierarchical structure of the lotus leaf also protects it from the water penetration. When liquid is pushed downward between the protuberances of the leaf, the suspension force increases due to an increase in both the contact line associated with the primary features and the sharp edges of the secondary features [61].

Thermodynamical analysis indicates that employment of double roughness structures not only amplifies apparent contact angle, but also leads to more energetically stable Cassie-Baxter state [62], [63]. This was shown for an array of nanopillars (size a_1, height H_1, and spacing b_1) on the array of micropillars (size a_2, height H_2, and spacing b_2). The apparent contact angles for such model:

$$\cos\theta_{C-B} = A_1(1 + \cos\theta_e) - 1 \qquad (1.10)$$

$$\cos\theta_W = \left(1 + \frac{4A_1}{a_1/H_1}\right)\cos\theta_e$$

where $A_1 = \frac{1}{((b_1/a_1)+1)^2}$ and θ_e is equilibrium contact angle of the liquid drop on a flat surface. Apparent contact angle in Cassie-Baxter depends only on b_1/a_1, while in Wenzel state it depends on both b_1/a_1 and H_1/a_1. Energy of the drop is then expressed by equation 1.7, which shows that the state with lower apparent contact angle has lower energy. By analyzing values of apparent contact angle for different states it is possible to find which state will be formed (Figure 1.8).

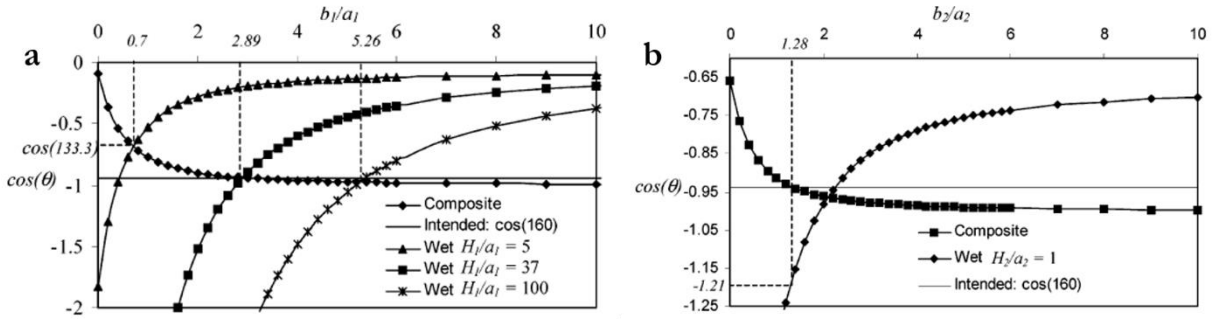

Figure 1.8: Plots of apparent contact angles ($\cos\theta$) for wetted Wenzel and composite Cassie-Baxter states as the function of roughness geometry parameters b_1/a_1 and b_2/a_2 for (a) only micropillars and (b) micropillars and nanopillars. Solid line represents $\cos\theta = \cos 160 = -0.93$ as the intended contact angle, diamonds represent Cassie-Baxter state and triangle, square and star show Wenzel states with different H_1/a_1 values. Reprinted from [62] with permission of American Chemical Society, Copyright 2004.

As an example, array of micropillars with $\theta_e = 95°$ were used as a model and it was shown that an array can be turned superhydrophobic by changing roughness geometry parameters. In terms of creating robust superhydrophobic surface, Cassie-Baxter state should be more energetically favourable than Wenzel state and transitions between these states should be prevented by high energy barrier. Cassie-Baxter state with contact angle of 160° (intended line in Figure 1.8a) will be formed when $b_1/a_1 = 2.89$. However, to ensure that Cassie-Baxter is indeed the favourable state, contact angle of the Wenzel state should be higher. This can be achieved by high H_1/a_1 ratios, as the Wenzel state will have larger contact angle and thus higher energy (when $H_1/a_1 = 37$ Wenzel and Cassie-Baxter states have the same contact angle and, as the result, the same energy). In practice achieving high aspect ratios is not desirable as the system becomes mechanically instable. Increase in the b_1/a_1 will lead to higher CA, but it also decreases energy difference between the states (when $b_1/a_1 = 5.26$ energy of the Wenzel and Cassie-Baxter states will be the same). By using the same approach, the calculations for the combination of micropillars and nanopillars can be made (Figure 1.8b). The role of the micropillars was set to the amplifying contact angle from $\theta_e = 95°$ to $\theta_{int} = 133°$. In this case even, if the array of nanopillars does not have high contact angle (low H_2/a_2 ratios) in combination with micropillars, the contact angle of the array will be significantly enhanced. This could not be achieved for such low aspect ratios without micropillars.

Interestingly, it was also shown that the effect of micropillar and nanopillars on the stability of the Wenzel and Cassie-Baxter states differ greatly [64]. In particular, presence of the microstructures actually decreases the stability of the metastable Cassie-Baxter state for nanopillars, which was confirmed

experimentally [65]. Effect of the nanostructures on the micropillars depends on whether they are situated on top or at the bottom of the microstructure. While top nanopillars decrease the transition barrier to Wenzel state for the micropillars, bottom nanopillars severely increase stability of the Cassie-Baxter state for the microstructures.

The role of the hierarchical structure in stabilizing fragile Cassie-Baxter state was reported [66]. The mechanisms that destabilize the composite state are scale dependent and the multiscale roughness is required, since it provides pinning of the interface and thus leading to a stable equilibrium [67]. Similarly, it was shown that hierarchy has a significant effect on the mechanical stability of the superhydrophobicity [66], [68]. Effect of the two-scale topography on the kinetics of the contact line recession was shown [69]. Since receding process has higher activation energy than advancing process and is crucial for the contact angle hysteresis, addition of the two-scale features lowered the transition state energy between metastable states. Analysis of the hierarchical surfaces of different topographies showed that it does have beneficial effect on the high contact angles and stability: however to a certain extent and depending on the basic geometry of the surface [70].

Hierarchical roughness plays an important role in the control of the superhydrophobic properties of the surfaces. Extensive studies show that role of double roughness structures or slender pillars lies in amplifying the apparent contact angle and making the composite drop energetically much more favourable and stable. However its effect is limited and it is necessary to keep in mind that all the factors may affect the wetting, when designing superhydrophobic surfaces.

1.5 Preparation of surfaces with hierarchical roughness

Hierarchical structure of the surface offers multiple advantages and improves its superhydrophobic properties. Variety of the methods have been developed to create and manipulate specified micro- and nanostructures. The micro- and nanofeatures of produced surfaces provide necessary surface roughness and topography. The most widely used methods are moulding, transfer printing, self-assembly and hybrid methods.

In the molding approach, deformable or curable material were filled into empty spaces of the mold of complementary shape to create the microstructures on the surface. Polydimethylsiloxane (PDMS) is widely used as a mould material due to its low modulus for conformal contact and low surface tension for easy release. However, its low modulus is a drawback for the preparation of high-resolution, high aspect ratios structures. To solve this problem, UV-curable polyurethane acrylate (PUA) has been used extensively for fabrication of sub-100 nm patterns [71]. Utilization of precise silicon masters prepared by photolithography allows moulding techniques to achieve high-resolution micro- and nanostructures [72], [73]. Although the preparation of the silicon master is time-consuming and costly, it ensures reproducibility and large area patterning. Two step photolithography is the direct way to produce multiscale structures

(Figure 1.9). With this approach, two layers of photoresists with micro- and nanofeatures are prepared with suitable size and a curable resin is back-filled to replicate the desired surface structure [74]. Another approach uses two separate moulds with micro and nanostructures that are placed sequentially (Figure 1.9) [75].

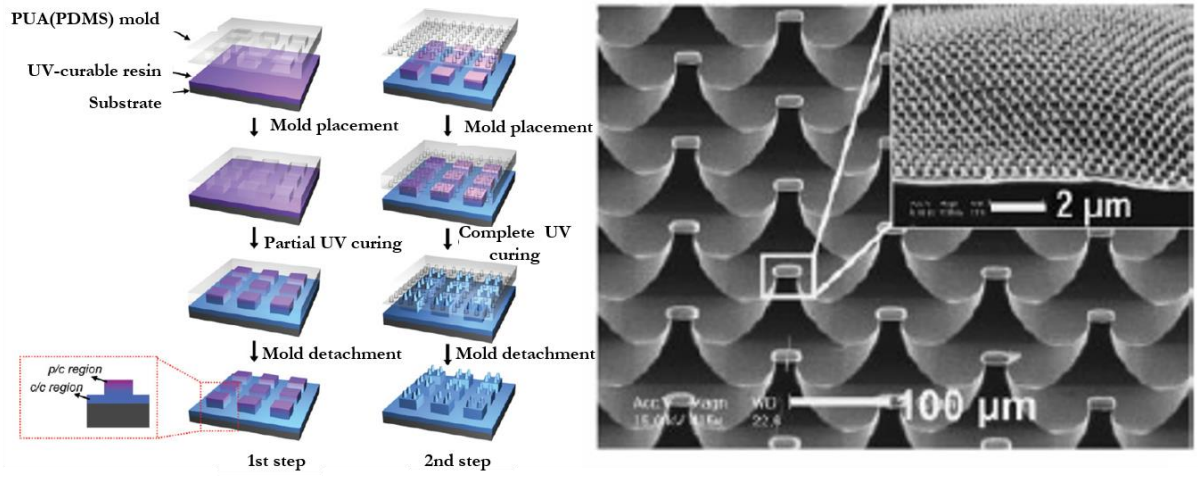

Figure 1.9: Schematic description of the two-step moulding approach via capillary force lithography (CFL) and example of the produced surfaces. Reprinted from [75] with permission from John Wiley and Sons, Copyright 2008.

Transfer printing is the process of transferring soft target materials on a receiving surface, such as polymer, glass, metal, etc. PDMS stamps are widely used as they allow the transfer of a metal or polymer layer to a substrate. Transfer printing is sensitive to the stamp chemistry and topography and resolution of the method depends on the mechanical rigidity of the mould [76]. This approach have significant advantages as it enables replicating patterns with high aspect ratios to be produced, for which moulding process is not always acceptable. Using multistep approach, variety of the surface structures have been made [77]–[80].

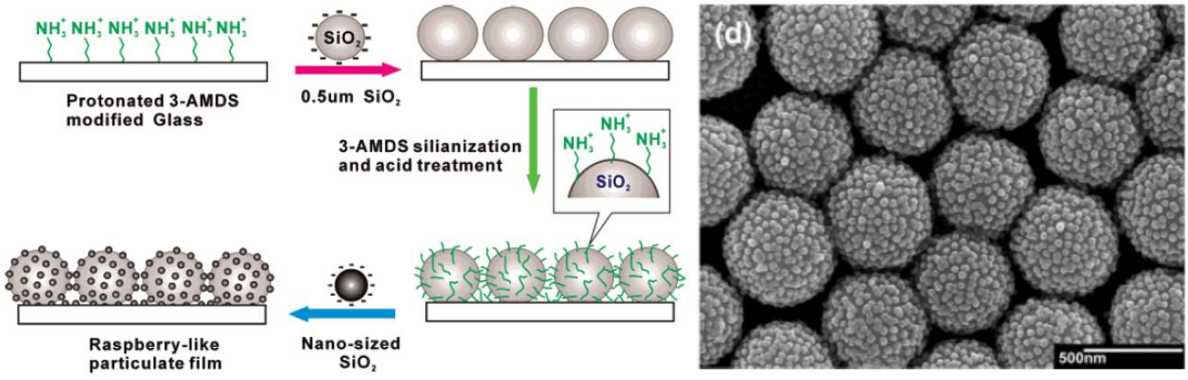

Figure 1.10: Schematic example of the self-assembly process and the produced surface. Reprinted from [81] with permission from American Chemical Society, Copyright 2007

Self-assembly methods utilize spontaneous assembly of molecules, nanoparticles and polymers for constructing complex surface structures. The means of the assembly may differ as various physical and chemical external manipulations are utilized. The created structures are closer to biomimetic surfaces than

those created by other means. Moreover, the method is fast, cheap and does not require expensive equipment. On the other hand, self-assembly is less controllable than other methods and not always reproducible, as the process greatly depends on the physical conditions. Self-assembly of micro- and nanoparticles is the most commonly used simple way to create specific hierarchical surfaces (Figure 1.10) [81]–[85].

Hybrid methods utilize combination of the self-assembly techniques with moulding approach. Typically in the hybrid method, the nanoscale texture is added to the microscale structures in an additional step. Usually the microscale structures are produced with moulding techniques, while the nano features are introduced using self-assembly [86]–[88]. The application of this approach is particularly useful for preparation of the complex hierarchical structures that is not possible to produce by using one method.

Chapter 2

Materials, methods and instruments

2.1 Chemicals and materials

2-Hydroxyethyl methacrylate (HEMA), buthyl methacrylate (BMA), ethylene glycol dimethacrylate (EDMA), 2,2,3,3,3-pentafluoropropyl methacrylate (PFPMA), (trimethoxysilyl)propyl methacrylate, trichloro(1H, 1H, 2H, 2H-perfluorooctyl)silane, 2,2-dimethoxy-2-phenylacetophenone (DMPAP), 4-pentynoic acid, 4-(dimethylamino)pyridine (DMAP), N,N'-diisopropylcarbodiimide (DIC), benzophenone, 1-decanethiol, cysteamine, 1H,1H,2H,2H-perfluorodecanethiol, cyclohexanol, 1-decanol, dichloromethane were purchased from Sigma-Aldrich (Germany) at purity >97%. 1-Butanol was purchased from Carl Roth (Germany) at purity 99.5%. All other chemicals were purchased from Sigma-Aldrich and used as supplied.

Quartz photomask was developed with Autodesk Inventor 2011 software and manufactured by Rose Fotomasken (Germany). Glass plates from Schott Nexterion B (Germany), Teflon films from American Durafilm (USA) were employed in this study.

For the stem cell experiment following antibodies were used:

Primary antibody	**Description**	**Source**
Nanog	Rabbit, polyclonal	Serotec
PCNA (PC-10)	Mouse, monoclonal	Santa Cruz
Oct3/4 (H-300)	Mouse, monoclonal	Santa Cruz
SSEA1(480)	Mouse, monoclonal	Santa Cruz

Secondary antibody	**Source**
Goat anti-mouse IgG/HRP	Dako
Goat anti-rabbit IgG/HRP	Dako
Alexa Fluor 488 goat anti-mouse IgG	Invitrogen

2.2 Activation, modification, fluorination of the glass plates

For activation the glass plates were immersed in 1M NaOH for 30 min, cleaned with water and immersed in 1M HCl for 30 min. Later the plates were washed with ethanol and dried.

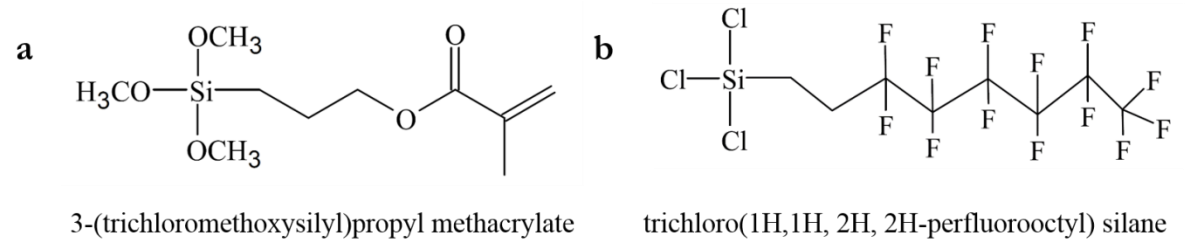

Figure 2.1: Structures of the modification and fluorination chemicals.

For modification activated glass plates were wetted with modification mixture (20 vol%. 3-(trimethoxysilyl)propyl methacrylate in ethanol adjusted to pH=5 with acetic acid buffer) and covered with another activated glass plate (Figure 2.2.). After 30 min the glass plates were separated and washed. The same side was again wetted with modification mixture and covered with another glass plate. After 30 min the glass plates were separated, washed with ethanol and dried with nitrogen gun.

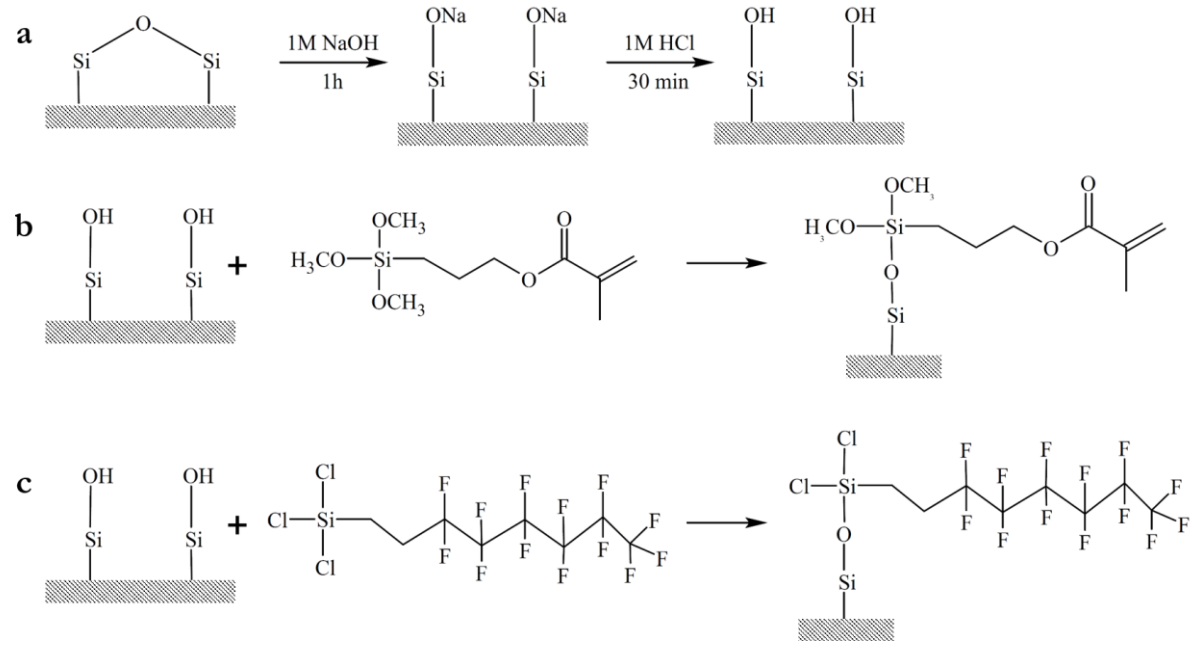

Figure 2.2: Scheme of the activation (a), modification (b), and fluorination (c) of the glass plates.

For fluorination an activated glass plates were exposed to trichloro(1H, 1H, 2H, 2H-perfluorooctyl)silane in an evacuated desiccator overnight.

2.3 Preparation of polymer films and patterns

2.3.1 Protruded and grooved micro-rough films

2.3.1.1 Polymerization mixtures

Polymer mixture consisted of monomer (HEMA for hydrophilic surface or BMA for hydrophobic surfaces), cross-linker (EDMA), initiator (DMPAP), and porogens (1-decanol and cyclohexanol) (Figure 2.3.). Different ratios of the 1-decanol and cyclohexanol were used for control of the pore size, as it was shown that 1-decanol leads to big pores, whereas cyclohexanol results in small pores [89].

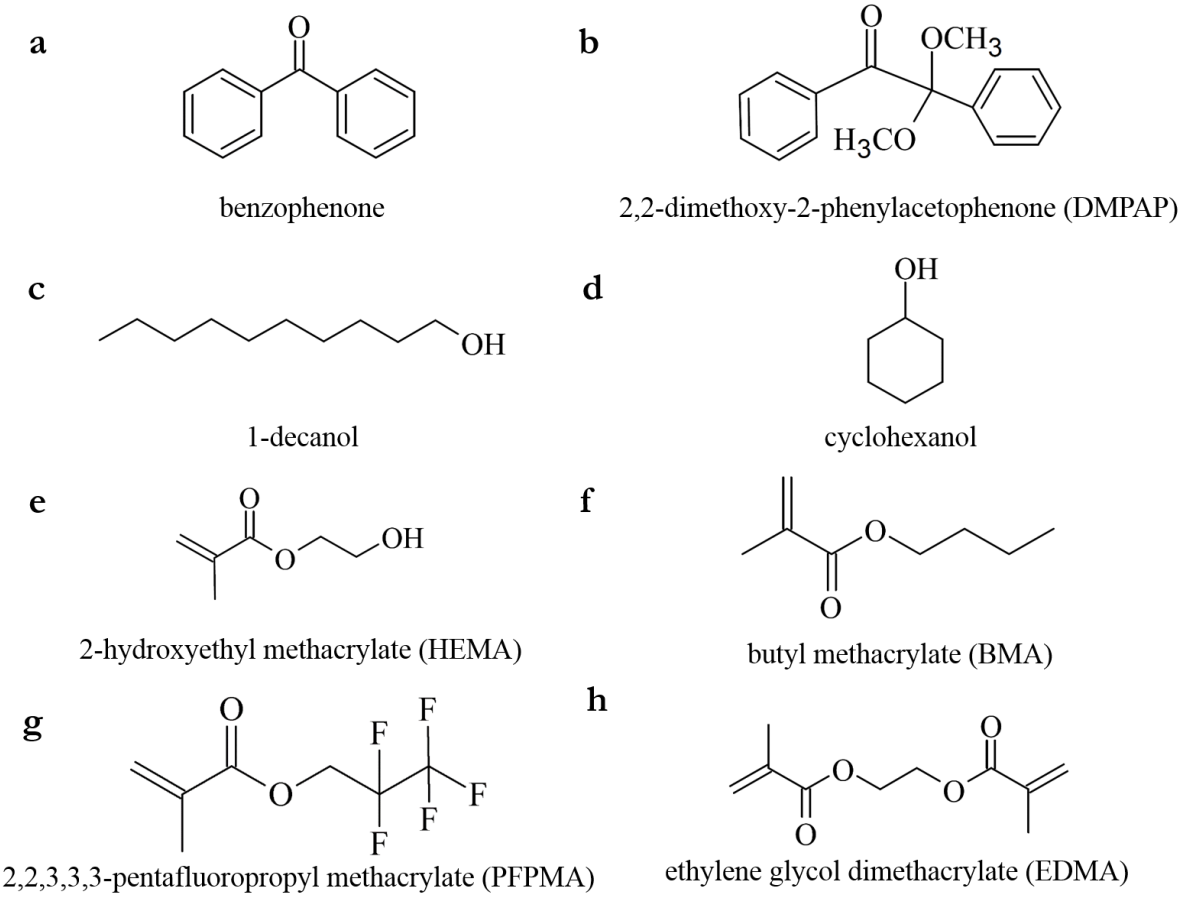

Figure 2.3: Chemical structures of the utilized polymerization initiators (a,b), porogens (c,d), monomers (e,f,g), and cross-linker (h).

All HEMA-EDMA mixtures contained the same amount of HEMA, EDMA, DMPAP, with total porogen content kept at 60 wt% for all the surfaces.

Table 2.1. Composition of the polymerization mixtures for preparation of HEMA-EDMA surfaces with different morphology.

Composition	**HA**	**HB**	**HC**	**HD**
HEMA, wt %	24	24	24	24
EDMA, wt %	16	16	16	16
DMPAP, wt %	1	1	1	1
1-decanol, wt %	60	50	40	30
cyclohexanol, wt %	0	10	20	30

All BMA-EDMA mixtures contained the same amount of BMA, EDMA, DMPAP, with total porogen content kept at 50 wt% for all the surfaces.

Table 2.2. Composition of the polymerization mixtures for preparation of BMA-EDMA surfaces with different morphology.

	BA	**BB**	**BC**	**BD**
BMA, wt %	20	20	20	20
EDMA, wt %	30	30	30	30
DMPAP, wt %	1	1	1	1
1-decanol, wt %	50	40	25	10
cyclohexanol, wt %	0	10	25	40

2.3.1.2 Polymerization

Polymer films were prepared by free radical photopolymerization of a corresponding polymerization mixture containing the monomer HEMA, cross-linker EDMA, porogens, and initiator DMPAP (Figure 2.4). For covalent attachment of the polymer to the glass surfaces, both utilized glass plates were beforehand modified with 3-(trimethoxysilyl)propyl methacrylate, contrary to the previously used method [90], [91]. Utilization of the photoinitiated polymerization offers several advantages such as (1) ability to start and stop polymerization on demand by turning off irradiation source, (2) spatial control of the polymerization, (3) possibility to perform the reaction at the room temperature. In the initiation step, excited photoinitiator generates reactive centers. During this process DMPAP is excited by energy absorption and as a result forms two radicals. Propagation of the reactive center by the addition of the monomer molecules leads to the growth of the polymer chain.

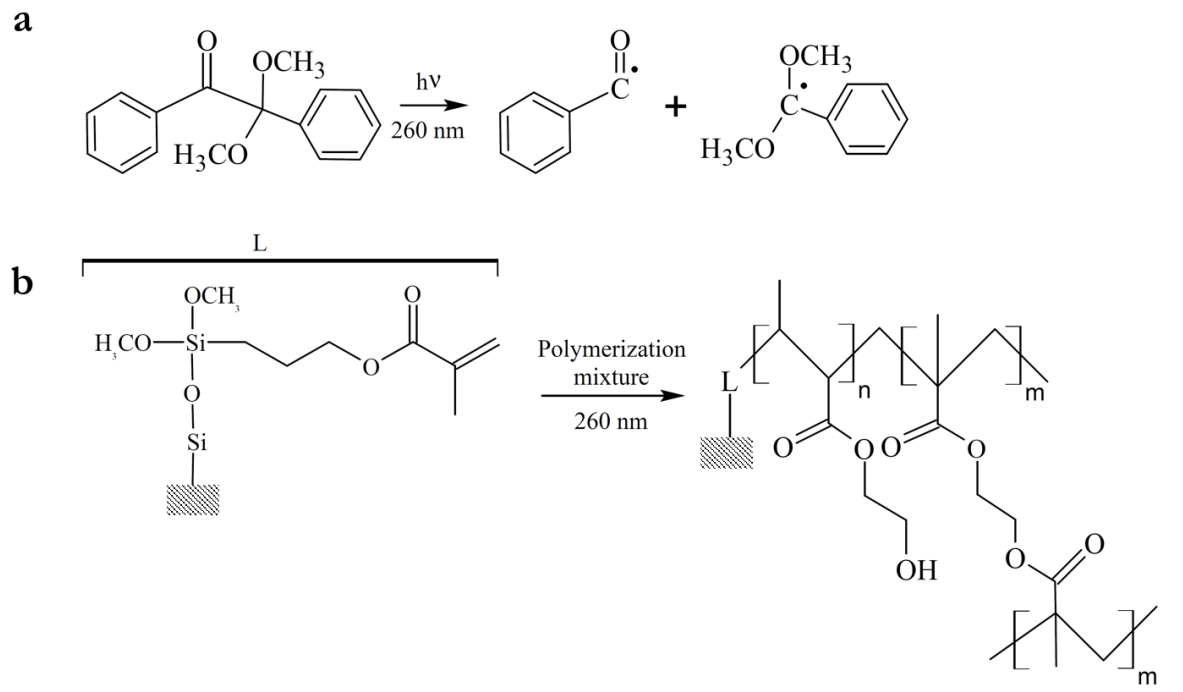

Figure 2.4. Scheme of the (a) initiation process by 2,2-dimethoxy-phenylacetophenone (DMPAP), and (b) polymerization of the 2-hydroxyethylmethacrylate (HEMA) and ethylene glycol dimethacrylate (EDMA) on the previously modified glass plate.

For the preparation of the polymer film, corresponding polymerization mixture was poured into the mold, consisting of the two modified glass plates. Plates were separated with 75 μm thick poly imide spacers for control of the polymer thickness. The mold was placed under UV-light (intensity 12 mW/cm^2, wavelength 260 nm) for 15 minutes (Figure 2.5). After UV-light irradiation the two glass plates were separated by a scalpel.

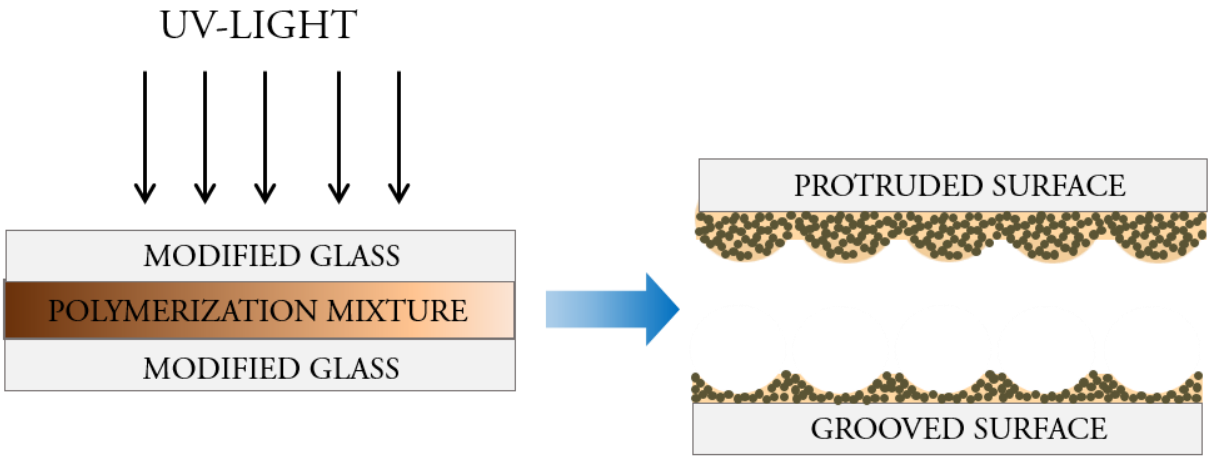

Figure 2.5: Schematic description of the polymer film preparation in the mold by the UV-initiated photopolymerization.

The hardened polymer broke and a polymer film was attached to both glass plates. The top glass slide, closer to the UV-light irradiation, forms ***protruded*** polymer film and bottom glass slide- ***grooved***.

The polymer films were washed with ethanol and acetone and dried with air gun. The samples were stored in methanol.

2.3.2 Smooth polyHEMA films

Smooth polyHEMA-EDMA surfaces were prepared using 60% HEMA, 40% EDMA. The polymerization mixture was poured into the mold, made of modified and fluorinated glass plates. Plates were separated with 12.5 μm thick polyimide spacers for control of polymer thickness. The mold was placed under UV-light (intensity 12 mW/cm^2, wavelength 260 nm) for 15 minutes. After UV-light irradiation the two glass plates were separated by a scalpel. The polymer films were washed with ethanol and acetone and dried with air gun. The samples were stored in methanol.

2.3.3 Nano-rough polyHEMA films

Nano-rough polymer mixture contained 24 wt% HEMA, 16 wt% EDMA, 1 wt% with respect to monomers photo initiator DMPAP, 12 wt% 1-decanol and 48 wt% cyclohexanol.

The polymerization mixture was poured into the mold made of modified and fluorinated glass plates. Plates were separated with 12.5 μm thick poly imide spacers which control polymer thickness. The mold was placed under UV-light (intensity 12 mW/cm^2, wavelength 260 nm) for 15 minutes. After UV-light irradiation the two glass plates were separated by a scalpel. The polymer films were washed with ethanol and acetone and dried with air gun. The samples were stored in methanol.

2.3.4 Photografting of the polyHEMA surfaces

Photografting mixture contained: 25 wt% PFPMA, 1 wt% EDMA, 0.25 wt% benzophenone dissolved in a 1/3 (v/v) mixture water-*t*-butanol.

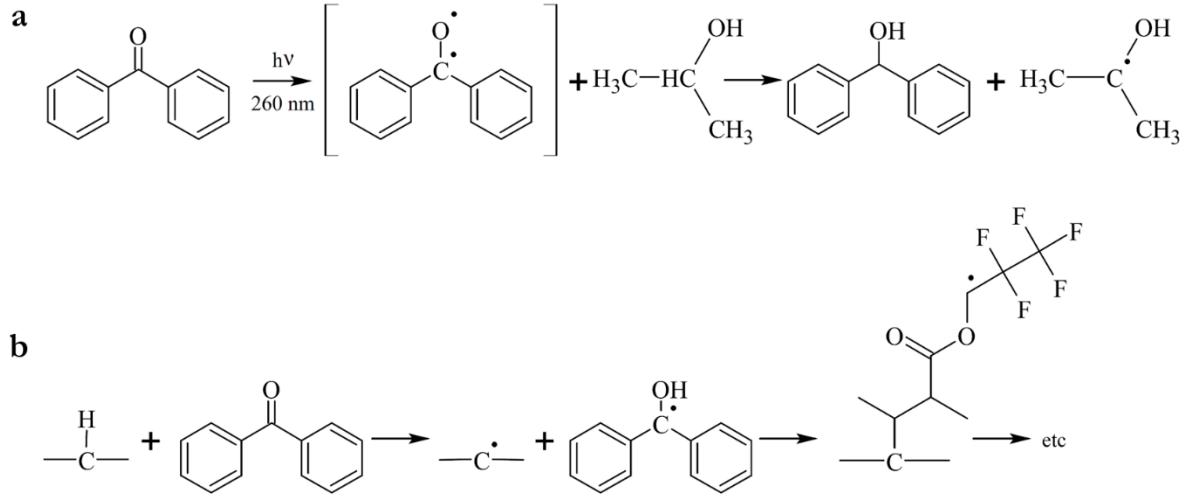

Figure 2.6: Scheme of the (a) initiation process by benzophenone, and (b) photografting of the polyHEMA surfaces with 2,2,3,3,3-pentafluoropropyl methacrylate (PFPMA).

Photografting, also known as photoinitiated graft-polymerization, is a versatile method for photoinitiated modification of polymer surfaces. The mechanism of the photografting was proposed by Råndy et al [92]. It was suggested that the photoinitiator could be excited to a singlet state (S_1) and later transform into triplet state (T_1) by intersystem crossing in the presence of UV-light. The triplet molecules can abstract hydrogen from the polymer surface, thus resulting in the radical formation on the surface. In this work, benzophenone was used as a photoinitiator. Under the UV-light benzopnenone gets excited and reacts with a co-initiator such as isopropanol to generate free radicals on the surface.

For photografting bottom glass plates the polymer samples were wetted with the photografting mixture 1 and covered with a fluorinated glass plate. The sample was irradiated for 30 min with an intensity of 11.5 mW/cm^2 by UV-light at a wavelength of 260 nm. The photografted sample was washed with ethanol and acetone and dried using an air gun. For the preparation of the patterned polymer surfaces, containing distinct superhydrophilic-superhydrophobic regions, the photomask of desired design was used.

2.3.5 Chemical modification of the grooved polyHEMA surfaces

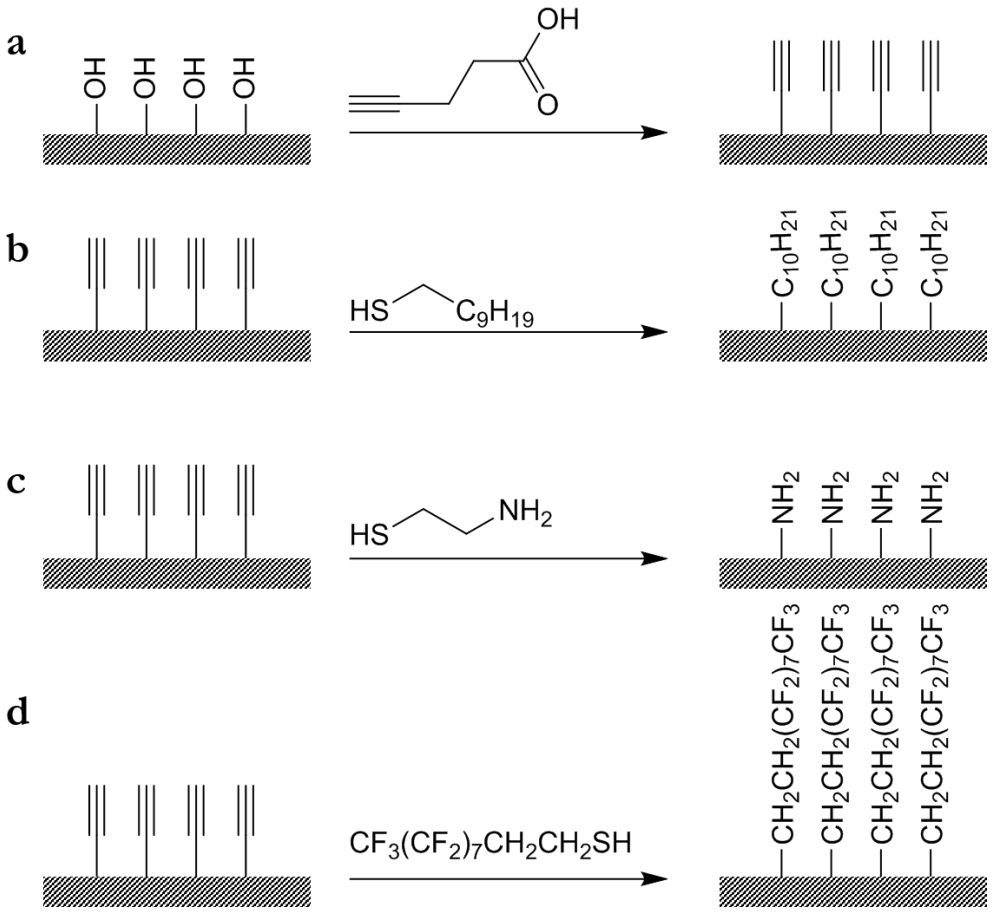

Figure 2.7: Schematic description of the chemical modification of the grooved spolyHEMA surfaces with (a) alkyne, (b) 1-decanethiol, (c) cysteamine, (d) 1H,1H,2H,2H-perfluorodecanethiol.

Firstly, two glass plates coated with a HEMA-EDMA layer were immersed into 50 mL of dichloromethane solution containing 4-pentynoic acid (111.6 mg, 1.14 mmol) and catalyst 4-(dimethylamino)pyridine (DMPAP) (56 mg, 0.46 mmol). Then, the coupling reagent N,N'-

diisopropylcarbodiimide (DIC) (176.5 µL, 1.14 mmol) was added to the solution cooled to about 0°C, and the solution was stirred at RT for 4 h. The plates were then washed extensively with acetone and kept in ethanol for several minutes, followed by drying.

Afterwards the substrate can modified with the respective thiol. The solutions of 1-decanethiol (5 vol%) or 1H,1H,2H,2H-perfluorodecanethiol (5 vol%) in acetone or cysteamine hydrochloride (15 wt%) in ethanol were used. These thiol solutions were not degassed prior to use. The alkyne polymer layer was wetted with the respective thiol solution and covered with a fluorinated quartz slide (25×75×1 mm, width×length×thickness). All of the fabrications of superhydrophobic or superhydrophilic layers using thiol-yne reactions were performed by UV irradiation for 60 seconds (12.0 mW/cm², 260 nm) without photoinitiator under ambient laboratory conditions. After the reactions, the samples were washed extensively with acetone and dried with a nitrogen gun.

2.4 WCA measurements

Water contact angles (WCA) were evaluated with UK1117 camera (EHD imaging GmbH, Germany), 5 µl syringe (Hamilton, Switzerland) by a sessile drop measuring method. The advancing and receding WCAs were determined by consecutive addition and subtraction of MilliQ water to the droplet. The measurements of WCAs were repeated at least three times. The calculation of WCA was performed using ImageJ Drop Analyzer plug-in.

2.5 SEM measurement

The surface and cross-section morphologies of HEMA-EDMA polymer films and its derivatives were analyzed using the ZEISS Leo 1530 (Carl Zeiss NTS GmbH, Germany; (INT, KIT)) scanning electron microscope after gold sputtering (15 nm) using the Balzers Union MED 10 (INT, KIT).

2.6 DLS measurement

Firstly, the polymer film was scratched by scalpel into the Eppendorf tube and 1 ml of ethanol was added. The solution was sonicated for 1 min and left overnight. Before the measurement was taken the sample was centrifuged at 1 rpm for 1 min and the supernatant was taken for measurement. Particle size distribution was measured on the Zetasizer Nano (Malvern).

Each measurement consisted of the 11 runs that gave averaged values. Each sample was measured 6 times and 3 independently made samples were measured. From these results size distribution of the particles was analyzed. The size distribution was characterized by following parameters: percentage of the particle population relative to the total population, particle size (***d)***, and full width at half maximum height (*w*).

2.7 Roughness measurements

Surface profiles and roughness of the samples were measured by FRT Microprof® 100 (IAI, KIT). The profile was measured for 4.8 mm with 0.4 mm cut-off in the beginning and the end of the measurement.

The sensor frequency was 100 Hz. The principle of measurement is based on the chromatic distance measurement. White-light is focused on the surface by measuring head with a strongly wavelength-dependent focal length. The spectrum of light scattered on the surface creates the peak in the spectrometer. The wavelength of the peak is used to determine the height of the sample. Advantage of this method is that it can measure transparent as well as not transparent, reflective or light absorbing samples.

Surface area profile was measured using Sensofar S neox (IAI, KIT). As the light source blue light was used (460nm) and 50X objective was used (NA 0.8, optical resolution 0.17 μm, vertical resolution 3 nm). The principle of the measurement is based on the confocal imaging, where out of focus light is eliminated. The sample is scanned in the vertical steps, so that every surface point passes through the focus. The height of the surface is found by the detection of the narrow axial response. As only a small local areas are illuminated at each step, the obtained images are of high resolution.

Roughness factor r was calculated from obtained surface profile by dividing the area of the actual surface to the apparent surface area.

Roughness parameters that were calculated: arithmetic mean deviation (Ra), root mean square deviation (Rq), maximum profile peak height (Rp), maximum profile valley depth (Rv), and skewness (Rsk). The definitions of the roughness parameters are following.

$$Ra = \frac{1}{l}\int_0^l |Z(x)|\, dx$$

$$Rq = \sqrt{\frac{1}{l}\int_0^l Z(x)^2\, dx}$$

$$Rp = \max(Z(x))$$

$$Rv = \min\ (Z(x))$$

$$Rsk = \frac{1}{Rq^3}(\frac{1}{l}\int_0^l Z(x)^3\, dx$$

2.8 Measurement of water spreading in the micro-channels

The flow in the micro-channel was visualized using Nikon Coolpix S8000 and AVS Video Editor 4.2. The flow velocity was measured by the following equation $v = d/t$, where d is the distance the rhodamine solution travelled and t is time of travel.

2.9 Cancer cell experiment

All cancer cell experiments were performed in collaboration with Dr. Alexander Efremov (KIT).

2.9.1 Cell culture

Red fluorescent rat mammary carcinoma MLTy-mCherry was kindly donated by Prof. Jonathan P. Sleeman (Institute of Toxicology and Genetics, KIT, Germany). Human Cervical tumor cell line HeLa

expressing GFP was purchased from BioCat (Heidelberg, Germany). All cell lines were cultured using DMEM, supplemented with 10% FBS, 100 u/ml penicillin and 0.1 mg/ml streptomycin. Cells were cultured at 37°C in a humidified atmosphere of CO_2 and 95% air. The initial cell seeding numbers were 5–10 × 10^3 cells/cm^2.

2.9.2 Cell cross-contamination assay

Polymer patterns were prepared according to the Section 3.3.4 with 3 × 10 mm cm adjacent rectangles with 500 μm borders. Appropriate volume of cell suspension was pipetted onto each hydrophilic area to fill the pattern's contour. MLTy-mCherry (red) and HeLa (green) cells were seeded at concentration 50 × 10^3 cells/cm^2 into neighboring rectangular patterns. The cells were cultured for 18 h inside isolated compartments. Afterwards patterns were connected, washed several times with PBS and immersed into the same medium. Further, cells were co-cultured for 24 h, 48 h and 72 h and fixed with 4% formaldehyde. Areas with patterned cells were analyzed by the Keyence BZ-9000 (Japan) fluorescence microscope. The cross-contamination between the compartments was calculated based on the cell number inside opposite compartment with ImageJ. The obtained numbers were normalized to the total number of cells.

2.9.3 Cell motility assay

HeLa GFP expressing cells were seeded at concentration 50 × 103 cells/cm2 on the micro-rough grooved, nano-rough polyHEMA surfaces and on the Petri dish. The cell motility assessment was done be the time-lapse microscopy at 37°C in a humidified atmosphere of CO_2 and 95% air using Axiovert 200M (Zeiss). The cells were observed for 24h.

The images were analyzed by ImageJ software. Individual movements of 10 cells were tracked. Based on the obtained cell coordinates speed (S), translocation (T), displacement (D) and length of the path (L) were calculated. The cell displacement (D) was defined as the length of the line between the starting and ending points of cell movement, whereas length (L) is the total length of the path that cell travelled. Cell speed (S) was defined as $S = L/t$ and cell translocation as $T = D/t$.

2.10 Stem cell experiments

All stem cell experiments were performed in collaboration with Dr. Zhang Ping (KIT)

2.10.1 Cell culture

The mouse embryonic stem cell line D3 was cultured in GlutaMAXTM-1 medium (Invitrogen) supplemented with 15% ES FBS (PAA), 0.1mM β-mercaptoethanol, 1% penicillin/streptomycin and 1000 units/ml LIF at 37°C/5% CO_2/ 95% humidity. mES cells, cultured on the gelatin for one passage(p1 cells) were used for seeding on the surfaces. For the stem cell proliferation study 1 Million cells were seeded into 15 cm Petri dish. mES were cultured for 4 passages each consisting of 4-5 days. After each passage cells were trypsinized for 1 min with 1% trypsin solution, counted and seeded into new surfaces.

2.10.2 Cell lysis

Cells were washed with PBS, and lysed in NP40 lysis buffer (50 mM Tris pH 8.0, 150 mM NaCl, 5 mM EDTA, 1% NP40, 1 mM PMSF) for 10 min on ice. The protein extract was cleared by centrifugation at 13,000 g for 10 min at 4°C.

2.10.3 Determination of the protein concentration

The protein concentration of cell lysate was determined by the method of Bradford. First, 2 µl cell lysate was mixed with 500 µl Bradford solution (AppliChem). For the blank control, 2 µl NP40 lysis buffer was used. The standard curve of protein concentration was generated by adding serial dilutions (2 µg - 20 µg) of BSA (bovine serum albumine) in 500 µl Bradford solution. Then, 150 µl of the mixtures were pipetted into a 96-well plate, and measured via an ELISA reader (ELx808 Ultra Microplate Reader, Bio-Tek). Finally, the protein concentration was calculated by the software program (KC4 version 3.01).

2.10.4 SDS-PAGE and Western blotting

30 µg of total protein in 1x sample buffer (2% sodiumdodecylsulfate (SDS), 80 mM Tris pH6.8, 10% glycerol, 5% 2-mercaptoethanol, 0.001% bromophenol blue) were heated for 5 min at 95°C, loaded onto an SDS-10 % polyacrylamide gel, separated by electrophoresis and transferred onto a polyvinylidene difluoride membrane (Millipore) using the Trans-Blot Turbo semi-dry transfer system (Bio-Rad). The membrane was blocked for 60 min in 5% BSA (in 0.2% Tween-20 in TBS, TBST) and incubated overnight with the primary antibody at 4°C. After washing 3 times for 5 min in TBST, the secondary antibody was added and incubated for 1 h. After extensive washing, the blots were developed by adding ECL (Pierce ECL Western Blotting substrate) and exposing the membranes against an X-ray film.

2.10.5 Alkaline Phosphatase Staining

Cells were washed twice by PBS and fixed by 2 ml of 4% paraformaldehyde solution for 20 min. Thereafter, cells were washed 3 times with 5 ml Tris-maleat buffer (1 M maleic acid, 0.02 M Tris, pH 9.0) for 5 min. The activity of alkaline phosphatase was developed by incubation with the reaction buffer (0.1 % Fast Red TR Salt, 0.02% Naphtol AS-MX Phosphate, and 0.08 % MgCl2 in Tris-maleat buffer) for 10-20 min. The positive clones which stained in red were photographed by a Keyence Biorevo BZ-9000 light microscope. The obtained images were analyzed using image J and built-in Keyence software.

Chapter 3

Results and discussion

3.1 Superhydrophobicity of micro-rough protruded and grooved surfaces

3.1.1 Background

Interest for superhydrophobic and superhydrophilic surfaces have increased greatly in the last decade as the studies of natural nonwettable surfaces emerged and their artificial substitutes were used as water-repellent and self-cleaning [93], [94], antiadhesive and antifouling [95]–[97] surfaces as well as in microfluidic [98], and biotechnology applications [99], [100].

Phase separation is a widely used method for the creation of superhydrophobic and superhydrophilic porous polymer films [101], [102]. This method is quick, cheap, and does not require expensive equipment. The method is based on a formation of two phases when a multicomponent mixture undergoes some change of environment, such as temperature or pressure. As a result of phase separation, a bicontinous structure can be formed (Figure 3.1). In this structure the newly formed phases form a 3D interpenetrating network. If one of the network components solidifies when the bicontinous structure is formed, the second liquid phase could be removed. Since the solid structure is continuous, the liquid removal does not necessarily lead to the destruction of the solid network. The solid structure parameters, such as pore size, can be controlled via altering different parameters of the composition of the initial multicomponent mixture or other parameters of the process of phase separation such as rate of solidification or temperature.

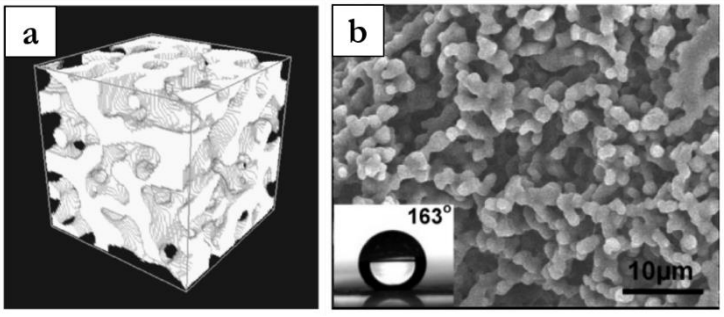

Figure 3.1: Examples of phase separation (a) model of a bicontinuous structure [103] American Physical Society, Copyright 2001; (b) phase-separated poly(*tert*-butyl acrylate)-*block*-poly(dimethylsiloxane)-*block*-poly(*tert*-butyl acrylate) triblockcopolymer films [104] American Chemical Society, Copyright 2005.

The porous structure of the polymer provides high roughness and polymer wetting properties depend on the monomer used. Polymerization conditions define size of the polymer globules, and the thickness and morphology of the polymer film. As a result, the biggest advantage of this method is versatility and simplicity of production of polymer surfaces with defined properties. However, while porous structure of the polymer may be advantageous for superhydrophilic wetting, it also leads to the increased pinning of the contact line and increases contact angle hysteresis (CAH).

In this section the effect of the surface topography and hierarchy on the superhydrophilic and superhydrophobic properties of the surface was examined. In order to study this, the lift-off method was developed for the simultaneous formation of the surfaces with complementary surface topography. Protruded and grooved poly(2-hydroxyethylmethacrylate-*co*-ethylene dimethacrylate) (polyHEMA) and poly(butyl methacrylate-*co*-ethylene dimethacrylate) (polyBMA) surfaces were prepared. The prepared surfaces were characterized by WCA, SEM, and roughness measurements and their surface morphology and wettability were compared. Additionally, surface properties of photografted and chemically modified polyHEMA films were studied.

3.1.2 Experimental details

All polymer films were prepared on 1 mm thick glass slides as described in Chapter 2. The polymerization mixture was poured into the mold made of two modified glass plates as described in section 2.3.1. Plates were separated with 75 μm thick poly imide spacers to define polymer thickness. The mold was placed under UV-light for 15 minutes. After UV-light irradiation the two glass plates were separated by a scalpel. The hardened polymer broke and a polymer film was attached to both glass plates. Films were washed extensively using ethanol and stored in methanol.

WCA measurements were made for all films according to the procedure described in Section 2.4. SEM imaging was done for all polymer films using ZEISS Leo 1530 microscope described in Section 2.5. DLS measurements were done for grooved surfaces according to the procedure outlined in Section 2.6. Roughness measurements were performed using optical and confocal profilers according to the procedure described in Section 2.7.

3.1.3 Surface properties of protruded and grooved surfaces

Protruded and grooved surfaces were produced using the lift-off approach. Previously, a similar method of producing porous polymer films was utilized [101]. However, the polymer mold was created by one modified glass plate (top plate relative to the UV-light source) and one fluorinated glass plate (bottom plate relative to the UV-light source). As a result, after separation of the glass plate the polymer film was

attached solely to the modified glass plate. There was no polymer attached to the fluorinated plate, due to its low surface energy. In contrast, in the lift-off approach polymerization mold comprised of two modified glass plates. The utilization of the two modified glass plates led to the feasible chemical bonding of the polymer to both glass slides. In this case, during the separation of the glass plates, the polymer film was broken and the surfaces with protruded and grooved morphologies were formed (Figure 2.5). The difference in surface topographies of two glass plates might be caused by the unequal polymerization in the mixture. As the UV-light goes through the mold, it is partially absorbed and scattered by the polymerization mixture. This might lead to the gradual decrease in UV-light intensity throughout the thickness of the mold. As a result, the polymerization process on the top and bottom of the mold would differ. After the polymerization, the mechanical properties of the polymer would be weaker at the bottom of the mold. This might lead to the easy breaking of the polymer film in proximity of the bottom glass plate and formation of protruded (top plate) and grooved (bottom plate) topographies, respectively.

Surface morphology of protruded and grooved polyHEMA surfaces. Superhydrophilic poly(2-hydroxyethylmethacrylate-*co*-ethylene dimethacrylate) (polyHEMA) surfaces were prepared on glass substrates using polymerization mixtures with different porogen compositions (see Table 2.1). The total porogen content was kept at 60 wt% in all the polymerization mixtures and various 1-decanol cyclohexanol ratios were used to change polymer globule size. The morphologies of the protruded and grooved polyHEMA surfaces were investigated using SEM (Figure 3.2).

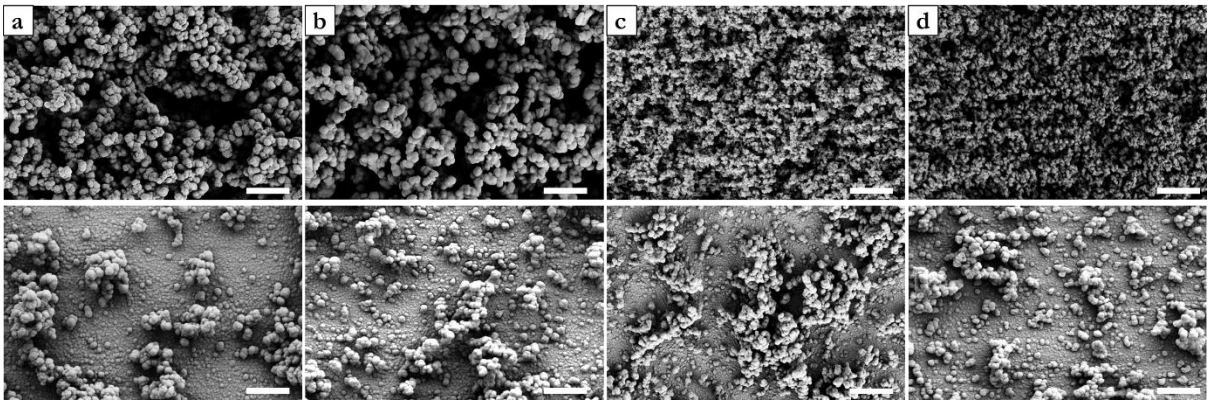

Figure 3.2: Surface morphology images by SEM of the protruded (top row) and grooved polyHEMA surfaces (bottom row). Polymer compositions: (a) HA, (b) HB, (c) HC, (d) HD. Scale bars 5 μm.

It was found that the lift-off separation process of the glass plates does not occur uniformly, creating special surface texture on both glass plates in a complementary manner. All tested surfaces showed either protruded topography (top row images in the Figure 3.2) or grooved topography (bottom row images in the Figure 3.2) irrespectively of the polymer composition. Decreasing content of 1-decanol led to a linear decrease in the globule size (Table 3.1). When 1-decanol was the only porogen in the mixture the porous surface HA with globule size of ~650 nm was obtained. The lowest content of 1-decanol used was 30% and the obtained polymer surface HD had a globule size of ~200 nm. The decrease of the 1-decanol amount below 30% resulted in a further decrease of the globule size and resulted in a stronger cohesion between the glass plates and inhomogeneous separation of the plates.

It was found that the globule size differed for protruded and grooved surfaces. The globule size depends on the onset of the phase separation. The obtained results might indicate that the phase separation in the bulk (protruded) and surface (grooved) polymer film followed different kinetics. Presence of the surface defects might promote nucleation process and hence facilitate phase separation. This could lead to the faster phase separation and result in larger globules at the surface.

Porogen composition in the polymerization mixture determines the kinetics of the polymerization process and globule size. 1-decanol is a poor solvent for polyHEMA in comparison with cyclohexanol. As a result, in the mixtures with higher 1-decanol content (HA, HB) the phase separation process occurs faster than in the mixtures with higher cyclohexanol content (HC, HD). When phase separation is fast, the surface has lower effect on the nucleation. Conversely, when phase separation is slow and the nucleation is limited, and the surface effect is more pronounced. Thus, the surfaces with high cyclohexanol content (HC, HD) show bigger differences in the globule size between protruded and grooved topographies.

Table 3.1: Globule size for protruded and grooved polyHEMA surfaces produced using different polymerization mixtures: HA, HB, HC, HD. The polymer globule size was measured on the SEM images using ImageJ software.

	Mix	**Protruded**	**Grooved**
Globule size, nm	HA	657±91	678±156
	HB	596±82	573±126
	HC	387±80	450±89
	HD	213±32	326±63

The protruded surface consisted of polymer globules assembled in the porous network. The polymer porosity was irregular, due to uneven breakage of the film. The polymer thickness was 64±0.86 μm. On the grooved surface polymer globules were compactly assembled in the disjointed agglomerates of about 9 μm, which were separated from each other by the thin layer of polymer. The distance between the aggregates varied between 5 and 20 μm. In between the piles, the polymer was permeated by narrow cracks of ~10 nm in width. Thickness of the polymer varied greatly from 1 to 3 μm with an average of 1.79±0.94 μm. The possible explanation of the thickness difference between protruded and grooved surfaces lies in the setup of film preparation. During the preparation of the polymer, the UV-light intensity was higher at the top of the mold and after separation the thicker polymer film was attached to the top glass plate.

Surface profiles of the protruded and grooved samples were compared using optical microprofiler (Figure 3.3). It was shown that, similarly to the SEM results, protruded surfaces had the height deviations (Z- values) mostly below the reference plane, due to its porous structure. Conversely, grooved surface had Z-values above the reference plane as the polymer globules form aggregates on the glass plate. Roughness factor r was obtained from surface profile by calculating the ratio of the actual surface area to the projected surface area. The found values of r for both surfaces were 1.14. This implies that while surface area of the both samples is the same - surface topography is actually different.

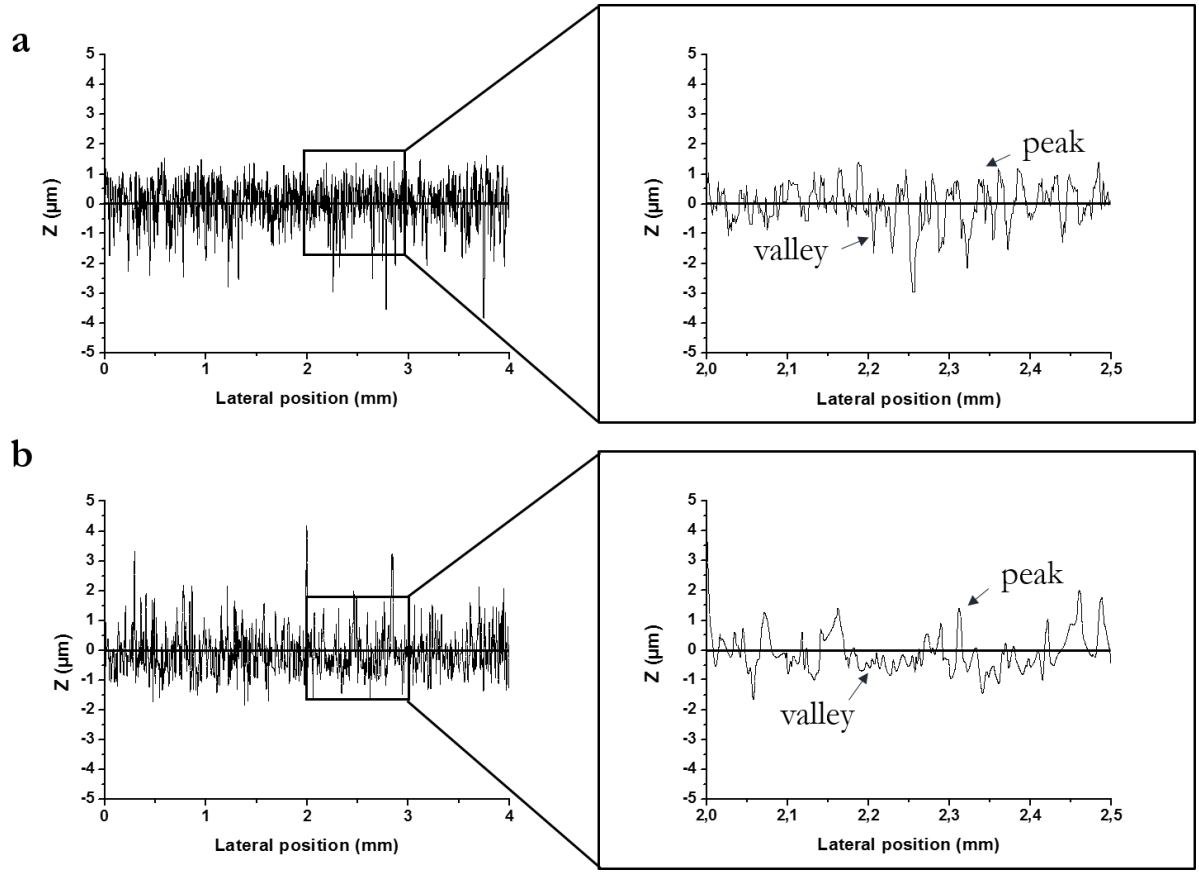

Figure 3.3: Surface linear profile showing height deviations (Z-values) relative to the mean line for (a) protruded and (b) grooved polyHEMA surfaces. Polymer composition HC.

Altitude roughness coefficients such as arithmetic mean deviation (*Ra*), root mean square deviation (*Rq*), maximum profile peak height (*Rp*), maximum profile valley depth (*Rv*), and skewness (*Rsk*) were calculated as described in Section 2.7. For both surfaces *Ra* and *Rq* were quite close due to the similarities in their surface topography (Table 3.2).

Table 3.2: Roughness coefficients for protruded and grooved surfaces.

Surface	*Ra*, µm	*Rq*, µm	*Rp*, µm	*Rv*, µm	*Rsk*
Protruded	0.53±0.01	0.68±0.02	1.93±0.38	3.35±0.39	-0.66±0.2
Grooved	0.67±0.05	0.87±0.06	3.90±0.42	2.15±0.2	0.91±0.18

The difference in the *Rp* and *Rv* values showed the complementary nature of the both surfaces, since what is peak for one surface is valley of the other. Skewness parameter is a measure of the surface profile asymmetry relative to the mean line. The sign of the *Rsk* indicates whether the surface profile is skewed downwards (negative sign) or upwards (positive sign). Since the protruded and grooved polyHEMA surfaces possessed opposite surface topography, the sign of the skewness parameter *Rsk* should be opposite, while the absolute values should be quite close. And indeed, *Rsk* values showed that while protruded surfaces were skewed downward, grooved surface is skewed upward relative to the average line.

These results indicate mostly presence of the deep valleys on the protruded surface and high peaks on the grooved surface. Due to the difference in the surface topography of protruded and grooved surfaces, the wettability of both surfaces would greatly differ. The presence of the sharp polymer peaks on the grooved surface leads to small contact with placed water droplet. As a result water removal would be easier and the surface would have higher receding water contact angle (WCA). Deep valleys of the protruded surface promote fast water spreading, however they also result in the pinning of the contact line during receding. Thus the grooved surface would have a smaller CAHs compared to the protruded surface.

Surface wettability of protruded and grooved polyHEMA surfaces. The influence of the surface roughness on the wetting properties is described by the Wenzel model. According to this model, the presence of the surface roughness enhances intrinsic hydrophilic or hydrophobic properties of the surface [22]. Since the objective was to study the effect of surface roughness, toporgaphy and morphology on the wetting properties, smooth polyHEMA polymer film was examined first. The smooth surface was prepared using polymerization mixture without any porogens, hence the surface did not have any pores or globules. From the SEM image of surface morphology (Figure 3.4) it is clear that the surface was indeed quite smooth. WCA of the smooth surface was 57°, due to inherent hydrophilicity of HEMA molecule and absence of the surface roughness.

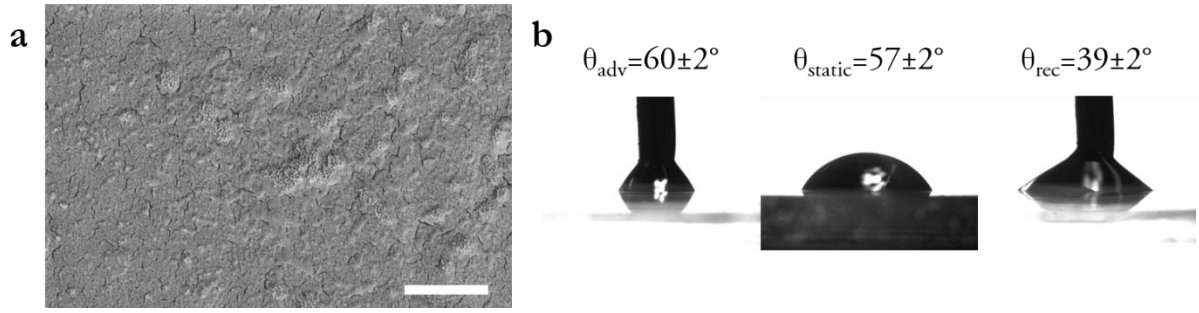

Figure 3.4: Smooth polyHEMA surface characterization (a) SEM image, (b) WCA measurement. Scale bar is 1 μm.

Equilibrium WCA may differ from the measured contact surface if the surface is structurally and chemically not homogeneous. The Tadmor equation relates equilibrium WCA with surface advancing and receding WCA. Using the Tadmor equation 1.19 the equilibrium WCA was calculated for the smooth surface and was found to be 53°, which was close to the experimentally found value of static WCA indicating that indeed the produced surface had negligent effect of surface inhomogeneity.

Wetting properties of the protruded and grooved surfaces were examined using WCA measurement (Figure 3.5). Both surfaces were found to be superhydrophilic with WCA below 10°, but their interaction with water was quite different.

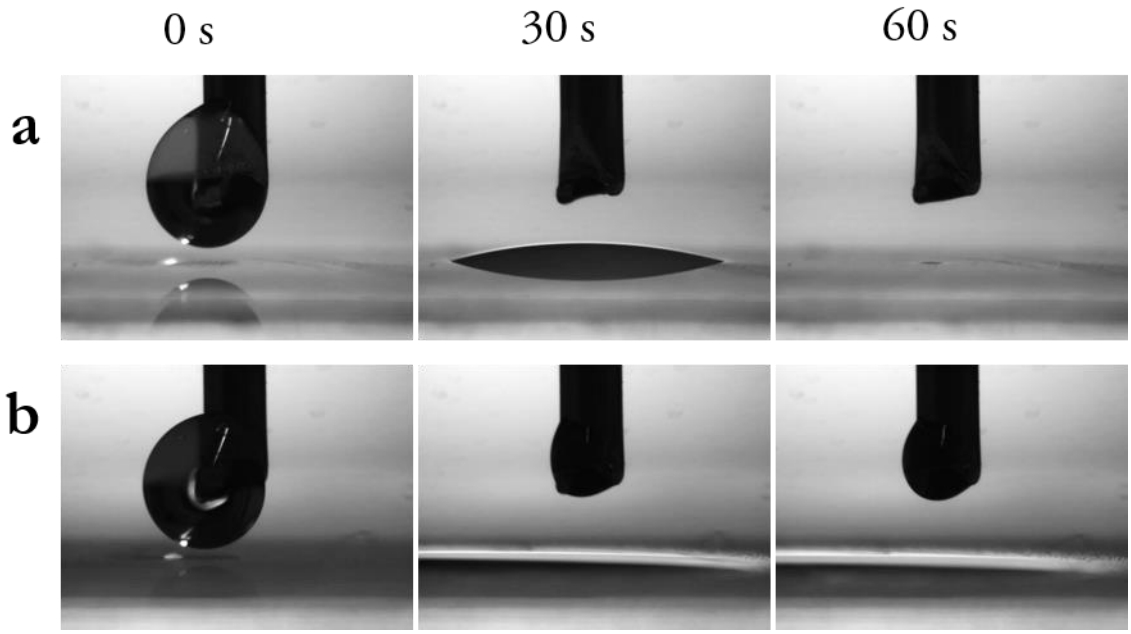

Figure 3.5: Photographs of water droplets spreading and adsorbing on the (a) protruded and (b) grooved polyHEMA surfaces. Polymer composition HC.

Upon contact with protruded surface, the water droplet quickly soaked into the pores and in less than 1 minute the surface was completely wet, showing no water film on its surface. Whereas on the grooved surface, water droplet was unable to soak in, due to its low thickness. However, water spread greatly on the surface and formed a thin liquid film. All tested composition showed the same superhydrophilic behaviour due to their porous structure.

Surface morphology and wetting of protruded and grooved polyHEMA surfaces after photografting with PFPMA. Superhydrophilic polyHEMA surface can be also further functionalized using photografting with 2,2,3,3,3-pentafluoropropyl methacrylate (PFPMA) [101]. PFPMA is a highly hydrophobic molecule due to the presence of fluorines, therefore after photografting the modified surface exhibits hydrophobic properties. Surface morphology and wetting properties of the smooth surface functionalized with PFPMA were characterizes using SEM and WCA measurements (Figure 3.6).

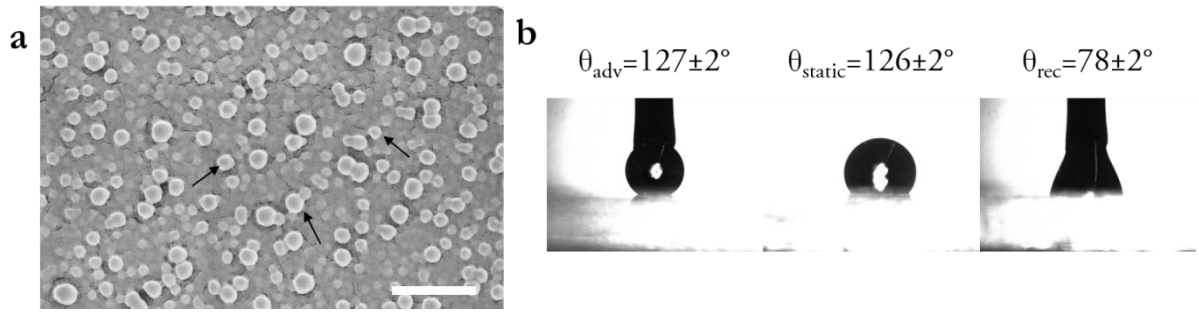

Figure 3.6: Smooth polyHEMA surface characterization after photografting with PFPMA (a) SEM image, (b) WCA measurement. Black arrows indicate photografted polyPFPMA globules. Scale bar is 1 μm.

It was found that after photografting the smooth polyHEMA surface was modified with a polyPFPMA nanoglobules. The size of the spherical photografted globules was 173±37 nm and they were

homogeneously distributed on the surface. The wetting properties of the surface also changed. WCA increased from ~57° to ~126° due to both- the surface roughness provided by the photografted globules and their hydrophobic nature. However, the surface also possessed 49° CAH, indicating that the surface was in the Wenzel state.

Surface morphology of the protruded and grooved polyHEMA surface after photografting with PFPMA was also studied using SEM. It was found that after the photografting, the surface morphology of the both surfaces was completely altered (Figure 3.7).

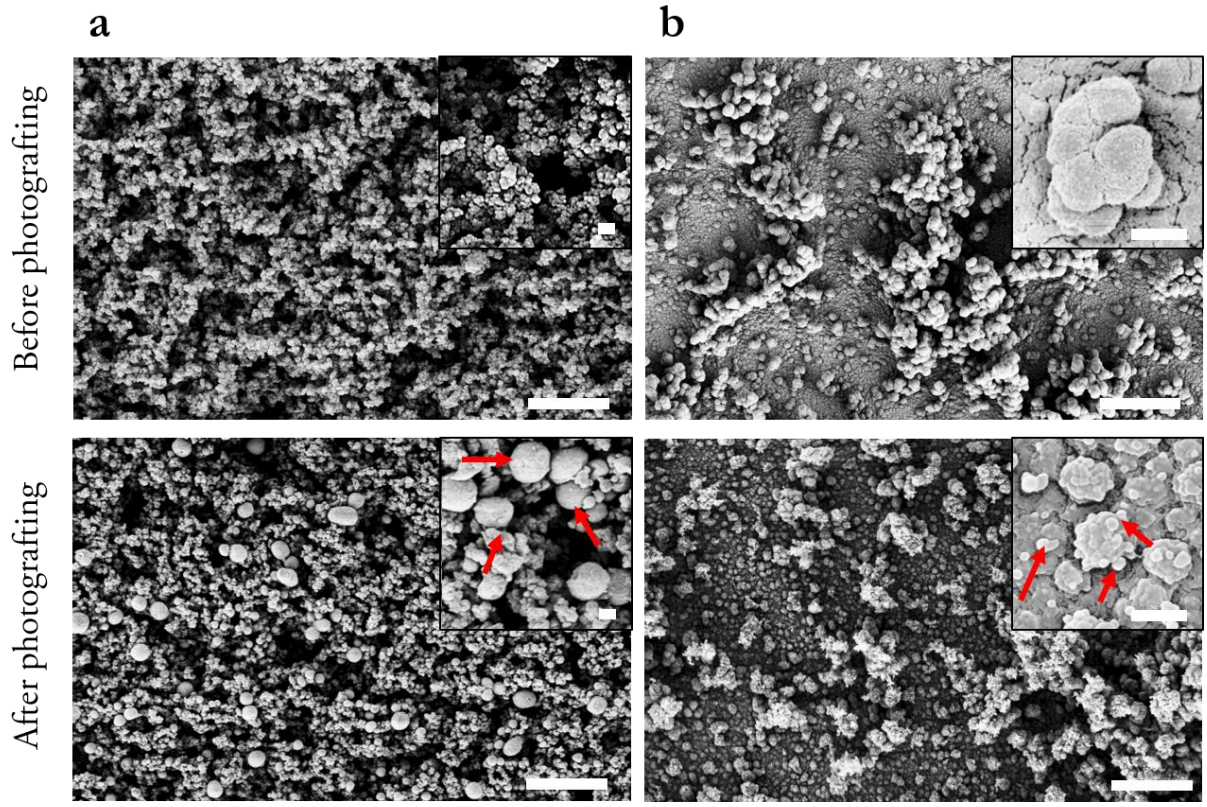

Figure 3.7: SEM images of (a) protruded, (b) grooved polyHEMA surfaces before and after photografting with PFPMA. The inlets show the magnified image of the polyHEMA and photografted polyPFPMA globules. The red arrows indicate photografted polyPFPMA nanoglobules. Polymer composition HC. Scale bars are 5 μm for full image and 500 nm for inlet images.

After photografting, the protruded and grooved surfaces were covered with additional "photografted polyPFPMA" globules (red arrows on Figure 3.7). Photografted polyPFPMA globules on the protruded surface were 801±281 nm in diameter and their size greatly varied (Figure 3.7a). The photografted polyPFPMA globules covered the entire grooved surface, both polymer agglomerates and the space between them. The size of the photografted polyPFPMA globules on the grooved surface was 89±23 nm (Figure 3.7b). In comparison with protruded surface, the amount of the photografted polyPFPMA globules on the grooved surface was around 30 times higher. The photografted polyPFPMA globules cover the polymer agglomerates from all the sides, effectively creating "raspberry-like" structures.

Protruded and grooved surfaces were modified by photografting with PFPMA under identical conditions. However, due to the different surface topography water behavior on these surfaces was different (Figure 3.8). The highest difference in the WCAs between protruded and grooved surfaces, was observed for the HD polymer composition (Table 2.1.). Advancing WCA for both, the protruded and grooved surfaces were 165° and 167°, respectively. However, the receding WCAs for protruded and grooved surfaces were 123° and 165°, respectively. As the result, CAH for protruded surface was 42°.

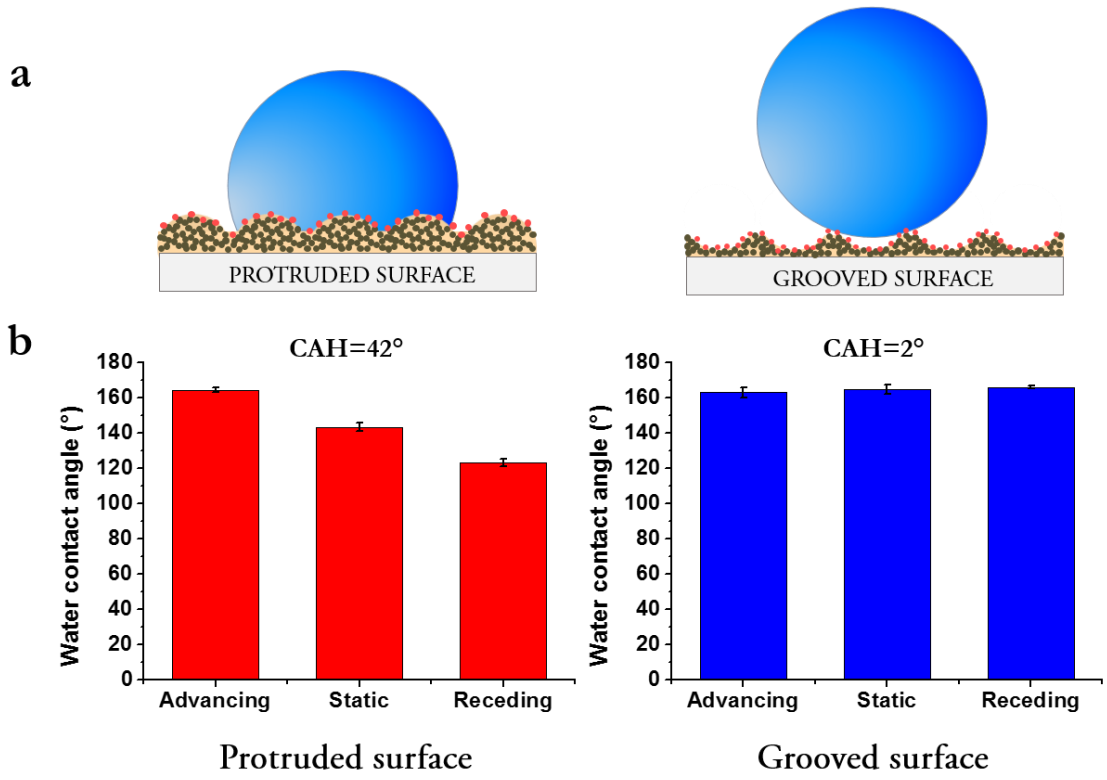

Figure 3.8: Comparison of the wettability of protruded and grooved polyHEMA surfaces after photografting with PFPMA. (a) Schematic drawing depicting interaction of water with protruded and grooved surfaces. (b) Water contact angles for protruded and grooved polyHEMA surfaces after photografting with PFPMA for HD polymer composition. Error bars are ± standard deviation

It can be concluded that the surface topography of the protruded surface promoted pinning of the contact line and resulted in the lower receding WCA. Conversely, the grooved surface topography led to the high receding WCA and low angle hysteresis. It was found that all surfaces, protruded and grooved, were highly hydrophobic with advancing WCA above 150° (Table 3.3).

Table 3.3: Water contact angles of protruded and grooved polyHEMA surfaces after photografting with PFPMA. Polymer compositions: HA, HB, HC, HD

		HA	HB	HC	HD
Protruded surface	**θ_{adv},°**	165±2	164±4	161±2	165±1
	θ_{static},°	151±3	157±2	150±4	144±3
	θ_{rec},°	136±4	148±2	143±3	123±2
	CAH,°	29	16	18	42
Grooved surface	**θ_{adv},°**	168±2	165±4	172±4	167±3
	θ_{static},°	165±3	162±3	170±3	165±3
	θ_{rec}, °	167±3	161±5	169±4	165±1
	CAH,°	1	4	3	2

The high hydrophobicity of these surfaces resulted from the combination of the surface roughness and hydrophobic nature of the photografted globules. However, all protruded surfaces were also characterized with large CAH ranging from 16° to 42°. Therefore, although the protruded surfaces were highly hydrophobic, they were not superhydrophobic. In contrast grooved surface had static WCAs above 160° for all compositions and also CAH below 5°. Low receding WCAs of protruded surfaces implies that the contact line is pinned during the decrease of the droplet volume. Low receding angles are characteristic for the Wenzel state, when liquid is filling the texture of the surface. High receding WCAs typically correspond to the Cassie-Baxter state since it has low contact area. In this state, water drop was resting on the polymer aggregates with air trapped in between. It should be noted that both protruded and grooved surfaces were polymerized using exactly the same polymerization mixture. Moreover, they are produced from the same glass mold and the only difference is that the protruded surface is the "top" glass slide directly irradiated with UV light, while the grooved surface is the bottom slide. This orientation leads to the asymmetric break of the porous polymer layer with the formation of the denser polymer protrusions in the case of the protruded surface and less dense polymer peaks with higher aspect ratio in the case of the grooved surface (Figure 2.5). This difference leads to the significantly decreased WCA hysteresis for the grooved surface and therefore superhydrophobic behavior. The observed results is an important advancement of the method for the fabrication of superhydrophobic porous polymer films by the phase separation approach.

WCAs above 150° and low CAH are both necessary conditions for superhydrophobic surface. It is thus vital to understand what surface characteristics provide desirable wetting properties. Low CAH of the photografted grooved polyHEMA surface can be attributed to either the special polymer surface topography of the grooved surface relative to the protruded surface, or to the effect of the hierarchical roughness introduced by the photografting. In order to investigate this effect, protruded and grooved surfaces were prepared using a poly(butyl methacrylate-*co*-ethylene dimethacrylate) (polyBMA), polymer with lower hydrophobicity than that of the polyPFPMA. Surfaces were prepared in exactly the same way as the

polyHEMA surfaces by the lift-off approach, however without photografting. Similarly, the protruded surfaces exhibited low receding WCAs and high CAH (Figure 3.9).

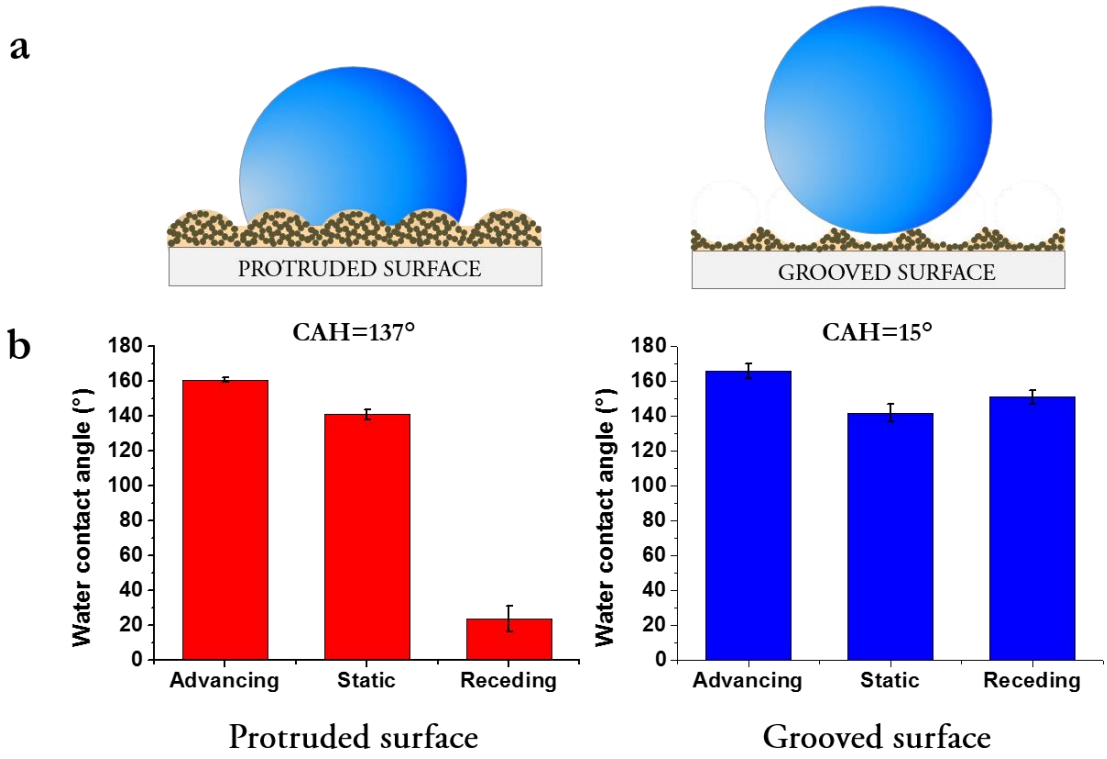

Figure 3.9: Comparison of the wettability of protruded and grooved polyBMA surfaces. (a) Schematic drawing depicting protruded and grooved surface at their contact with water drop. (b) Water contact angles for protruded and grooved polyBMA surfaces for HD polymer composition. Error bars are ± standard deviation

It was found that static WCAs for all protruded polyBMA surfaces were below 140° (Table 3.4.). The advancing WCAs were above 150° for all tested surfaces, while receding WCAs were ranging from 24° to 102°. The surfaces with the highest 1-decanol content, and thus largest pore and polymer globule size, had a receding WCA of ~100°. As the globule size was decreased further, the receding WCA was also decreased to ~20° for the HD surface. In comparison with the photografted protruded polyHEMA surface, protruded polyBMA surfaces showed lower static WCA and higher CAH. Grooved polyBMA surfaces showed highly hydrophobic properties, with static WCAs of ~150° and CAH of ~11°. This indicates that porous morphology of the protruded surfaces and roughness that it provides is not enough to ensure superhydrophobic properties of the film. This effect confirms that the observed decrease of the WCA hysteresis on the grooved polyHEMA surfaces. The morphology of the protruded surface on the other hand is not enough for achieving superhydrophobicity. In this case, the utilization of the photografting provides an essential tool for increasing hydrophobicity as well as hierarchical roughness.

Table 3.4: Water contact angles of protruded and grooved polyBMA surfaces.

		BA	**BB**	**BC**	**BD**
Protruded surface	θ_{adv}	157±2°	155±1°	154±1°	161±1°
	θ_{static}	124±4°	139±3°	133±5°	141±3°
	θ_{rec}	102±4°	103°±2	35±7°	24±7°
	CAH	55°	52°	119°	137°
Grooved surface	θ_{adv}	159±7°	154±10°	166±4°	166±4°
	θ_{static}	154±6°	154±2°	162±1°	142±5°
	θ_{rec}	148±5°	145±7°	155±10°	151±4°
	CAH	11°	9°	11°	15°

The presence of hydroxy groups enables the modification of polyHEMA surfaces by the chemical means. HC sample with 40 wt% of 1-decanol was chosen as a representative of the grooved polyHEMA surfaces. The chemical modification of the polyHEMA surface was based on the esterification of the hydroxy groups on the surface using 4-pentinoic acid, in presence of the catalyst (DMPAP) and a coupling agent (DIC). As the result of esterification, alkyne groups were introduced to the surface (Figure 2.7). The produced modified polyHEMA surface with alkyne groups subsequently reacted with 1-decanethiol or perfluorodecanethiol through thiol-yne reaction under UV-light (260 nm, 11.5 mW/cm^2). The surface morphology for all the surfaces was analyzed by SEM (Figure 3.10). As was previously noted, photografting with PFPMA results in the addition of photografted polyPFPMA globules to the polyHEMA surface. In contrast, polyHEMA surfaces chemically modified with decanethiol and perfluorodecanethiol showed the same surface morphology as the unmodified polyHEMA surfaces.

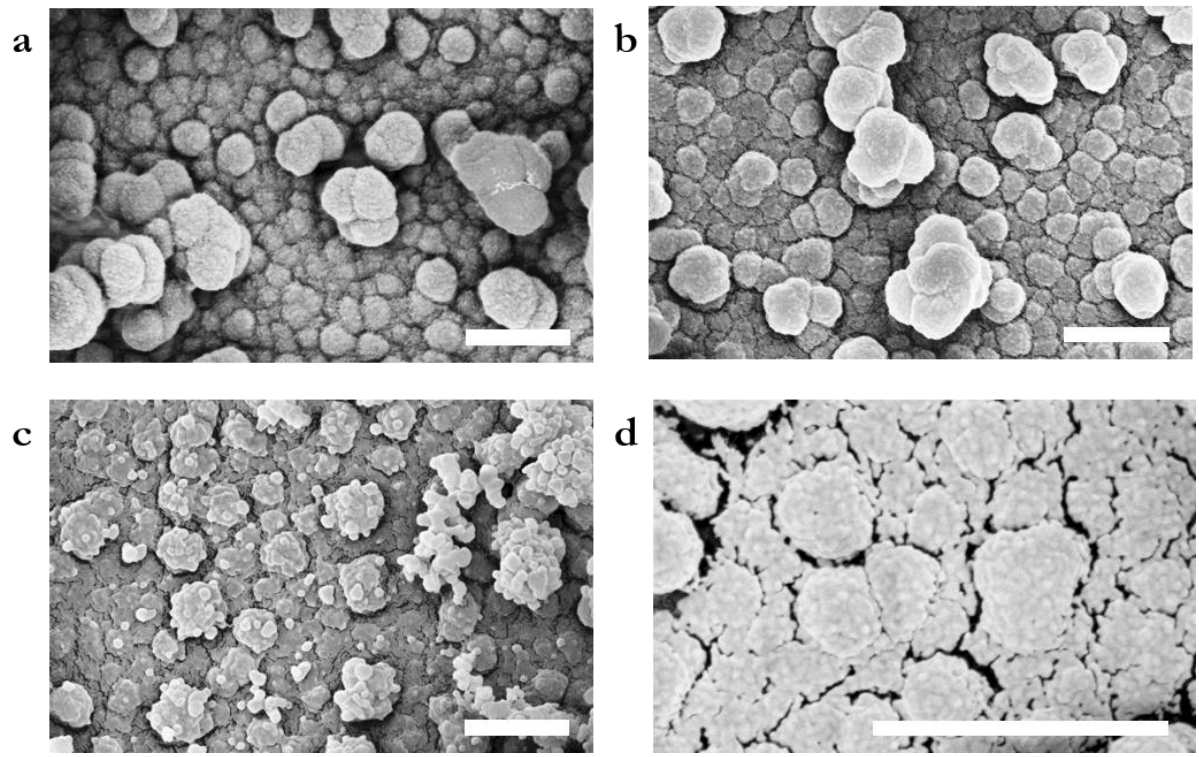

Figure 3.10: SEM images of the grooved polyHEMA surface (a) decanethiol modified and (b) perfluorodecanethiol modified, (c) photografted with PFPMA, (d) magnified image of the polymer globules of the grooved not modified polyHEMA surface. Scale bars 1 μm.

Wettability of the photografted and chemically modified surfaces were tested using water WCA measurements (Table 3.5.). All of the surfaces showed superhydrophobic properties with static WCAs >160° and CAH<5°. The WCA of 162° for decanethiol modified surface was the lowest compared to the photografted with PFPMA and perfluorodecanethiol modified polyHEMA surfaces. However, both photografted and perfluorodecanethiol modified surfaces had high static WCAs of 172° and 174°, respectively and CAH below 4°. Based on the SEM analysis, the morphology of the chemically modified surfaces did not change after the surface modification (Figure 3.10), however the functionalized surfaces showed very low WCA hysteresis, comparable to that of the photografted with PFPMA polyHEMA surface. This result indicated that surface morphology of the grooved polyHEMA was sufficient for the creation of superhydrophobic surfaces with WCAs above 160°. In other words, the secondary nano-sized polymer globules did not affect the CAH. On the other hand, the advancing WCA increased by 10° on both fluorinated surfaces (photografted with PFPMA and perfluorodecanthiol modified), suggesting that the absolute value of the WCAs depends on the chemical composition, while the roughness is more critical for the CAH.

Table 3.5: Water contact angles of grooved polyHEMA surfaces modified by photografting with PFPMA, and chemically modified with decanethiol and perfluorodecanethiol modified via thiol-yne reaction. Composition for all surfaces was HC.

	Photografted with PFPMA	**Decanethiol modified**	**Perfluorodecanethiol modified**
θ_{adv}	172±4°	164±3°	174±2°
θ_{static}	170±3°	162±4°	169±2°
θ_{rec}	169±4°	159±2°	170±3°
CAH	3°	5°	4°

The high magnification image of the grooved polyHEMA prior any modification was taken by SEM to investigate the structure of the individual polymer globules. It was found, that the surface morphology of the individual polymer globules was inhomogeneous. Observed polymer globules inhomogeneity was due to the presence of mesoglobules, which are small globular constituents of the bigger polymer globules. The mesoglobules possessed size of 27±5 nm, for the polymer globule size of ~450 nm. Each individual polymer globule consisted of ~100 mesoglobules. In contrast, the photografted PFPMA nanoglobules displayed size of ~ 90 nm. After photografting with PFPMA, the polymer globules were completely covered with photografted polyPFPMA nanoglobules and the mesoglobular structure of the individual polymer globules was completely not observed. The photografted polyPFPMA nanoglobules covered the polymer globules from all the sides and each polymer globules was covered by about 10 polyPFPMA globules.

3.1.4 Roughness and polymer globule size of the grooved surfaces

The roughness of the grooved polyHEMA surfaces was analyzed using a confocal profiler. The working principle of the confocal profiler is based on confocal imaging. During the measurement, out of focus light is eliminated. The sample is scanned in the vertical steps, so that every surface point passes through the focus, while out of focus light is eliminated. The corresponding topography maps (Figure 3.11) of the surfaces prepared using polymerization mixtures with different porogen contents were analyzed.

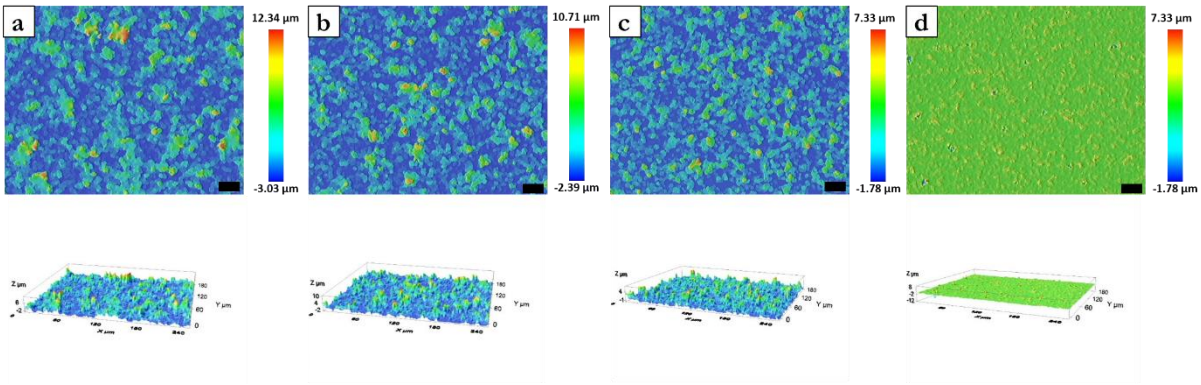

Figure 3.11: Topography maps of the grooved polyHEMA surfaces. Polymer compositions: (a) HA, (b) HB, (c) HC, (d) HD. Scale bars are 20 µm.

As the amount of 1-decanol decreases the surface becomes smoother, due to the reduced globule size. The grooved surface consists of sparse aggregates of globules with the height above average and relatively smooth space between the polymer piles. The surface with the lowest 1-decanol content (30%) and the smallest globule size has the lowest height difference between the polymer aggregates and smooth space. Also, as the surface becomes smoother, the polymer aggregates were distributed more homogenously on the surface.

The average area roughness (Sa) was calculated from the topography maps (Figure 3.12). Surface roughness increased steadily as the content of the 1-decanol in the polymerization mixture increased. The HA surface with the highest 1-decanol content had a globule size of ~680 nm and average area roughness of ~1600 nm, while the HD surface with the lowest 1-decanol content had globule size of ~140 nm and average surface roughness of ~520 nm.

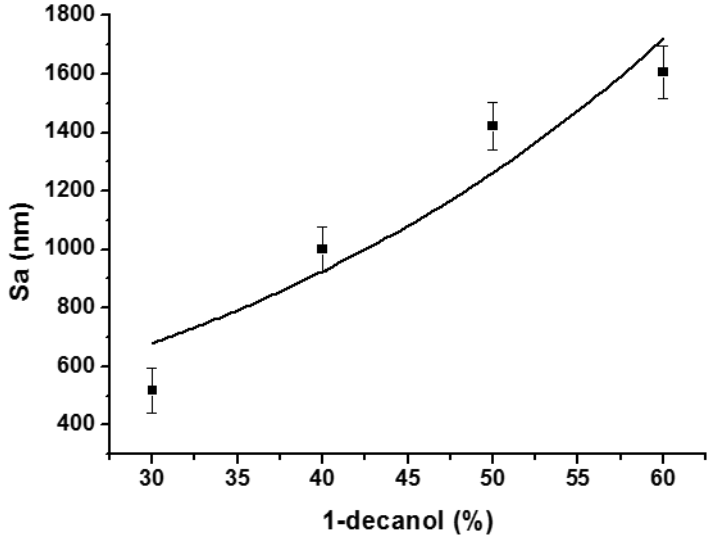

Figure 3.12: Dependence of the average surface roughness (Sa) of the grooved polyHEMA surfaces on the 1-decanol content in the polymerization mixture. Error bars are ± standard deviation. Solid line represents exponential fit of the data.

The size of the polymer globules was measured by SEM as was shown in Section 3.1.3 and the results were confirmed by DLS measurement (Figure 3.13). For the DLS measurement the porous polymer film was destroyed and dispensed in water to form a suspension of polymer globules that formed polymer monolith. After the dispersion of the polymer particles in the water, the solution was homogenized by the sonication. Sonication parameters were chosen as such to ensure the successful dispersion of the polymer particles, while simultaneously not destroying individual polymer particles. Thus, the solution was probably comprised of not only individual polymer particles, but also preserved particle agglomerates. The particle suspension was analyzed by DLS and the particle size distribution was obtained. Due to the high variation of the samples and use of three independent samples, there was large difference in the population of the different samples, which resulted in the large standard deviations. The size distribution was characterized by following parameters: percentage of the particle population relative to the total population and particle size (*d*).

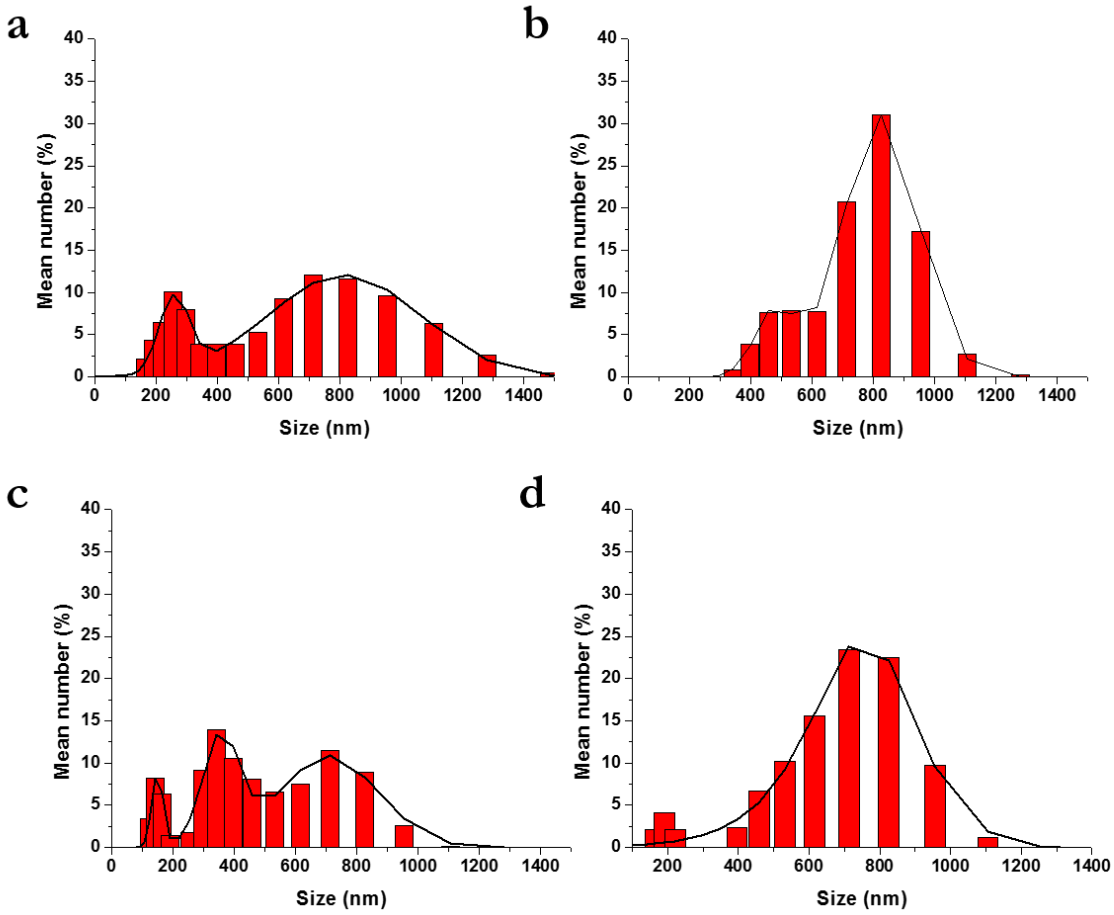

Figure 3.13: Particle size distribution for grooved polyHEMA surfaces with polymer compositions: (a) HA, (b) HB, (c) HC, (d) HD. Solid line represents Gaussian fit of two or three independent populations.

The particle size distribution for HA surface showed two peaks with Gaussian distribution. The first peak comprised 27% of the total particle population with d = 259 nm average size of the particle, whilst the second peak contribute 73% of the total particle population with d = 664 nm. The second surface HB particle distribution also consisted of two peaks: the first peak corresponded to 18.9% of the total particle

population with d = 470 nm, 81.1 % of the total particles belonged to the second peak with d = 805 nm. The third surface HC had particle distribution with three separate peaks. The smallest peak comprised 11% of the total particle population with d = 150 nm, the second peak possessed 41% of the total particle population with d = 344 nm, the third peak contributed 48% of the total population with d = 678 nm. The surface HD, which showed the smallest globules, gave the particle distribution that consisted of two peaks: the first one comprised 8.3% of the total population with d =191 nm, 91.7% of the total population gave rise to the second peak with d = 709 nm. The DLS results were in the agreement with the polymer globule size obtained from the SEM analysis.

Dependence of the polymer globule size on the porogen content was analyzed using SEM images (Figure 3.14). The polymer globule size increased from about 330 nm to 680 nm as content of the 1-decanol in the polymerization mixture increased from 30% to 60%. There are two porogens in the mixture that affect globule size: 1-decanol and cyclohexanol. Both porogens lead to the pore formation and the only difference is the size of the pores and polymer globules [89]. Hence reducing 1-decanol content to 0% (increasing cyclohexanol content to 60%) leads to a reduction of pore size to 330 nm.

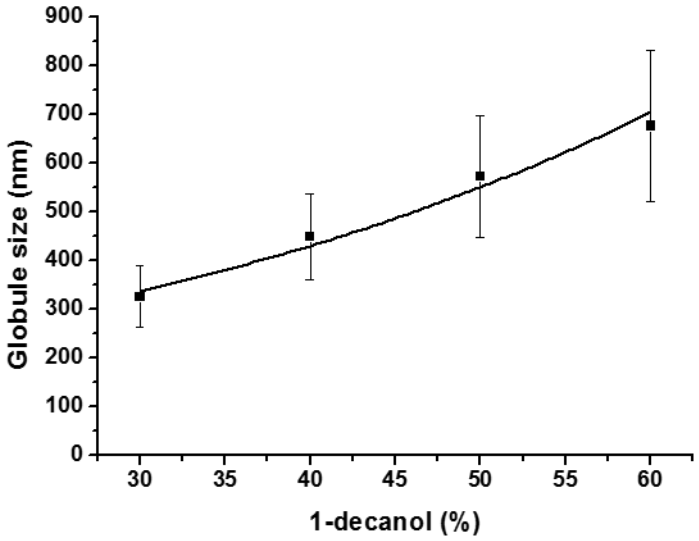

Figure 3.14: Dependence of the polymer globule size (measured by SEM) of the grooved polyHEMA surfaces on the 1-decanol content in the polymerization mixture. Error bars are ± standard deviation. Solid line represents exponential fit for the data.

As previously shown (Section 3.1.3), photografting of the polymer surfaces with PFPMA leads to a change in the polymer surface morphology. In order to estimate how strongly the presence of the nanoglobules formed after photografting changed surface roughness, the effect of the photografting on the smooth polyHEMA surface was examined by confocal profiler (Figure 3.15).

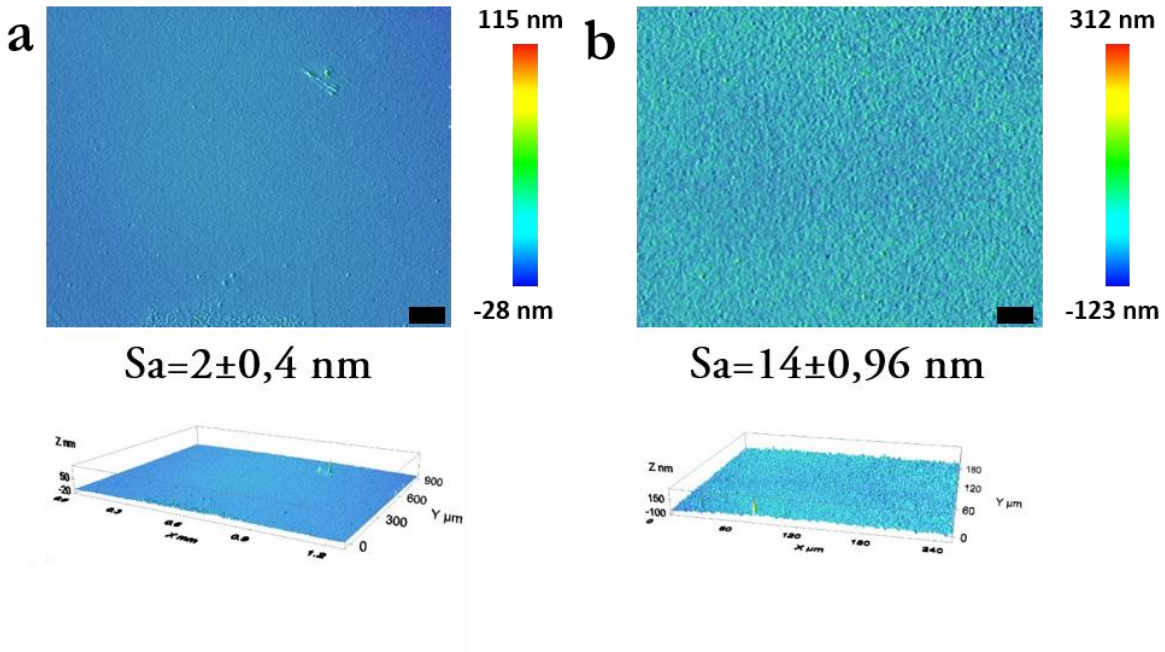

Figure 3.15: Topography maps of the smooth polyHEMA surface (a) before and (b) after photografting with PFPMA. Scale bars are 20 µm

The average area roughness of the smooth surface before photografting was ≈2 nm, due to the absence of any surface features or texture. After photografting, due to the presence of the photografted polyPFPMA globules, the average area roughness increased to ~14 nm. Sa value after photografting is also low, possibly due to the fact that the globules constituted only ~45% of the whole area and the rest of the surface is smooth.

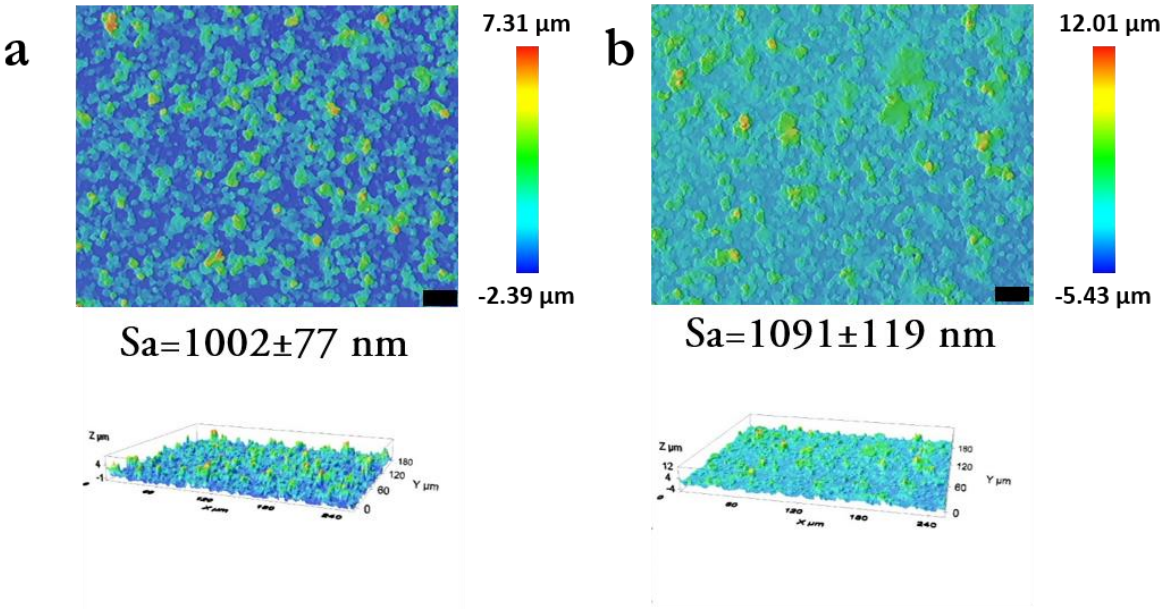

Figure 3.16 Topography maps of the grooved HC polyHEMA surface (a) before and (b) after photografting with PFPMA. Scale bars are 20 µm

Surface topography of the grooved polyHEMA surface before and after photografting was investigated using confocal profiler (Figure 3.16). Before photografting grooved polyHEMA surface possessed Sa of ~1000 nm, which increased to ~1090 nm after the process.

PolyHEMA surfaces prepared from different polymerization mixtures were characterized using confocal profiler, DLS and SEM analysis. It was shown, that surface roughness and polymer globule size increased with content of 1-decanol in the polymerization mixture. Additionally, it was found that after the photografting with PFPMA both smooth and grooved polyHEMA surfaces displayed an increase in the surface roughness.

3.1.5 Conclusions

The effect and influence of the surface topography and hierarchical structure on the wetting properties of the surface was examined. The lift-off method was utilized to produce surfaces with identical chemical composition, but different surface topography in one simple step. This approach is based on the separation of a polymer porous film prepared between two glass slides. Depending on the monomer used, the surfaces have either superhydrophilic (polyHEMA) or superhydrophobic (polyBMA) properties. Additionally, superhydrophilic surfaces could be turned superhydrophobic via photografting or chemical modification. Morphology, roughness and the wetting properties of the polymer on both glass slides were compared and influence of the surface topography on wetting was examined. Protruded surface had highly porous topography, whereas grooved surfaces consisted of disjointed agglomerates of polymer globules. Due to highly rough structure of both surfaces they have high WCA, however different surface topography lead to high CAH for protruded and low CAH for the grooved surfaces. This indicated, that surface topography of the grooved polymer is advantageous for superhydrophobic properties. However, just grooved surface morphology is not enough to ensure low CAH. Photografting with PFPMA of the superhydrophilic polyHEMA surface results in the formation of small globules and raspberry-like morphology of the polymer globules. By combination of the grooved surface morphology and hierarchical structure, polymer surface obtained superhydrophobic properties. Surface morphology, wetting, transparency and roughness of the grooved surface were analyzed. It was shown that globule size and surface roughness depend on the 1-decanol content in the polymerization mixture. Thus, surfaces with varied globule size and surface roughness could be made by controlling the porogen content.

3.2 Surface tension confined channels and Laplace micro-pump

3.2.1 Background

Microfluidics is a multidisciplinary field with a focus on the design of systems in which small volumes of fluids can be handled. It is widely used in the development of inkjet printheads, DNA chips, lab-on-a-chip technology, micro-propulsion, and micro-thermal technologies. It allows precise control and manipulation of fluids that are geometrically constrained to a small scale. The advantage of microfluidic systems lies in handling of the small liquid volumes and small size of the system [105]. This allows for a reduction in cost of the reagents as well as of the system in the whole. Additionally, microfluidic systems are beneficial for biological applications, when amount of the sample (for example DNA or protein) is limited.

Rigid polymer based microfluidic systems are widely used for creation of channels separated from the background by the physical borders. The poly(dimethylsiloxane) (PDMS) micro-channels are mostly used for this purpose, due to the ease of production, physical properties and economy [106], [107]. So called open microfluidic channels, created without any solid borders, offer unique advantages as they provide increased accessibility and simplicity of fabrication [108]–[110].

The lab-on-a-chip technologies use microfluidic devices where the use of external pumps to enable the flow of liquid is not always convenient. Removing external pumps can reduce the size and cost of a system. However, there are only a few microfluidic systems with miniaturized pumping systems. The Laplace pump principle is one of the few simple ways to generate liquid flow in a micro-channel without external pump [111]. The Laplace pump is created by two droplets of different size that are connected via a micro-channel (Figure 3.17).

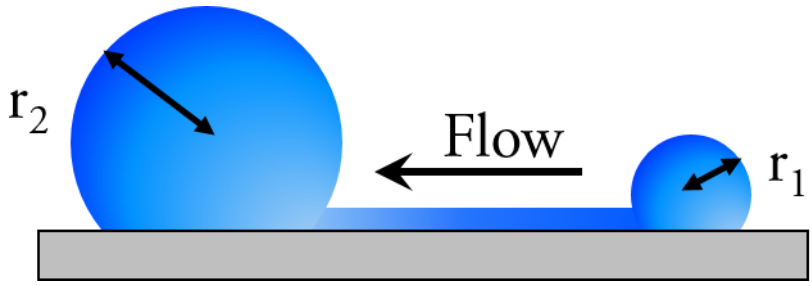

Figure 3.17: Schematic description of the Laplace pump system.

The pressure inside each of the individual drop is given by the Young-Laplace equation.

$$p = \frac{2\sigma}{r} \tag{3.1}$$

where p is pressure, σ is surface tension, r is radius of the drop. The pressure difference between two differently sized droplets creates is given by the Laplace equation:

$$\Delta p = p_1 - p_2 = 2\,\sigma\,(\frac{1}{r_1} - \frac{1}{r_2}) \qquad (3.2)$$

When the droplets are connected with a micro-channel, the system tries to balance out the existing pressure difference between the droplets. This is achieved through the generation of liquid flow from the smaller to the bigger droplet. This flow is created internally and as a result no external force or pump is necessary. This makes the Laplace pump a convenient way of generating flow in microfluidic systems without increasing the size of the device.

In this section, grooved poly(2-hydroxyethylmethacrylate-*co*-ethylene dimethacrylate) (polyHEMA) surface were utilized for the formation of surface tension confined micro-channels. The grooved polyHEMA polymer surfaces were photografted with 2,2,3,3,3-pentafluoropropyl methacrylate (PFPMA) and the photomask was utilized to create a micro-channel with desired dimensions. As a result, superhydrophilic micro-channel was confined by the superhydrophobic borders. The generation of flow based on the Laplace pump principle in the prepared micro-channels was shown. It was found that the designed open microfluidic system is suitable for production of liquid flow in the micro-channels. The generation of the liquid flow in the micro-channels with different channel dimensions and geometries (S-shaped channel) was shown. Due to the small channel dimension and produced flow velocities, the generation of the laminar flow was observed. The dependence of the flow on the micro-channel dimensions was examined and studied.

3.2.2 Experimental details

Superhydrophilic-superhydrophobic patterns were prepared according to Chapter 2.4 by the photografting of grooved polyHEMA (HC composition) surfaces with PFPMA and using a photomask with desired pattern dimensions. The video of the flow in the micro-channel was taken by a high speed camera (Nikon Coolpix S8000). The flow velocity was measured by the following equation $v = d/t$, where d (cm) is the distance the rhodamine solution travelled and t (s) is time of travel.

3.2.3 Generation of liquid flow using passive Laplace pump principle

The micro-channels on the grooved polyHEMA surface were produced to test the passive Laplace pump principle (Figure 3.18). The solution of the rhodamine dye was utilized to visualize the flow in the channel. The patterns with linear and S-curved channels connected to 10 mm circle outlet were used for the visualization of liquid flow. It was observed that after addition of 5 µl of rhodamine solution to the end of the micro-channel, the flow was generated and the dye solution moved towards the bigger compartment. In this process, the 1000 µm wide channel was gradually dyed in red colour. After 10 seconds, rhodamine

solution formed concentration gradient in the whole micro-channel and the rhodamine solution reached the circular droplet. After 70 seconds the micro-channel and circular droplet were completely dyed.

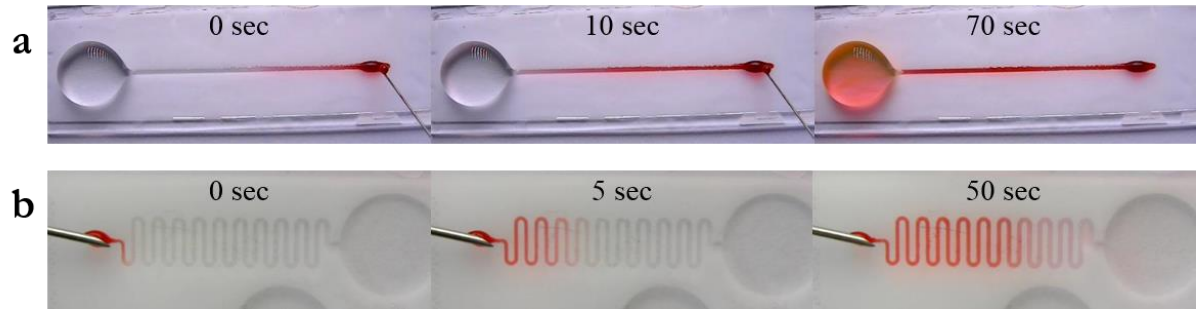

Figure 3.18: Images showing the flow of rhodamine solution (red) in the (a) 10 mm circle connected with 1000 μm wide channel pattern, (b) S-channel, consisting of 10 mm circle and 1000 μm wide channel.

The use of an S-curved instead of a linear channel lead to a similar formation of the liquid flow and resulted in gradual dying of the channel (Figure 3.18b). 5 seconds after the addition, the rhodamine solution travelled 40% of the whole path forming a clear concentration gradient. In comparison with the linear channel, on the S-curved micro-channel the concentration gradient is more visible, as the length of the path is larger. After 50 seconds, the rhodamine solution reached the circular droplet and in 90 seconds the droplet was completely dyed.

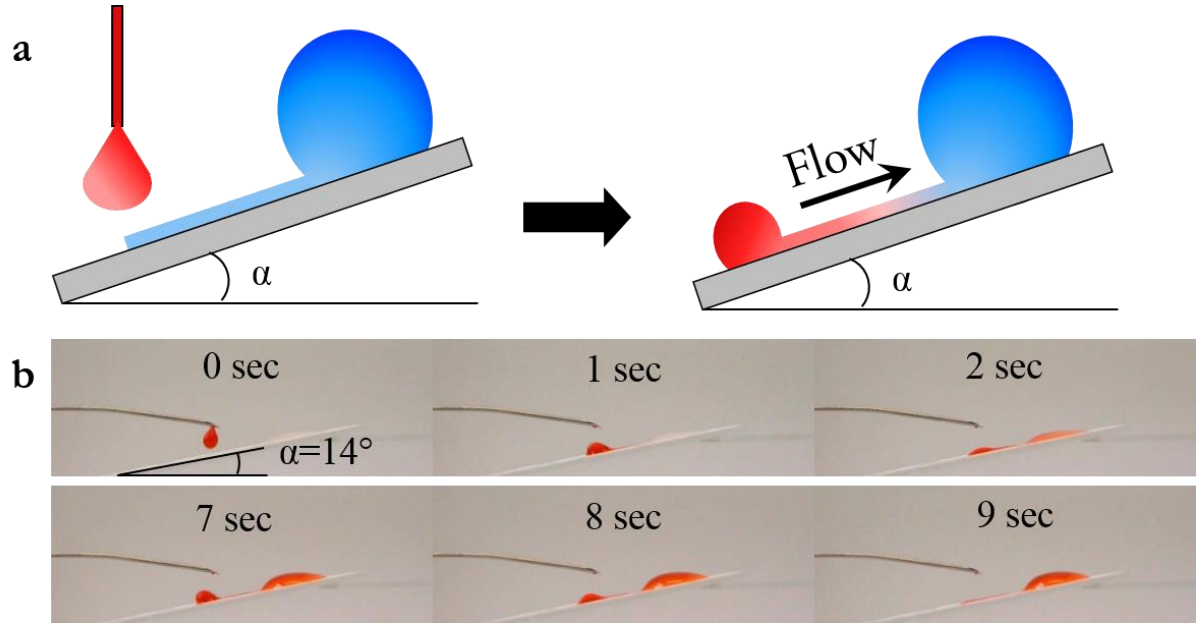

Figure 3.19: Images showing the upwards flow of rhodamine solution in the micro-channel with 10 mm circle outlet, tilt angle of ~14°.

The liquid flow in the micro-channel using the passive Laplace pump principle utilizes the pressure difference between the two droplets as the driving force of the flow. The upwards flow in the open micro-channel during the tilting is more complicated, due to the effect of gravity. The upward flow with 14° tilt was tested on the 1000 μm wide micro-channel (Figure 3.19). After one second of addition of the rhodamine solution, the dye moved upwards and in two seconds the circular droplet was dyed. In a similar way, the

second droplet was added and also after two seconds the added solution moved upwards. This proves the successful application of the passive Laplace principle in the superhydrophilic-superhydrophobic polyHEMA-PFPMA patterned microfluidic system as well as the possible application of the system for the creation of the chemical gradients.

The flow is laminar, when there is no disruption between the layers and no cross-currents perpendicular to the direction of flow. This flow regime is characterized by high momentum diffusion and low momentum convection. The Reynolds number, defined as ratio of inertial forces to viscous forces, is used for characterization of the flow regimes, such as laminar and turbulent flow [112]. For the laminar flow the Reynolds number is low, when the viscous forces are dominating. Laminar flow motion is smooth and constant. During the turbulent flow the inertial forces are dominating and thus the Reynolds number is high. Turbulent flow is distinguished by flow instabilities such as chaotic eddies, vortices etc. For the flow in the pipe, Reynolds number (Re) is given by the following equation:

$$Re = \frac{\rho v D_H}{\mu} \qquad (3.1)$$

where ρ is density of liquid, v is mean velocity of the liquid, μ is dynamic viscosity of the fluid, D_H is hydraulic diameter of the channel. The laminar flow is observed for Re<2300 and turbulent flow occurs when Re>4000. In the interval in-between the Re>2300 and Re<4000 the "transition" flows occur. While ρ and μ characterize the properties of the liquid flowing in the channel, v and D_H depend on the channel dimensions and established flow velocity. Thus, for creation of laminar flow the flow velocity and hydraulic diameter should be as low as possible to ensure low Reynolds number. In the microfluidic flow generated using passive the Laplace pump principle, the flow velocity is quite small (see Section 3.2.4). For the water solution in 500 μm wide channel connected to 10 mm circle outlet the highest observed flow velocity was around 0.3 m/s. The Reynolds number for the 500 μm micro-channel was estimated and was found to be around 115. This indicates that the developed micro-channel system might be suitable for generation of laminar flow. This statement was verified in the experimental setup using T-channels and solutions of water (transparent) and rhodamine (red).

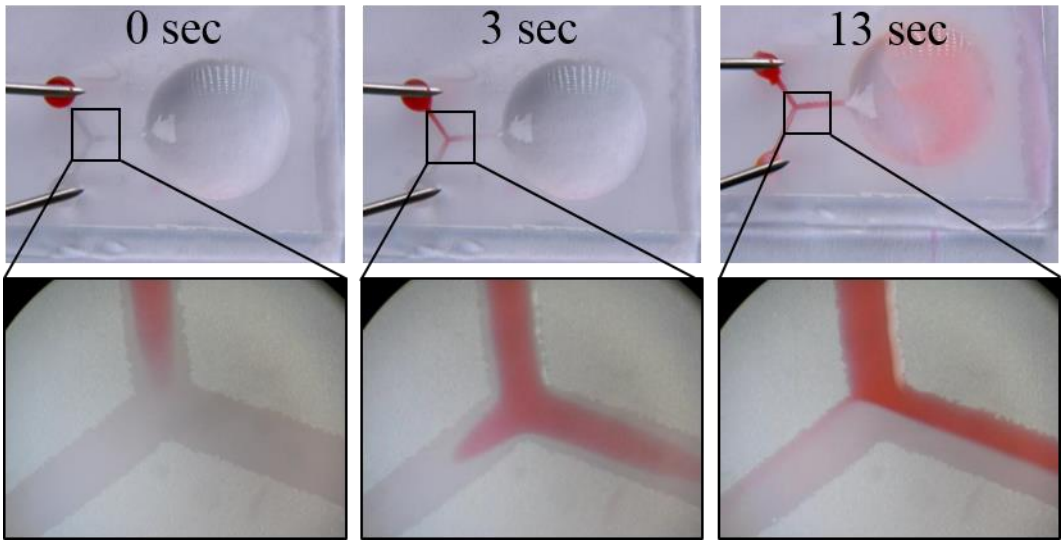

Figure 3.20: Images of the T-channel with 10 mm circular outlet the simultaneous addition of the rhodamine and water and creation of the laminar flow.

The T-shape 500 μm wide channel connected to 10 mm circle with two inlets was used for the simultaneous addition of two solutions and generation of laminar flow (Figure 3.20). If flow in the channel would be turbulent, the rhodamine solution would be chaotically distributed in the channel. However, it can be seen that after 13 seconds, water and rhodamine solutions are flowing in the parallel. There is distinctive straight line separating water and rhodamine solutions. The flow was stable, as long as the rate of the solution addition remained constant. If the rhodamine solution was added in higher rate than water (Figure 3.20 middle image), the laminar flow was not observed. Instead of flowing inside the middle channel connected with the outlet, the rhodamine solution partially flowed into water inlet. This shows that in the designed micro-channel system and by using the Laplace pump principle, the laminar flow in the channel was generated.

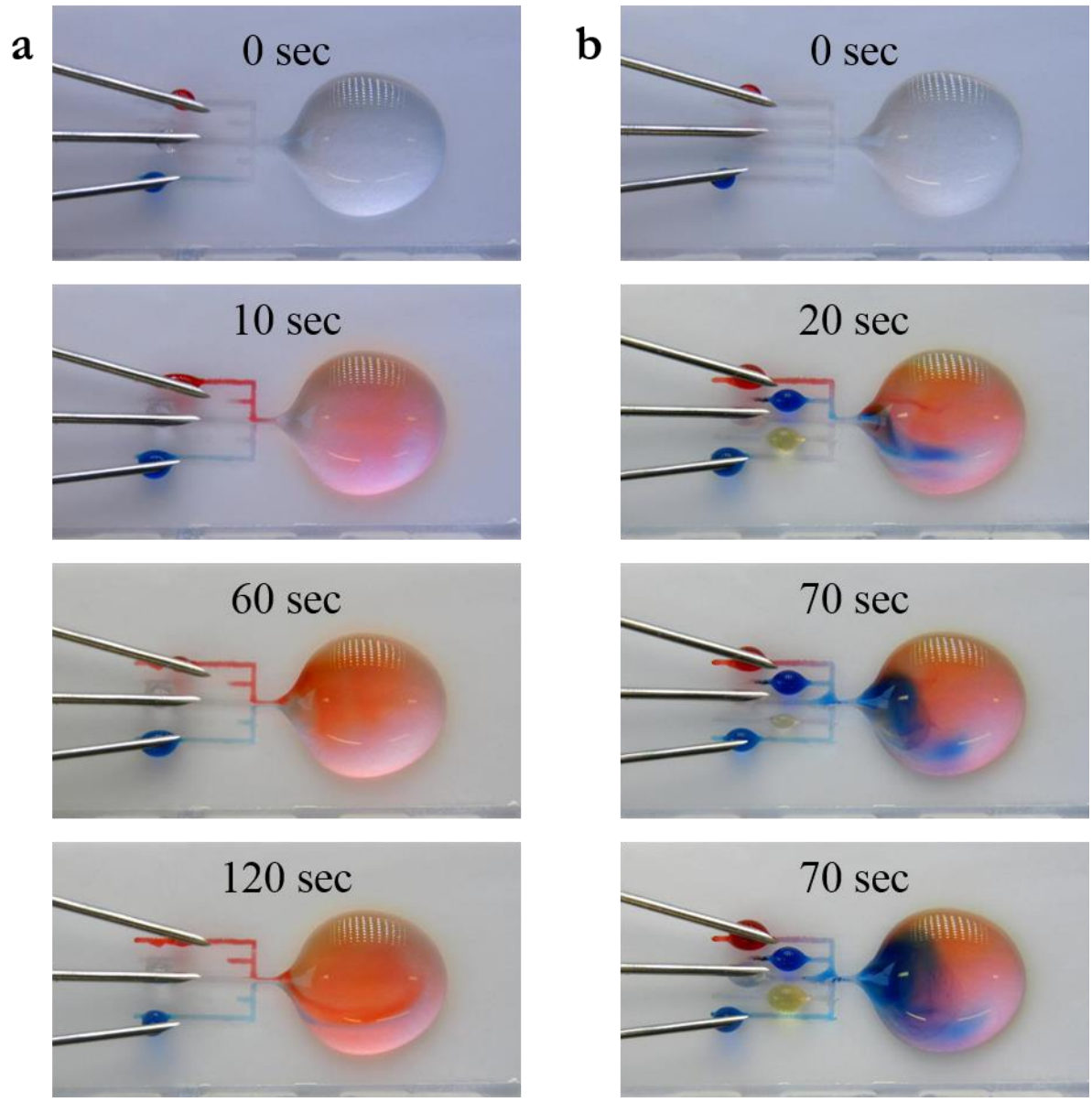

Figure 3.21: Images of the liquid flow in the micro-channels with 5 inlets and 10 cm circular outlet of (a) three and (b) five water dye solutions mixing.

Formation of not only simple but complex liquid patterns is a difficult task, however it is advantageous for numerous applications, for example in medical and biotechnological fields [113]. The micro-channel with multiple inlets connecting to the 10 mm circle was used for creation of the complex liquid patterns (Figure 3.21). Different dye solutions were added simultaneously to the inlets and the flow towards the outlet circle was started. In the outlet circle solutions mixed forming the liquid pattern. By varying the rate of the solution addition different liquid patterns in the circle could be formed. The amount of the solution mixed depends on the number of inlets present and the dyes added. It should be noted, that when three dye solution were added simultaneously at the different dye flow cross-section the solution did not mix instead forming laminar flow and after reaching the outlet circle the separate flow lines of red dye, water and blue dye, are still visible (Figure 3.21a). Similarly, the complex liquid patterns in the circle were obtained when five dye solutions were utilized. These results confirm generation of the laminar flow in the

microfluidic system even when more than two solutions were used. Additionally, the formation of complex liquid patterns in the outlet droplet by mixing three or five solutions was shown.

3.2.4 Influence of the channel dimensions on the liquid flow

The flow velocity in the micro-channel generated through the Laplace pump principle was measured by the analysis of the flow video. For this, rhodamine solution was utilized for easy detection of the flow inside the micro-channel (Figure 3.22).

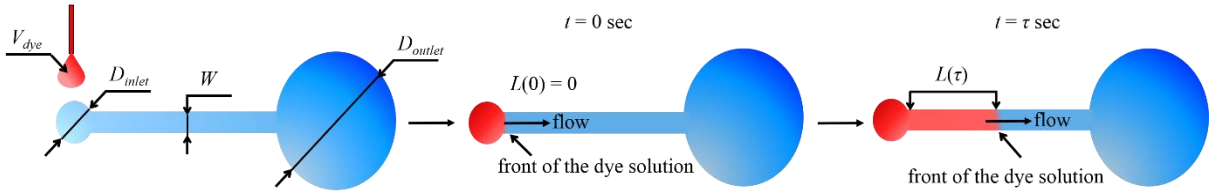

Figure 3.22: Schematic description of the experiment.

Rhodamine solution was added to the inlet droplet and the movement of the dye front from inlet to outlet droplet was observed. The influences of the volume of rhodamine solution added to the inlet droplet (from here volume of the dye, V_{dye}), size of the outlet hydrophilic region (D_{outlet}), and width of the channel (W) on the flow were studied. The high speed video recordings of the flow started from the addition of the rhodamine solution (t = 0 sec) and ended when the rhodamine solution reached the outlet circle. The time of rhodamine solution traveling through micro-channel was recorded. Flow velocity of the dye front (from here flow velocity) was calculated from obtained values of the time (τ) and distance travelled by the front of the rhodamine solution ($L(\tau)$).

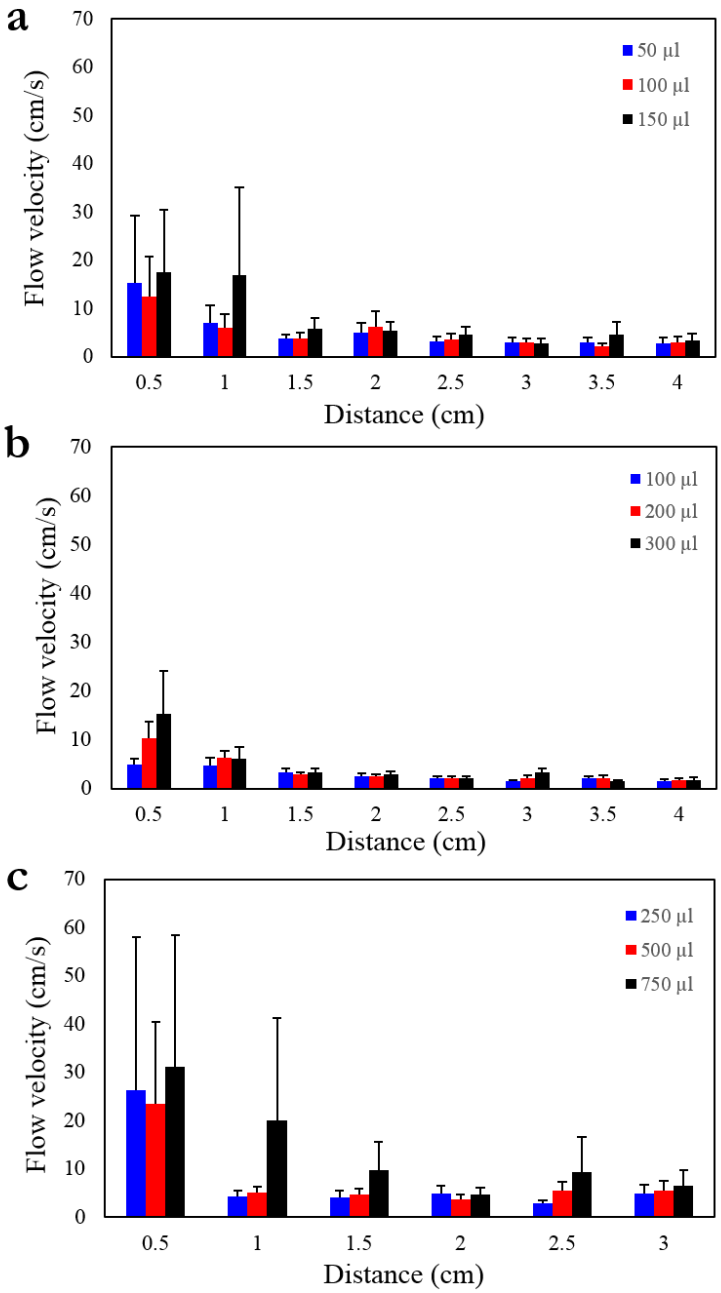

Figure 3.23: Graphs of the flow velocity of the dye front in the channels with 5 cm length, 1 mm width and diameter of the outlet patterned circle (D_{outlet}) of (a) 5 mm, (b) 10 mm, (c) 15 mm. Error bars are ± standard deviation.

The pressure difference between the outlet and inlet droplets depends on the diameter and hence the curvature of the corresponding droplets (Figure 3.23). To study the influence of the size of the outlet and inlet droplets on the flow velocity, a 5 cm long and 1 mm wide micro-channel was used. The highest flow velocity was observed in the beginning of the flow (0.5 cm from the inlet), independent of the outlet circle size. The flow velocity decreased with time (towards the end of the micro-channel), as the system balanced itself out. The observed decrease in the flow velocity with time can be explained by a gradual decrease of the pressure difference during the flow of liquid. During the flow, the radius of the hydrophilic region of the inlet droplet remains constant, while the volume of the droplet decreases. As a result, the

curvature and the Laplace pressure of the inlet droplet decreases, while the curvature and pressure of the outlet droplet increases. This causes a decrease in the pressure difference between the inlet and the outlet droplets. Therefore, the flow velocity in the channel is reduced with time.

It was found for all tested channels (with 5 mm, 10 mm, and 150 mm diameter of outlet circle) that flow velocity increased with the volume of the dye added to the inlet droplet. However, the difference in the flow velocity diminished with time (towards the end of the micro-channel). The graph (Figure 3.23) showed the potential influence of the radius of outlet circle on the generated pressure difference, which is the driving force of the flow in the channel. It was found that the change in the outlet circle diameter did not have a large effect on the flow velocity. Additionally, change of added volume of the dye had a limited effect on the flow velocity that was visible only for the biggest volume of the dye (Figure 3.23c).

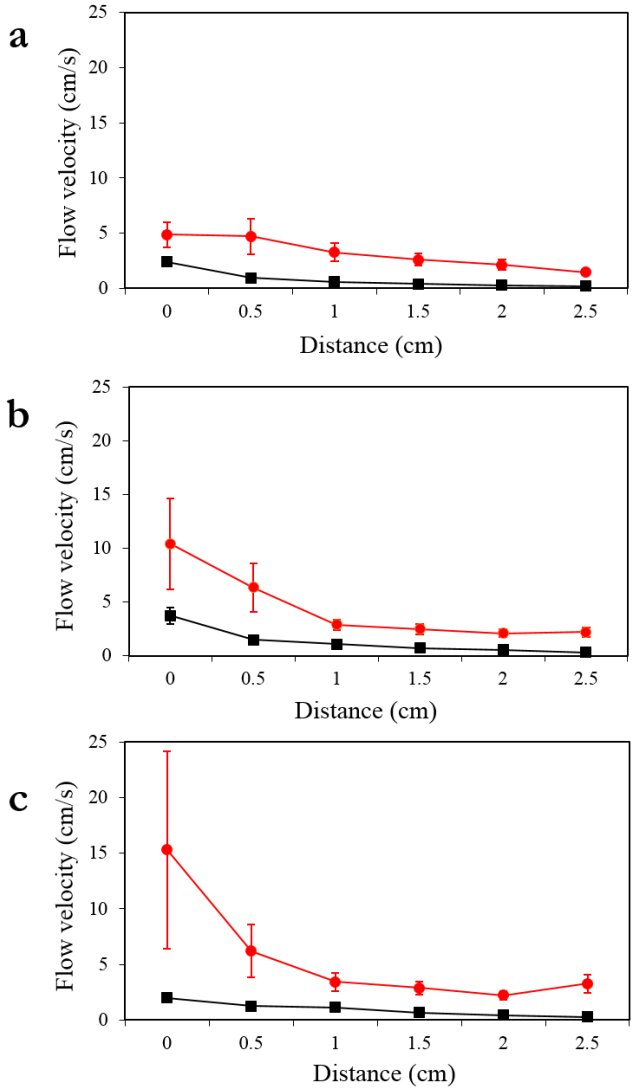

Figure 3.24: Graphs of the flow velocity of the dye for micro-channel with 10 mm outlet circle for 500 µm (black line) and 1000 µm (red line) channel width for different volumes of the added dye solution (a)100 µl, (b) 200 µl, (c) 300 µl. Error bars are ± Standard deviation.

The change of the channel width greatly affected the liquid flow. Two channels with different widths (500 and 1000 µm) were compared and the influence of volume of the dye on the flow velocity was

studied (Figure 3.24). Irrespectively of the channel width, the flow velocity of the dye front was faster at the beginning and decreased towards the end of the experiment time. It was found that the velocity was higher in the channel of the larger width for all tested volumes of the dye solution (100, 200, 300 µl)

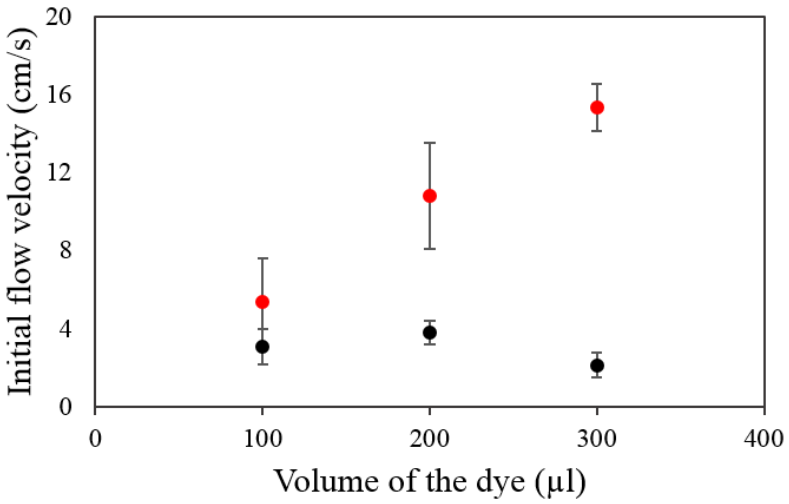

Figure 3.25: Initial flow velocity of the dye for micro-channel with 10 mm outlet circle for 500 µm (black line) and 1000 µm (red line) channel width. Error bars are ± Standard deviation.

The initial flow velocity (at t = 0 sec) differed greatly for the channels with different widths (Figure 3.25). For the small volume of the dye solution added to the inlet droplet (100 µl), the initial flow in the wider channel was about two times faster than in the narrow channel. When the volume of the dye in the inlet droplet was large (300 µl), the initial flow velocity in the wider channel was up to ~5 times faster than in the narrow channel.

3.2.5 Conclusions

Grooved polyHEMA surfaces were utilized for the formation of surface tension confined micro-channels. Polymer surfaces were photografted and a photomask was utilized to create hydrophilic micro-channel with desired dimensions. As a result, hydrophilic micro-channel, surrounded by the superhydrophobic borders, was formed. It was shown that the developed system could use the principle of the passive Laplace pump for flow generation. In this method, liquid flow is generated due to the pressure difference between the two channel ends. Utilization of this approach, allowed generation of flow inside the system, without any external pumps. It was found that even upward flow was possible. Formation of the laminar flow at the T-junction and complex liquid patterns in the multi-inlet system were also observed.

The effect of the channel dimension on the liquid flow was examined. The circle reservoir connected with the micro-channel was used as the experimental system. Reservoir diameter and the channel width were the primary parameters affecting the flow velocity. For all tested channels, the flow followed the similar

pattern: it was the fastest at the beginning of the experiment and then slowed down towards the end of the experiment. It was also shown that the volume of the dye solution had a strong influence on the flow.

It was shown that an open microfluidic system made using the superhydrophilic grooved polyHEMA channel surrounded by the photografted PFPMA grooved polyHEMA surface can create a passive Laplace pump. The system flow can be controlled by the channel dimensions. Also the laminar flow and formation of complex liquid patterns are easily achieved.

3.3 Cell behavior on the rough surfaces

3.3.1 Background

The interactions between cells and surfaces attracted great interest in the past decade, due to the emerging need to understand how surface properties modulate cell fate and later use this knowledge to control cell behaviour in artificial systems. It was shown that cell adhesion and proliferation depend on the wetting properties [114], stiffness [115], [116], and roughness [117] of the substrate.

Cells utilize filopodia, which are fine, integrin-containing cell membrane projections, to probe the surface. Integrins are cell receptors that orchestrate cellular adhesion to adjacent surfaces [118]. These receptors are transmembrane proteins consisting of α- and β- subunits [119]. Upon contact with a surface, integrins form clusters known as focal adhesions. Cell-surface communication is achieved through extracellular receptor domain binding to the ligand containing proteins, absorbed on the surface (e.g. fibrinogen, fibronectin, vitronectin).

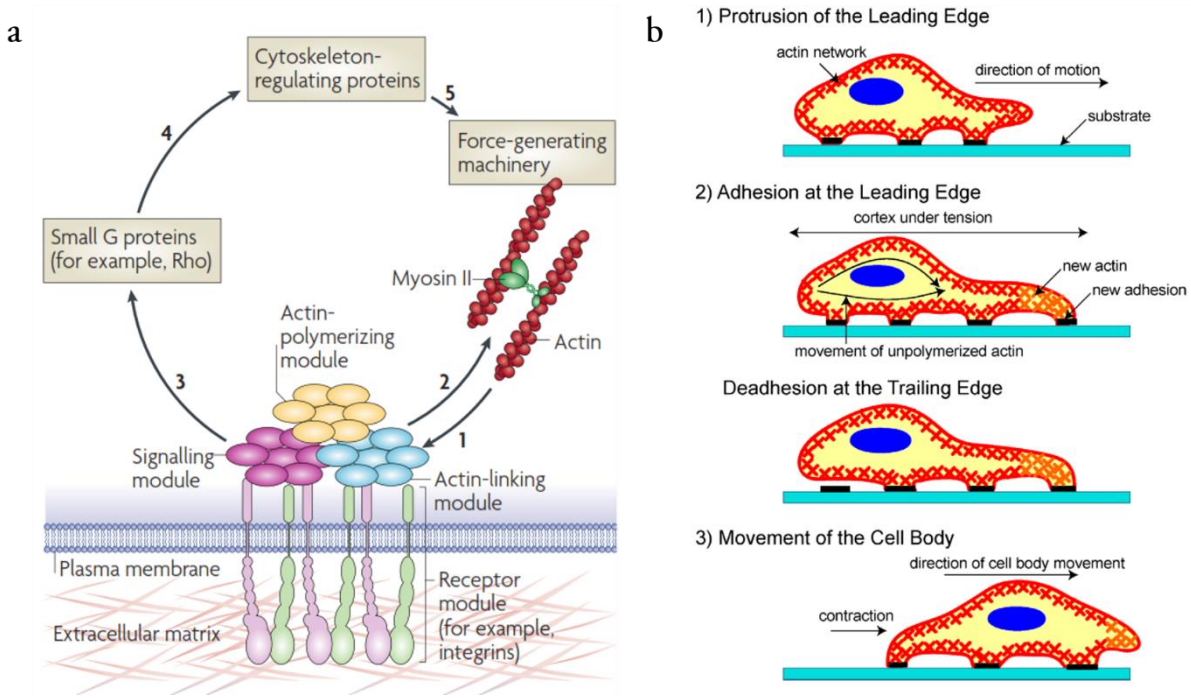

Figure 3.26: (a) Actin cytoskeleton-focal adhesion feedback loop. Reprinted from [120] with Nature Publishing Group permission, Copyright 2009. (b) Schematic description of cell movement. Reprinted from [121] with IJBS permission, Copyright 2007.

The spacing between the binding sites of individual integrins is in the range of 50-70 nm and is required for normal integrin signaling and adhesion [122]. Integrin-ligand binding leads to the contraction of the cytoskeleton through complicated signaling networks [123]. The inner-cell part of the integrin plays

a role in the activation of the phosphorylation- and G-protein-mediated pathways (Figure 3.26). Actin polymerization and myosin II-dependent contractility create forces that affect specific proteins in actin-linking modules (i.e talin and vinculin), receptor modules and co-receptors. Through integrin-mediated signaling pathways, cell-surface adhesion plays an important role in the control of other inner processes such as cell proliferation, differentiation, and migration [124].

Cell motility is a complex process induced by the cell's response to an external signal in its environment [121]. The cell cytoskeleton, composed of actin, microtubules and intermediate filaments, is the primary driving force in the cell movement process. Cell movement begins with protrusion of the leading edge forward by orienting and reorganizing the actin network. Polymerization of actin filaments towards the cell membrane generates a polymerization force and leads to the cell propelling the membrane towards the direction of the movement [125]. Afterwards, the cell adheres to the surface at the leading edge and releases at the rear of the cell. The focal adhesion in the rear disassembles due to the generated cytoskeletal contractile forces [126]. If the detachment process is not possible, adhesion sites prevent the cell from moving forward. In the final step, the cell body and rear of the cells are displaced. The acto-myosin network generates the required retraction force and since the actin filaments are connected to the cell membrane, the retraction force can enable the cell movement forward [127].

Self-renewal and pluripotency are unique stem cell properties that offer new prospects in medicine and biotechnology applications. Stem cells have great importance for the treatment of diabetes, Alzheimer and Parkinson's diseases, drug screenings and for stem-cell therapy. Embryonic stem cells are derived from the inner mass of the blastocyst, during early embryo development. Through the process of differentiation, embryonic stem cells give rise to all somatic cell types in the embryo. Stem cell differentiation is a complex process which depends on both physical [128]–[130] and chemical [131], [132] cues. For successful use of the advantages of stem cells it is important to be able to expand their population in artificial culture systems. Expanding stem cells in culture requires maintaining their self-renewal and differentiation capacity. Up till now the feeder system, where stem cells are cultured on a layer of mouse embryonic fibroblast cells (MEF), is the most widely used system in laboratory. The role of the feeder cells lies in the providing necessary chemicals for pluripotency stem cells. For example, leukemia inhibitory factor (LIF) was identified as one of the feeder cell derived molecules that plays a crucial role in the maintaining of stem cell pluripotency. However, challenges in expansion of undifferentiated stem cells for clinical applications include the removal of feeder layers and non-defined components in the culture medium [133]. Therefore, artificial systems that promote stem cell expansion while maintain stem cell pluripotency, without use of the feeder cells, are of great interest. Embryonic stem cells grow in tightly packed colonies with defined borders. However, as the cells start to differentiate, the cell colony starts to spread and the shape of individual cells change from spherical (not adhered or weakly adhered) to a spread out shape (adhered). Undifferentiated stem cells can be identified by elevated levels of alkaline phosphatase on their cell membrane (alkaline phosphatase staining), or by the expression of stem cell markers such as Oct3/4, Nanog, SSEA-4, and SSEA-3.

In this section, polyHEMA surfaces with different surface roughness were used for maintenance of stem cell pluripotency. PolyHEMA surfaces with micro and nano-roughness, as well as smooth

polyHEMA surfaces, were utilized. Firstly, cancer cell motility on the surface was examined using cross-contamination study and time-lapse analysis. Secondly, stem cells were cultured on the surfaces with varying surface roughness for four passages. The Alkaline Phosphatase (AP) assay and Western blot analysis were performed for the analysis of stem cell pluripotency. Additionally, microrough grooved polyHEMA surfaces were modified with amine and decane thiol groups to study the influence of chemistry on stem cell differentiation.

3.3.2 Experimental details

Cancer cell lines (red fluorescent rat mammary carcinoma MTLy-mCherry and human cervical tumor cell line HeLa expressing GFP) and mouse embryonic stem cell lines (D3) were cultured as described in Section 2.9.1 and 2.10.1, respectively. PolyHEMA surfaces with different surface roughness were prepared according to Section 2.3.1 for the micro-rough grooved surface, Section 2.3.2 for the smooth surface and Section 2.3.3 for the nano-rough surface. The micro-rough surface with composition HC was chosen as representative sample, due to its high transparency, needed for microscopy. For the preparation of the micro-rough surface, the mold consisted of two modified glass plates. The bottom glass plates with grooved morphology were used for further studies. For nano-rough and smooth surfaces, the polymerization mold consisted of modified (top plate) and fluorinated (bottom) glass plates. The chemical composition of all surfaces was kept the same by keeping the ratio of monomer (HEMA) to cross-linker (EDMA) constant. Surface morphology was examined by SEM measurement as described in Section 2.5. Surface roughness for all surfaces was measured by a confocal optical profiler according to Section 2.7. The 1 x 3 cm rectangular patterns were prepared for the cross-contamination study according to Section 2.3.1

3.3.3 Surface properties of the polyHEMA surfaces with different roughness

Three polyHEMA surfaces with different surface morphology and roughness (micro-rough, nano-rough, and smooth) were prepared. The surface morphology of the polyHEMA surfaces was compared by SEM (Appendix Figure 5.1). Although chemical composition of the surfaces was kept the same, surface morphology of the polymer surfaces differed greatly.

The surface roughness of the polyHEMA surfaces was measured by a confocal optical profiler and the average surface roughness (Sa) was calculated. The surface roughness results and topography maps closely correlated with the SEM results. Topography maps of the tested surfaces indicated that indeed the surface roughness was different for all the samples (Figure 3.27). Average surface roughness was the highest for microrough surface (with Sa=919±22 nm). As was found by the SEM, microrough surface was comprised of agglomerates of polymer globules inhomogeneously distributed on the relatively flat substrate. As a result, the thickness of the polymer film greatly varied, which contributed to high surface roughness.

The nano-rough protruded polyHEMA surfaces displayed Sa=68±30 nm. The highly porous structure of the nano-rough surface coupled with small globule size resulted in lower surface roughness compared to the microrough surface. Smooth polyHEMA surfaces showed Sa of ~2 nm.

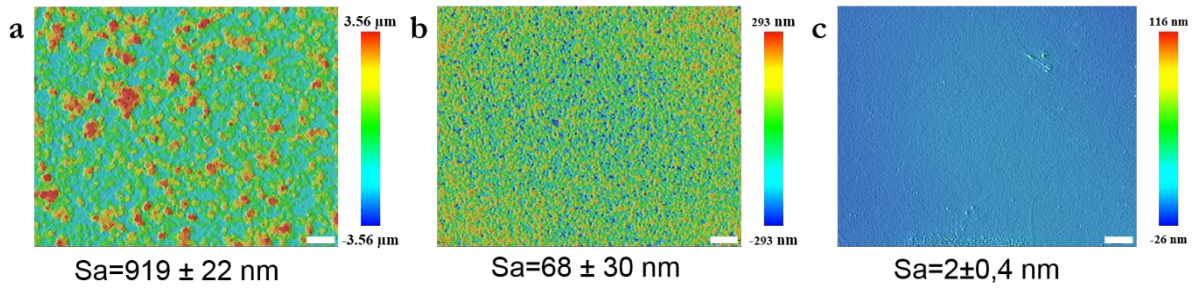

Figure 3.27: Topograpy maps of polyHEMA (a) micro-rough, (b) nano-rough, and (c) smooth surfaces. Scale bars 20 µm.

PolyHEMA surfaces with different surface roughness, but the same chemical composition, were prepared. The difference in the surface morphology and roughness of the polymer surfaces was confirmed by the SEM and surface topography measurements. Thus, these surfaces are suitable for the investigation of the influence of the surface roughness on cell behaviour. It should be noted that due to the roughness influence, all surfaces also possess different wettability and transparency.

3.3.4 Cell motility assessment on the micro-rough grooved polyHEMA surface

Maintaining cell populations in close proximity without cross-contamination is an important tool for studying and mimicking various natural processes. Nano-rough polyHEMA surfaces were used before to evaluate cell cross-contamination and cell-communication [91]. Two types of cells (MTLy-mCherry and HeLa-EGFP) were co-cultured in adjacent nano-rough compartments. Cells, dispensed into hydrophilic spots, were confined by the hydrophobic border. However, as the cells proliferated and migrated, the cross-contamination of the cells between the spots increased with time. It was found that after 72h of co-culturing, cross-contamination of the cells in the nano-rough pattern was 1.5%.

Similarly, micro-rough patterns were made and the MTLy-mCherry and HeLa-EGFP cells were cultured in adjacent rectangles for up to 3 days (Figure 3.28). In comparison with previously published results, the cross-contamination on the micro-rough polyHEMA pattern after 72h was extremely low. It was found, that after 24h, the vast majority of the cells stayed in the original adhesion spot, in the center of the rectangle. As a result, there were no cells on the superhydrophobic border and the surrounding space in its proximity was also void of any cells. After 48h, as the HeLa-EGFP cell number increased, they started to move towards the other compartment and the amount of cross-contamination increased. After 72h, the cross-contamination of cells was below 0.2%.

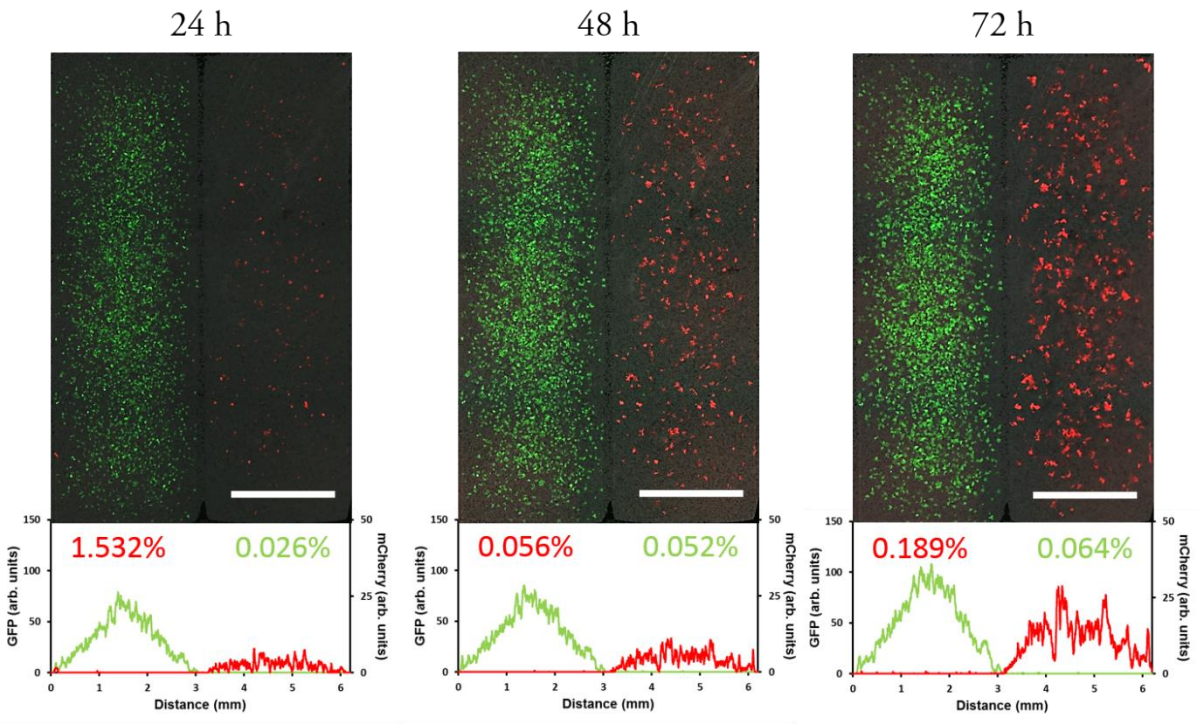

Figure 3.28: The fluorescence microscopy images and their respective quantification (below) of cross-contamination between MTLy-mCherry and HeLa-EGFP cells cultured in adjacent rectangles for 3 days. Scale bars are 2 mm.

It was observed that the cell cross-contamination was lower on the micro-rough surfaces than on the nano-rough surfaces. As the experimental conditions were identical, the the observed result may be explained by the combined effect of reductions of both cell proliferation and cell motility. Indeed, it was observed that cell proliferation on the micro-rough patterns was retarded compared to that on the nano-rough patterns and this may in turn affect the number of migrating cells. However, it should be noted, that the cells close to the superhydrophobic border stayed in the original position through all 72h (Figure 3.29).

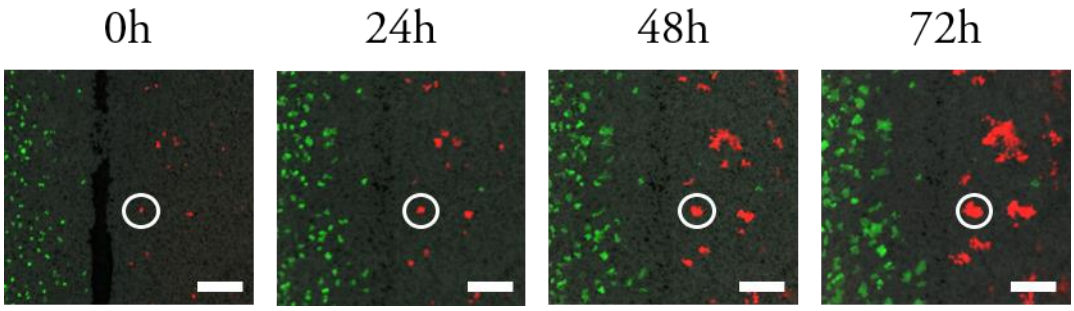

Figure 3.29: Time-lapse images of HeLa-EGFP cell colonies on a micro-rough polyHEMA surfaces in the vicinity of superhydrophobic border. Scale bars 1 mm.

The observation of individual cell colonies in the hydrophobic border vicinity, showed an increase of the colony fluorescence intensity and hence cell number. However, there was no change in the colony position and during this time the colony remained tightly packed. Thus, it can be concluded that the main reason for the low cell cross-contamination observed on the micro-rough patterns was low cell motility. To

prove this, cell motility of the HeLa-EGFP cells was measured by time-lapse fluorescence microscopy. The cells were continuously monitored for 24h and their movement trajectories were plotted (Figure 3.30).

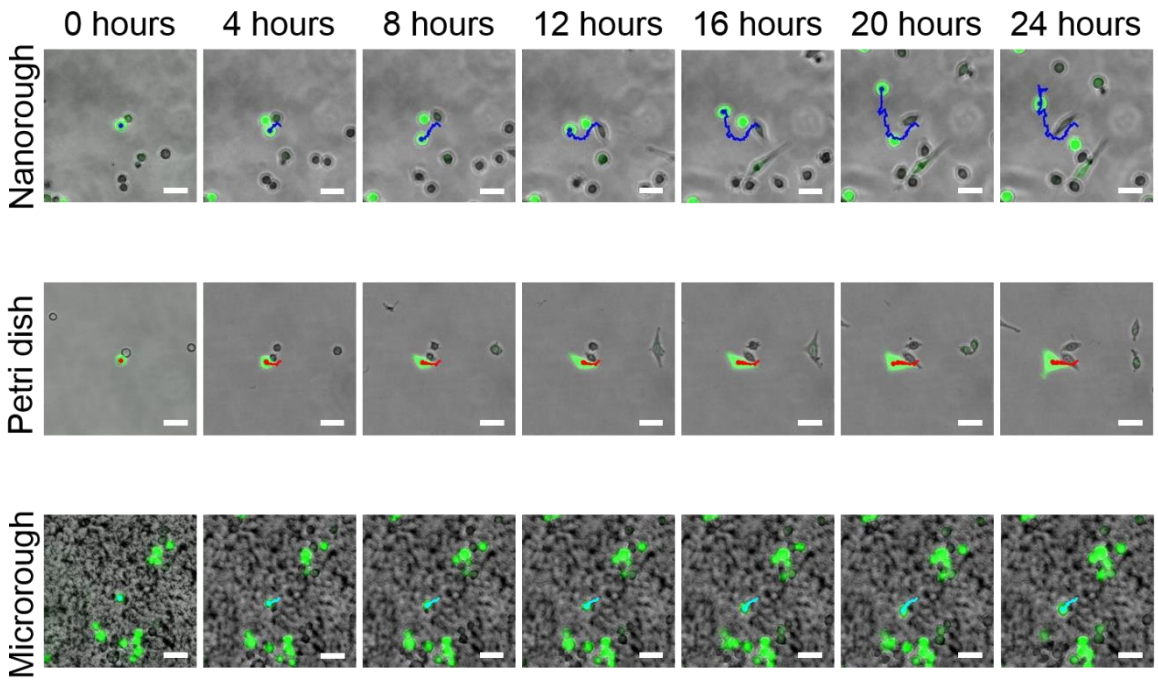

Figure 3.30: Time-lapse images of HeLa-EGFP cells on the micro-rough, and nano-rough polyHEMA surfaces and on a Petri dish for 24h. Scale bars 50 μm.

For the comparison of cell motility, a Petri dish (polystyrene) sample was used as a control, since it is widely used for cell culture. It was found that on the nano-rough surface, the cells had the highest motility. The cell shape changed from rounded to spread out when the cell proliferated and moved. On the Petri dish, cells did not move as much as on the nano-rough surface. The cells on the micro-rough surface almost did not move from the initial position, staying close to the initial point as where they were seeded. The cell shape was close to round through the whole observation time. To compare the cell motility, the quantification of cell speed (S), translocation (T), displacement (D) and length of the path (L) was performed for 10 cells (Figure 3.31).

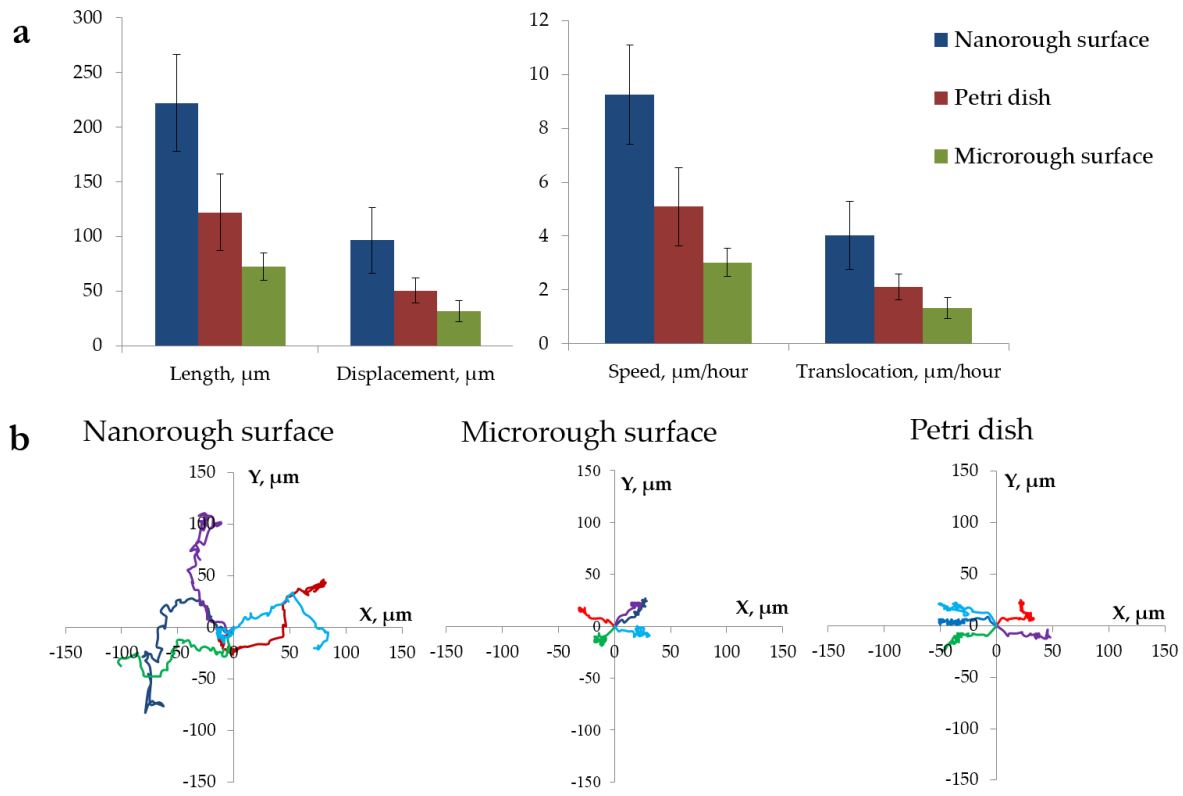

Figure 3.31: (a) Comparison of the path length (L), displacement (D), speed (S=L/t) and translocation (T=D/t) of the cells (HeLa-EGFP) cultured on the nano-rough, micro-rough and Petri dish surfaces. (b) Five examples of the travelled cell paths (HeLa-EGFP) on the nano-rough, micro-rough and Petri dish surfaces. The values are calculated for 10 cells. Error bars are ± standard deviation.

The cell displacement (D) was defined as the length of the line between the starting and ending points of cell movement, whereas length (L) is the total length of the path that the cell travelled. Cell speed (S) was defined as $S = L/t$ and cell translocation as $T = D/t$. The trajectories of 10 cells on all surfaces were analyzed and the trajectories of 5 of them are shown. Cells on the nano-rough surface showed the highest motility with 220 µm travelled at the speed of 9 µm/hour. Cells on the Petri dish travelled only half of that distance (120 µm) and cells on the rough surface only a third (72 µm). Not only did the cells travel longer distances, the travelled path of the cells on the nano-rough surface was more complex. The possible explanation of the observed high cell motility on the nano-rough surfaces versus low cell motility on the micro-rough surfaces, is the retardation of the cell movement process. Cell movement consists of three steps: protrusion of the leading edge, adhesion of the leading edge and de-adhesion of the rear end, contraction and movement of the cell body [121]. From the obtained evidence, it can be concluded that the surface micro-roughness inhibits at least one of the cell movement steps. From time-lapse images, it can be seen that the cells form protrusions (Appendix Figure 5.2). Thus, the reason might lay in inhibition of the trailing edge during de-adhesion. It is well known that cell-surface adhesions, and specifically integrin-ligand binding, regulate cell motility [134]. Previously, it was also shown that cells can form protrusions into the surface pores, making cell detachment more difficult [135]. Therefore, it can be concluded that strong interaction of the cell protrusions with the micro-rough surface might prevent cells from easily detaching.

As a consequence, cells are pinned to the spot and unable to move. Additionally, it was observed that on the micro-rough surface cells did not show any signs of spreading during the whole time of observation. This might indicate that the cell spreading process is also inhibited [136]. After the establishment of initial cell-surface adhesion, increased actin polymerization on the cell periphery results in an increase of the cell area [137]. During this intermediate phase of cell spreading, recycling of the adhesion receptors takes place. As new adhesion sites are formed on the cell periphery, mature adhesion sites located towards the center of cell are disassembled [138]. It can be therefore be concluded that a difficulty in the disassembly of formed cellular contacts might prevent cell spreading and movement on the micro-rough surface. In contrast, on the nano-rough surface cells were able to spread and move freely, indicating that formation and disassembly of the adhesion sites takes place.

Mathematical models of cell movement are usually based on random motion models [139]. Uncorrelated random motion signifies that the direction of an object's movement is completely independent of the object's previous movements. The movement can be measured by the mean squared displacement $< \delta(\tau)^2 >$, which is given by the following equation:

$$\delta(\tau) = r(t+\tau) - r(\tau) \qquad (3.2)$$

where τ is time interval between two positions $r(t+\tau)$ and $r(\tau)$. For random motion, $< \delta(\tau)^2 >$ satisfies the following equation:

$$< \delta(\tau)^2 > = 2nD\tau \qquad (3.3)$$

with n is the dimension of the space of the movement and D is the diffusion coefficient. However, cell movement is in fact not random, as each movement is dependent on the history of the previously taken steps [140].Correlated random walk is described by the Fürth equation:

$$< \delta(\tau)^2 > = 2nD(\tau - P(1 - e^{-\tau/P})) \qquad (3.1)$$

where P is the persistence time and is a measure of the time for which a given velocity is remembered. Persistent random motion is widely used as a mathematical model for eukaryotic cells movement [141], [142]. However, while this model provides some insights into cell movement it does not take into account the cell movement process and should therefore be used with caution.

The mean squared displacement $< \delta(\tau)^2 >$ was calculated for the cell movement on the nano-rough, micro-rough and Petri dish surfaces (Figure 3.32).

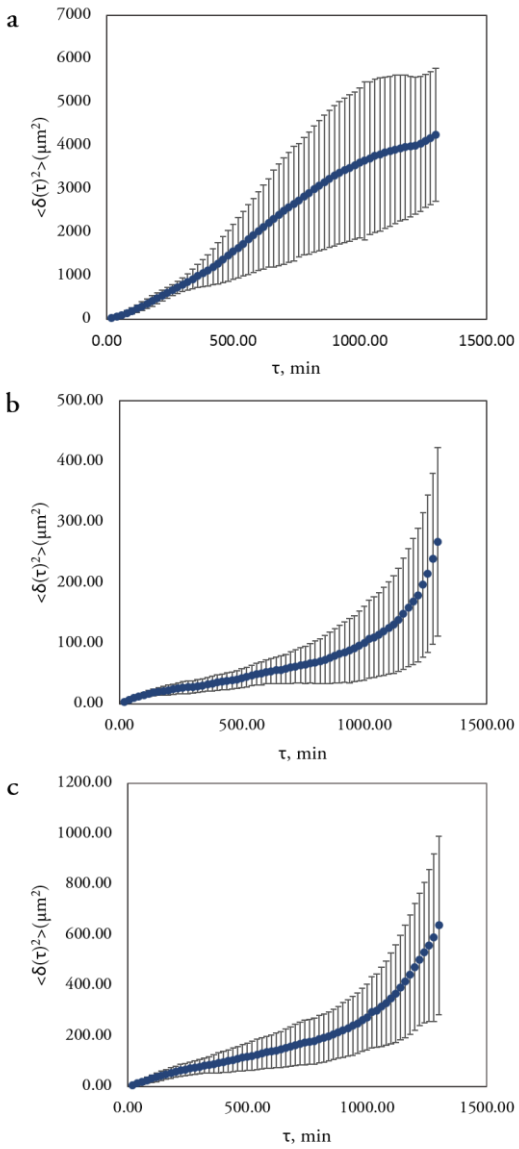

Figure 3.32: Mean squared displacement $< \delta(\tau)^2 >$ vs. time interval τ for cells on (a) nano-rough and (b) micro-rough polyHEMA surfaces and on (c) a Petri dish surface for 24 hours. Error bars are ± standard deviation.

From the obtained results, it can be concluded that for all the tested surfaces the cell motility did not follow the random walk or persistent random walk model. In contrast, the mean square velocity can be fitted quite well by an exponential equation. In agreement with previously published results, these findings show that the motility data of adherent cells cultured in vitro follows an exponential distribution [143], [144]. It was found that the mean squared displacement of the cell movement on the nano-rough surface differed greatly from that on the micro-rough polyHEMA surface as well as the Petri dish surface. The mean squared displacement of the cells on the Petri dish was higher than that on the micro-rough surface. However, the mean squared displacement dependency for the Petri dish and micro-rough surface was the same. Since the cell environment was the same during the culturing for all surfaces, the effect of cell density and other factors on the cell movement is not relevant to the observed effects. However, as the cells were cultured on the surfaces for 24 hours, it is possible that the cell movement in the initial stage of culture would be different

than in the later stages of culturing. In the initial culture stage, the cells come into contact with the surface and form primary adhesion sites. During the middle or later stage, as the cell moves around it can come into close contact with other cells or divide. These factors can influence cell behaviour and consequently cell movement. To answer if the cell movement was different for initial and later stages, the mean squared displacement at different time intervals were analyzed.

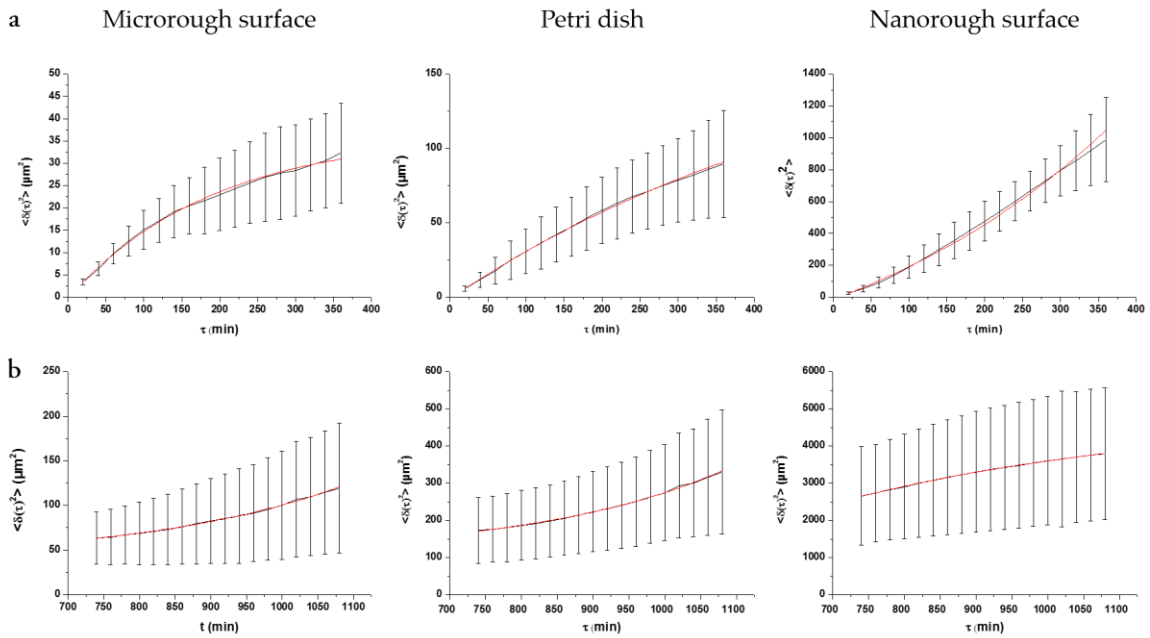

Figure 3.33: Mean squared displacement $< \delta(\tau)^2 >$ vs. time interval τ for nano-rough and micro-rough polyHEMA surfaces and a Petri dish surface for the (a) 0 to 6 hours' time interval, (b) 12 to 18.2 hours' time interval. Red line corresponds to the exponential fit of the data. Error bars are ± standard deviation.

It was found, that the biggest differences in the mean squared displacement between the nano-rough and micro-rough/Petri dish surfaces were in the initial (0-6 hours) and intermediate (12-18 hours) cell movement stages (Figure 3.33). In the first 6 hours of observation, the mean squared displacement for the Petri dish and micro-rough surfaces followed a decaying exponential dependence. This might be related to the retarded cell motility, due to the adaptation of the cells to new environment. In contrast, in this time period the cells on the nano-rough surface showed a growing exponential dependence. The inversed tendency was found in the intermediate stages of cell movement (Figure 3.31a). This indicates that on the nano-rough surface, cell movement follows a different pattern than on the micro-rough and Petri dish surfaces. The possible explanation of this is that cells on the nano-rough surface do not require the adaptation period in the initial stages or that this period is faster than on the other two surfaces. The difference in the intermediate stage of cell culturing might be caused by the start of the cell division, leading to the inhibition of cell movement.

3.3.5 Maintenance of stem cell pluripotency

This part of the work was done in collaboration with Dr. Ping Zhang (Christina Blattner group, ITG, KIT).

Cell adhesion plays an important role in stem cell differentiation [118]. In particular, it was shown for mesenchymal stem cells (MSC) that reduction in adhesion is necessary for the maintenance of MSC multipotency [128], [145]. Cell adhesion should be reduced, while still allowing cell proliferation. These conditions resemble the natural stem cell niche, where the stem cells exhibit slow proliferation and are quiescent [146], [147]. As shown previously, a cancer cell line on the micro-rough surface showed reduced cell motility due to the strong interaction between the cells and the surface. Therefore, micro-rough surfaces might be able to delay stem cell differentiation by retarding cell adhesion and cell motility. To investigate this effect, polyHEMA surfaces with different roughness were utilized. PolyHEMA surfaces were prepared as described in Section 2.3 and were characterized using SEM and a confocal optical profiler as was mentioned earlier in Section 3.3.3.

Mouse embryonic stem cells (mES) were cultured on the micro-rough, nano-rough, and smooth polyHEMA surfaces. Petri dish and gelatin surfaces were used as the controls. Strong adhesion of the feeder cells to the gelatin is widely used as the routine method for feeder cell removal. This technique was utilized with the cells prior to their seeding (p1 cells). For all the passages, the same cell number was seeded on all surfaces (1 million cells). Afterwards, cells were cultured for 4 passages and each passage consisted of 4-5 days. After each passage, the cells were collected and their total number was calculated (Figure 3.34).

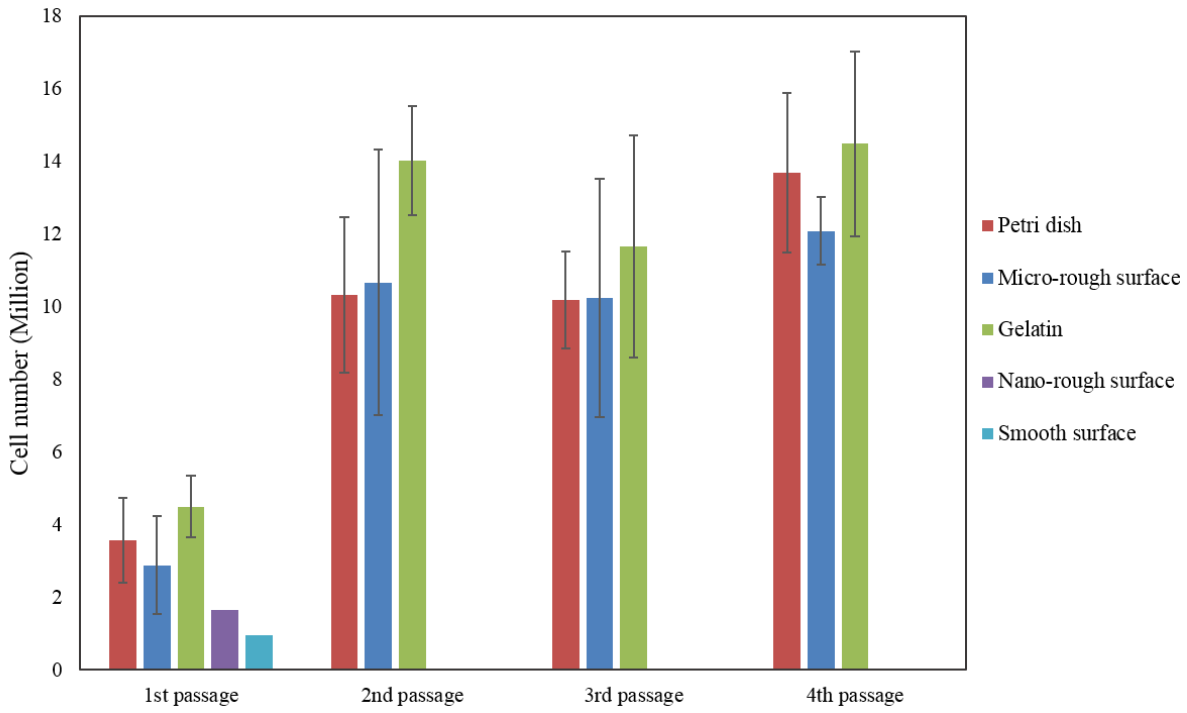

Figure 3.34: Total mES cell number after each passage during 4 passages on micro-rough, nano-rough and smooth polyHEMA surfaces, as well as on the Gelatin and Petri dish surfaces. Red line corresponds to the seeded cell number. Error bars are ± standard deviation.

The cell proliferation cycle can be influenced by cell-surface adhesions, which in turn can be controlled by the surface properties [148], [149]. For practical application of artificial cell culture systems, cell adhesion and cell proliferation are important cell behavior characteristics to understand. mES cells adhered poorly to the nano-rough and smooth polyHEMA surfaces, which resulted in extremely low cell count after just 1 passage. The cells did not adhere well to the smooth surface and were easily removed by the washing step. After four days in culture, the cell number on the smooth surface was 0.95 million (lower than what was seeded). On the nano-rough surfaces, the cells did form some colonies, however in comparison with the other surfaces (micro-rough, gelatin, and Petri dish), the cell number after 4 days in culture was significantly lower (1.7 million cells). Hence, nano-rough and smooth surfaces were found not to be suitable for long term stem cell culturing. Conversely, after passaging mES on the micro-rough surface, gelatin and Petri dish, the cell number significantly increased. It was found that after each passage the cell number on the gelatin covered surfaces was a bit higher than on the Petri dish or micro-rough surface, indicating that proliferation may be slightly retarded on these surfaces. After fourth passage, the cell numbers for the gelatin, Petri dish, and micro-rough surface were 14.5, 13.7, 12.1 million cells, respectively. However the difference was not significant, and therefore micro-rough surfaces were found to be suitable for the long-term stem cell culture.

Alkaline phosphatase (AP) staining is a simple tool for detecting pluripotent stem cells. Pluripotent stem cells show elevated levels of alkaline phosphatase in the cell membrane and are stained violet, while differentiated cells are transparent. mES cells cultured on gelatin, Petri dish and polyHEMA surfaces with different surface roughness were stained with AP staining after each passage. The AP staining of the mES

cells cultured on the nano-rough and smooth surfaces showed low amounts of stem cell colonies (Figure 3.35). It should be noted however, that the stem cells that were seeded on the surfaces might have contained feeder cells, as it is difficult to completely remove the feeder cells. On the nano-rough surface there were some stem cell colonies, however, they had no distinctive borders indicating that the cells in the colony periphery started to differentiate. In between the colonies lay large amounts of differentiated cells. The differentiated cells possessed an elongated cell shape and were found mostly either as individual cells or in small cell groups. The stem cell colonies and differentiated cells were sparse on the smooth surface.

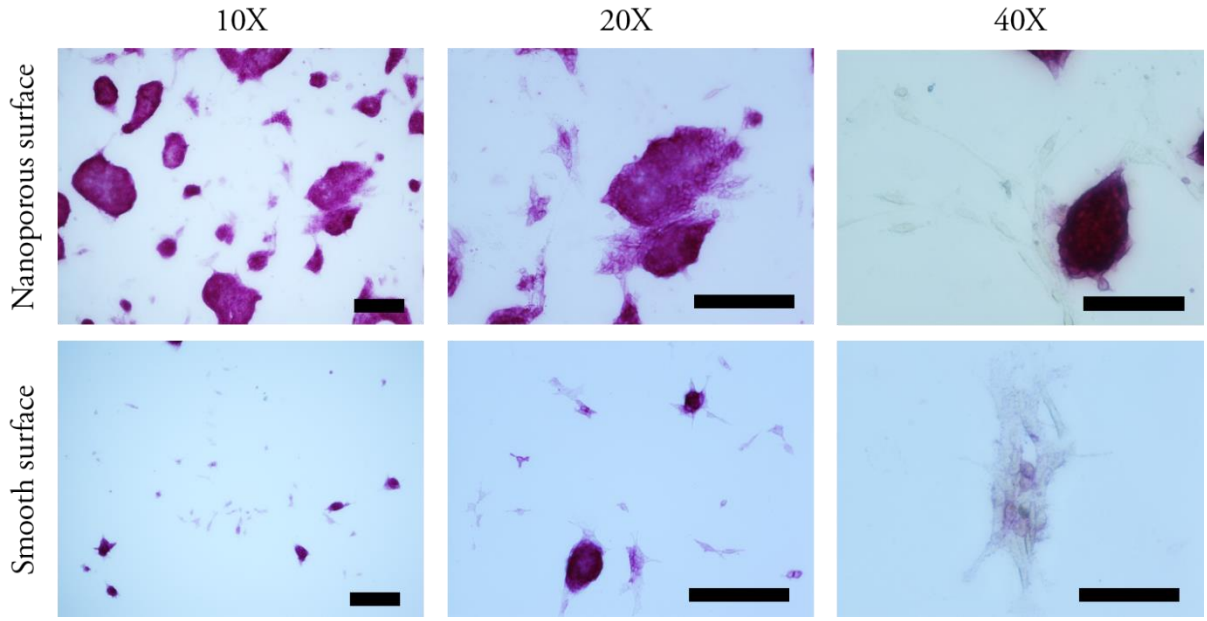

Figure 3.35: Alkaline phosphatase staining of the mES cell after 4 passages cultured on the nano-rough and smooth polyHEMA surfaces. Pluripotent cells were stained violet, while differentiated cells were transparent. Scale bars in 10X, 20X images are 200 μm, in 40X images- 100 μm.

The result of the AP staining on the smooth and nano-rough surfaces can be related to the observed low stem cell adhesion during seeding and partial removal of the stem cells after washing. The stem cell colonies were relatively small and had some differentiated cells on its edges. The differentiated cells were spread out and had an elongated cell shape. This shows that stem cell adhesion and proliferation is influenced by the surface roughness. The possible explanation is that the surface roughness provides necessary points for cell-surface contacts and thus increases cell adhesion. As the surface roughness decreases, it becomes harder for cells to form the adhesion sites. However, even the smooth surface has some structural inhomogeneity and by using these surface defects the cells can anchor themselves. The elongated cell shape of mES cells on the smooth and nano-rough surfaces supports this assumption.

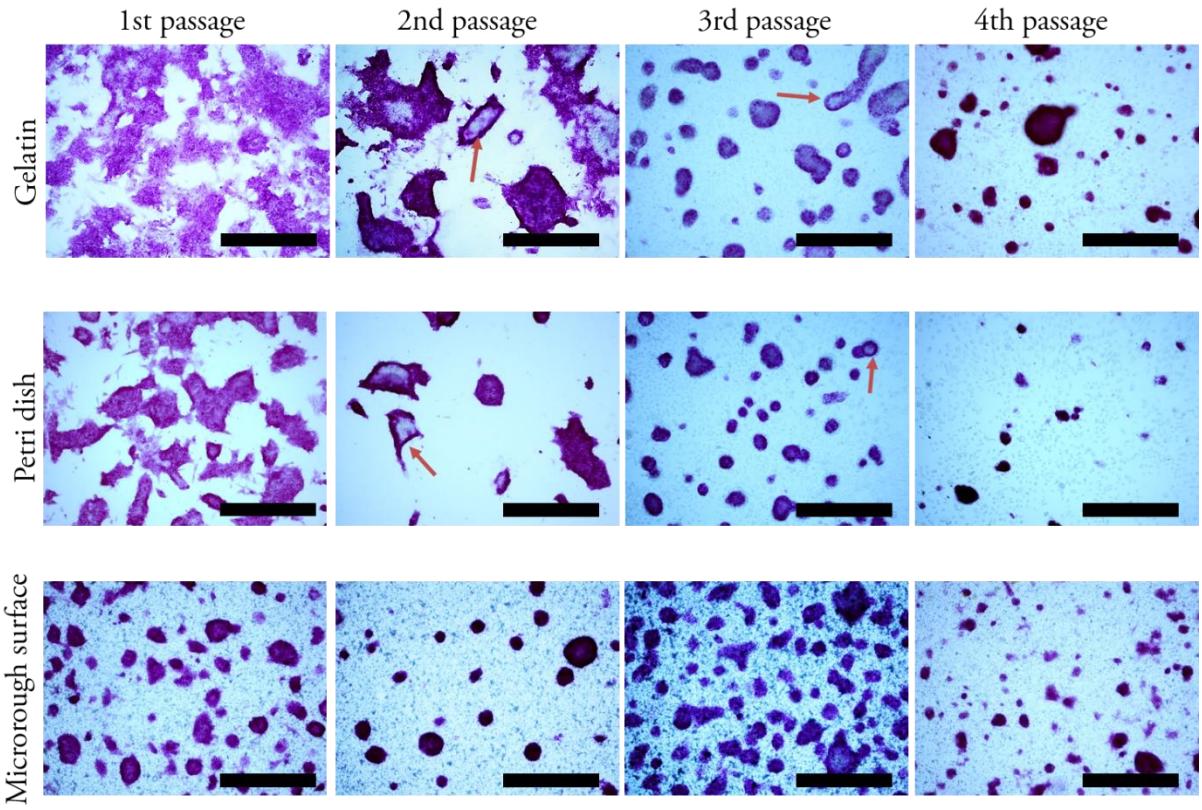

Figure 3.36: Alkaline phosphatase staining of mES cells after four passages cultured on the micro-rough polyHEMA surfaces, Petri dish and gelatin. Pluripotent stem cells were stained violet. Red arrows indicate mixed colonies. Scale bars 500 μm.

The microscopy images of AP stained mES cells on the micro-rough surfaces show completely different behavior (Figure 3.36). It can be seen that after the first and second passage there are mostly pluripotent stem cell colonies and no differentiated cells on all surfaces (microrough polyHEMA surface, Petri dish and gelatin). On the micro-rough surfaces, the stem cell colonies are smaller and more spherical and have more intense color of staining than on the gelatin and Petri dish. It was found that after the second passage, the amount of the unstained cells on the gelatin and Petri dish was elevated in comparison with that on the micro-rough surface. After the third passage, some cells appeared outside of the colony that were not stained. After four passages on all surfaces, there were still some stem cell colonies. However, on the gelatin and Petri dish surfaces there was a vast number of unstained cell surrounding the stem cell colonies. The mES colony shape on the micro-rough surface was round and the colony size was smaller compared those on the gelatin and Petri dish surfaces. After the second passage, there were some mixed stem cell colonies on the gelatin and Petri dish surfaces (red arrows in Figure 3.36). The mixed colonies were not completely stained indicating that they consisted of both stem cells and differentiated cells. After the fourth passage, the amount of differentiated cells significantly increased on the gelatin and Petri dish surfaces.

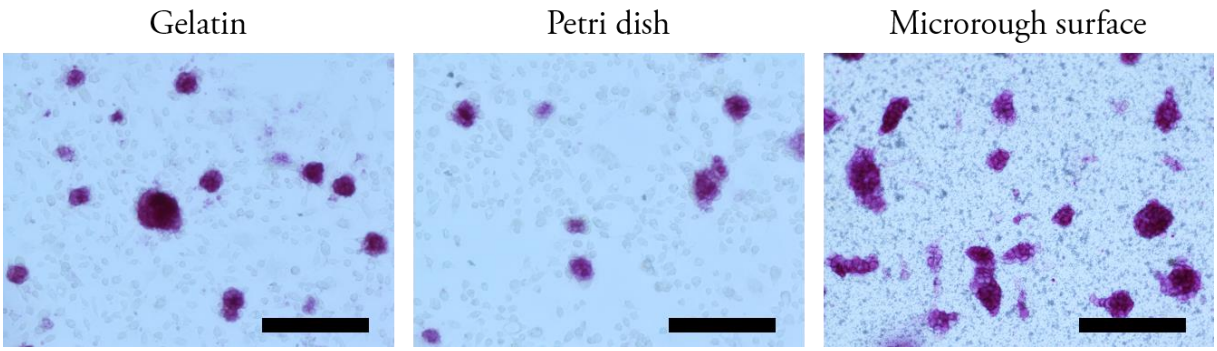

Figure 3.37: Alkaline phosphatase staining of the mES cell after 4 passages cultured on the micro-rough polyHEMA surfaces, Petri dish and Gelatin. Pluripotent stem cells were stained violet. Scale bars 100 μm

It was found that after the fourth passage on the gelatin and Petri dish surfaces, there were fewer stem cell colonies and their size decreased in comparison with that for the second and third passage. The unstained cells surrounded the stem cell colonies. However, on the micro-rough surface there were few unstained cells and the stem cell colony number was higher. The maintenance of stem cell pluripotency is a complicated process that depends on various factors both chemical and physical [150]. The presence of the required chemicals in the environment, produced by either the feeder cells or by the addition of supplements in the cell media, influences stem cell differentiation. It is possible that differentiated stem cells could act like the feeder cells and help to maintain stem cell differentiation on the gelatin and Petri dish surfaces after three passages. This might explain the presence of the undifferentiated stem cell on the gelatin and Petri dish surfaces in the later passages. The results of AP staining of mES cells on the micro-rough surface show that the mES cells were pluripotent after four passages, and stem cell colonies were compact and had spherical shape. However, the AP staining is a qualitative approach and further quantitative investigations were necessary.

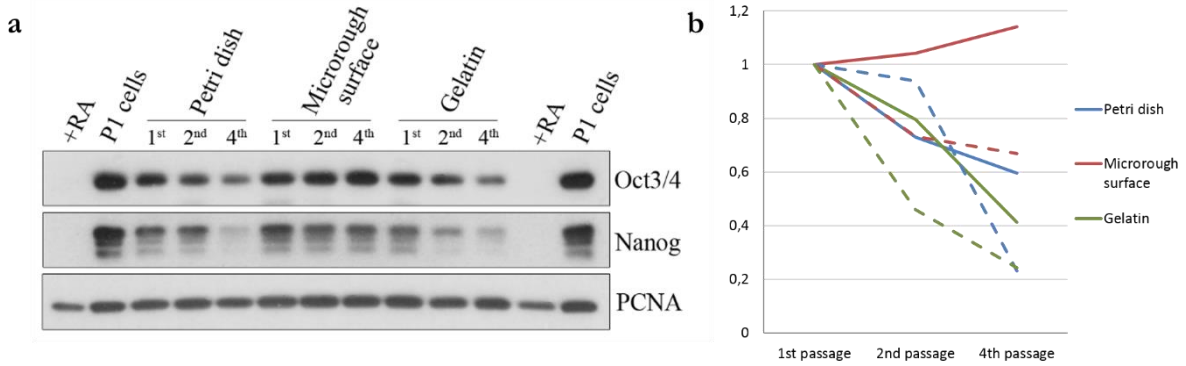

Figure 3.38: (a) The expression of the stem cell pluripotency markers Oct3/4 and Nanog were monitored by Western blotting. Hybridisation with an antibody targeted against PCNA was performed for the loading control. (b) The quantification of the expression of Oct3/4 (straight line) and Nanog (dashed line) relative to PCNA levels.

Genes and their expressed proteins that are characteristic to specific pluripotent stem cells can be used as stem cell markers. The different types of stem cells express different stem cell markers. Monitoring of the stem cell markers is a quantitative approach for the determination of stem cell pluripotency [151].

Oct-4 and Nanog are two homeodomain transcription factors that were the first identified markers necessary for early embryo development and pluripotency maintenance in embryonic stem cells [152], [153]. In addition to Oct4 and Nanog, other factors were found to be required for pluripotency, such as Sox2, SSEA-1, SSEA-4, Sall4, and Dax1. These pluripotency markers are part of the complicated transcriptional regulatory network in embryonic stem cells. Expression of the stem cell markers Oct3/4 and Nanog was monitored by Western blot analysis (Figure 3.38). Stem cells treated with retinoic acid (RA) were used as a negative control, since retinoic acid is known to induce stem cell differentiation [154], [155]. mES cells prior to the seeding onto the surfaces (P1 cells) were used as a positive control. The level of Oct3/4 and Nanog expression in the cells on the Petri dish and gelatin surfaces decreased with each passage as more of the stem cells differentiated. Expression of Oct3/4 and Nanog in the cells on the micro-rough surface was kept high through all four passages, indicating high maintenance of the stem cell pluripotency on this surface. Quantification of the expression levels of Oct3/4 showed that expression of the marker slightly increased for cells on the micro-rough surface. For cells on the Petri dish and gelatin surfaces, the expression of Oct3/4 was about 2 and 2.5 times lower, respectively, than that on the micro-rough surface after four passages. The expression of Nanog decreased for all tested surfaces, and for the micro-rough surface it was about 1.5 times lower than the initial expression level. However, for Petri dish and gelatin surfaces the expression level of Nanog decreased about 4 times relative to the initial expression level. This indicates that the expression level of Oct3/4 and Nanog in mES cells cultured on the micro-rough surface after four passages was significantly higher than that on the gelatin and Petri dish surfaces. Based on the AP staining and Western blot results, it may be concluded that after culturing mES cells for four passages on the micro-rough surface, many mES cells maintained their pluripotency.

Similar results were obtained by using a mES-Oct4-eGFP expressing cell line. These experiments were performed in close collaboration with Mona Jaggy and Tatjana Autenrieth (Martin Bastmeyer group, KIT). Oct4 is one of the four Yamanaka factors that are present only in pluripotent stem cells. Thus, by using the mES-Oct4-eGFP cell line it is possible to observe stem cell behavior without staining, as the pluripotent stem cells expressed GFP and could be directly observed using fluorescence microscopy. It was shown that indeed on the micro-rough surface the stem cells formed compact colonies without any differentiated cells (Appendix Figure 5.3). On the nano-rough and smooth surfaces after 3 days there was a large amount of differentiated stem cells surrounding the stem cell colonies. Similar findings were found by calculating the colony number and differentiating the colony by type: Oct4 positive, Oct4 negative or mixed colony (Appendix Figure 5.4). On the micro-rough surfaces, a higher number of Oct4 positive colonies and a low amount of the mixed colonies were observed. It should be noted that as the surface roughness decreased, the number of mixed colonies as well as Oct4 negative colonies increased, indicating that these surfaces promote stem cell differentiation. The mES-Oct4-eGFP cells were also cultured for long-term on the micro-rough surface (Appendix Figure 5.5). Even after three weeks of culturing, the mES cells formed compact spherical colonies that were Oct4 positive. Additionally, micro-rough polyHEMA surfaces were modified with decanethiol and aminethiol using consequent esterification and thiol-yne reactions. mES cells were cultured on the modified polyHEMA surfaces for three days (Appendix Figure 5.6). It was found that

stem cell differentiation did not depend on the surface chemistry, as for all tested surfaces the level of mES differentiation was almost identical.

The observed cell motility retardation and the maintenance of stem cell pluripotency on the micro-rough surface can be linked to the strong cell-surface interaction and inability of cells to disassemble primary adhesion contacts. Similarly, it can be hypothesized that the micro-rough surface provides optimal cell contacts. Previously, there have been reports regarding the effects of nanotopography on stem cell differentiation by the irregular formation of focal adhesion sites [156], [157]. It was shown that on surfaces with higher roughness the cell area was smaller and the expression of focal adhesion kinase (FAK) was higher. Therefore, SEM images of the cell-surface contacts of mES-Oct4-eGFP cells on micro-rough, nano-rough and smooth polyHEMA surface were captured (Appendix Figure 5.7). It was seen that cells on the micro-rough surface formed a high number of elongated protrusions inside the surface. Some of these cell-surface contacts, although smaller, can also be seen on the nano-rough surface. However, on the smooth surface, no cell-surface contacts are visible. This indicates that the connection of the cell to the surface is higher for the micro-rough surface and may lead to the observed reduced cell motility, as it would be harder for the cell to remove these contacts.

The formation of cell-surface contacts depends on the initial phase of the cell surface sensing. Surface features within a threshold of 35 nm in height are able to influence filopodia and guide cells [158], [159]. The ability of cells to sense the nanoscale sized surface features is achieved through individual integrin receptors, since the extracellular part of integrin receptors are around 23 nm wide and the final 5 nm of the integrin α- and β-chains is responsible for ligand binding [160]. It is therefore possible that on the smooth surface cells attach not by filopodia but by individual integrin receptors. However, the adhesion between cells and the substrate would be relatively weak. Additionally, the ~70 nm spacing between the integrin receptors would impose the spacing between surface features [122]. The surface features on the smooth surface were quite small and rare, making the formation of the cell-surface contacts difficult. Hence, on the smooth surface the attached cells had an elongated shape. This led to the observed reduced cell adhesion to the smooth surface. As the surface feature size increases the cells are able to sense the surface more easily, which might in turn lead to facilitated filopodia formation and anchoring. This assumption explains the observed multiple cell protrusions on the micro-rough and nano-rough surfaces. Formed cell protrusions would be difficult to disassemble, preventing cell spreading and motility.

3.3.6 Conclusions

PolyHEMA surfaces with different surface roughness were used for the study of cell motility and maintenance of stem cell pluripotency. PolyHEMA surfaces with micro and nano-roughness, as well as smooth polyHEMA surfaces were utilized. For the study of cell cross-contamination of the two cancer cell lines, the patterned micro-rough surfaces were prepared and the obtained results were compared to those for the patterned nano-rough surfaces. It was found that when cells were cultured in adjacent compartments

on the micro-rough surface, after 72h the cross-contamination was below 0.2%, while for the nano-rough surface after 72h the cross-contamination was 1.5%. The observed cell colonies had proliferated, however their position remained constant during the observation time. The possible reason for this observed effect was retarded cell motility. Therefore, cell motility assessment on the micro-rough, nano-rough and Petri dish samples was performed. Indeed, it was found that the path cells traveled on the nano-rough surface was three times longer than on the micro-rough surface. On the Petri dish surface, the cells traveled around half the distance than on the nano-rough surface, but still more than on the micro-rough surface. The obtained results showed that cells could not spread easily on the micro-rough surface and their movement was impaired.

The ability to reduce stem cell adhesion while maintaining capability for self-renewal and pluripotency is a promising prerequisite for developing an artificial stem cell culture system. mES stem cells were cultured on the surfaces with varying surface roughness for four passages. It was found that the cells did not grow well on the nano-rough and smooth surfaces due to low adhesion after seeding. Additionally, even after one passage the cells started to differentiate. Stem cells on the micro-rough surface formed compact spherical colonies and were able to maintain stem cell pluripotency for four passages, while on the control surfaces the mES cells started to differentiate. Additional experiments with mES-Oct4-eGFP stem cell lines were performed to further confirm the obtained results. mES-Oct4-eGFP cell cultured for three weeks on the micro-rough surface maintained their pluripotency. Micro-rough grooved polyHEMA surfaces were modified with aminethiol and decanethiol groups to study the influence of chemistry on stem cell differentiation. It was found that the surface chemistry did not have as much influence as the surface roughness.

Chapter 4

Conclusions and Outlook

In this work, the optimal surface morphology and surface topography for the development of superhydrophobic surfaces were investigated. This was done by modifying the existing method of preparation of porous polymethacrylate films. The method was modified so that the poly(2-hydroxyethyl methacrylate-*co*-ethylene dimethacrylate) (polyHEMA) and poly(butyl methacrylate-*co*-ethylene dimethacrylate) (polyBMA) surfaces with "grooved" and "protruded" surface topographies were produced with superhydrophilic (polyHEMA) or superhydrophobic (polyBMA) properties. Superhydrophilic polyHEMA surfaces were turned superhydrophobic via photografting with 2,2,3,3,3-pentafluoropropyl methacrylate (PFPMA) or chemical modification via esterification, followed by a modification with hydrophobic thiols using the thiol-yne reaction. Morphology, roughness and the surface wetting properties of the grooved and protruded polymer films were compared and the influence of the surface topography on the surface wetting properties was examined. Protruded surfaces had a highly porous morphology, whereas grooved surfaces consisted of disjointed agglomerates of polymer microglobules. Both, protruded and grooved polyHEMA surfaces showed water contact angles (WCA) close to ~0°. After polyHEMA surfaces were photografted with PFPMA, their morphology was changed. PolyHEMA globules on the protruded and grooved surfaces were covered with photografted polyPFPMA globules. On the protruded surface the size of the photografted polyPFPMA nanoglobules was ~800 nm, while on the grooved surface the size was ~90 nm. Due to the highly rough structure of both surfaces, they showed high static WCAs (~150° for the protruded and ~160° for the grooved surface), however difference in the surface topography led to high contact angle hysteresis (CAH) for the protruded (~20°) and low CAH (~3°) for the grooved surfaces. This indicated that the surface topography of the grooved polymer was advantageous for obtaining superhydrophobicity and specifically for low CAH. However, the polyHEMA surface photografted with PFPMA showed a hierarchical structure, which is known to improve hydrophobic properties of surfaces. The effect of the photografted polyPFPMA globules on surface wettability was tested using chemical modification of polyHEMA surfaces without altering their surface morphology. PolyHEMA surface modified with 1-decanethiol and *1H,1H,2H,2H*-perfluorodecanethiol possessed static WCAs of ~165 and CAHs of ~4°. The unmodified polyHEMA globules were found to consist of small mesoglobules ~30 nm in diameter, the presence of which might explain the observed high WCA and low CAH of chemically modified polyHEMA surfaces. These results show that the grooved polyHEMA surfaces modified by either photografting with PFPMA or by chemical modification with alkylthiols are suitable for the production of superhydrophobic surfaces with high WCAs and very low CAH. The method used to prepare grooved polyHEMA surfaces is fast, simple and allows for the control over surface features such as polymer globule size, surface thickness and transparency. These surfaces are promising as self-cleaning, antibiofouling, and bacteria repellent materials as well as in the fields of microfluidics and patterning.

Application of the grooved polyHEMA surface for the production of a microfluidic system based on the passive Laplace pump principle was shown in the next section of the thesis. The principle of the Laplace pump is based on the pressure difference between two droplets of different size. When the droplets were connected by a micro-channel, flow from the smaller (higher pressure) to the larger (lower pressure) droplet was generated. The micro-channels were produced by photografting the grooved polyHEMA surfaces with PFPMA using a photomask to create a hydrophilic-superhydrophobic micropattern. The production of liquid flow inside such hydrophilic micro-channel using the passive Laplace pump principle was shown. Due to the small dimensions of the micro-channel and low flow velocities generated, the formation of laminar flow in the T-shaped channel was observed. We also showed the ability to create complex multichannel microfluidic systems where more than two solutions can be applied. The effect of channel dimensions on the liquid flow was examined. For all tested channels, the flow was faster at the beginning and then slowed down towards the end of the experiment due to a decrease of the pressure difference between the inlet and outlet droplets with time. It was found that the reservoir diameter and the channel width were the primary parameters governing the liquid flow inside the channels. The flow was faster in the channels with large diameter of the outlet droplet, since the pressure inside the droplet decreases as the droplet size increases. Similarly, it was found that the flow was faster in the wider channel. This indicates that by adjusting the width of a channel and the size of the reservoir the flow rate can be controlled. The developed system of a pump-less generation of the liquid flow offers great advantages for designing microfluidic systems with reduced size and cost. There are only few systems which are comparatively simple while offering great versatility and functionality. The ability to generate laminar flow as well as complex liquid patterns is also important for designing miniaturized microfluidic devices for biotechnological and medical applications.

It is believed that surface roughness can be used to control cell adhesion, motility and stem cell differentiation. We used the ability to create polyHEMA surfaces with micro-rough, nano-rough and smooth surface morphologies in order to investigate cancer cell motility and stem cell differentiation as a function of surface roughness. It was found that the migration of two cancer cell lines (red fluorescent rat mammary carcinoma MTLy-mCherry and human cervical tumor cell line HeLa expressing GFP) on the microrough surface was significantly reduced, although the proliferation of the cells was not affected. Previously it was shown that the nano-rough surface did not have such an effect on the cell migration. Followed these experiments, assessment of cell motility was done for the micro-rough and nano-rough surfaces as well as a Petri dish. The cell path was three times shorter on the micro-rough surface than on the nano-rough surface. The obtained results might be explained by the inhibition of the trailing edge of the cell during the de-adhesion step of cell movement, which can be related to the strong interaction between the cell protrusions and the micro-rough surface. The inability of cells to remove their protrusions might prevent cells from detaching and moving. Similarly, it was observed that cells do not spread on the micro-rough surfaces. It can therefore be concluded that difficulty in the disassembly of formed cellular contacts prevents cell spreading and movement on the micro-rough surface.

The cell environment plays a crucial role in the maintenance of stem cell pluripotency or in the direction of cell differentiation. The ability to reduce cell adhesion in a similar way as the stem cells experience in the stem cell niche might help for the long-term culture of stem cells in vitro. As shown previously, the interaction of cancer cells with the micro-rough surface led to a significantly reduced cell motility possibly due to the strong interaction between the cells and the surface. This indicates that micro-rough surfaces might be able to delay stem cell differentiation by retarding cell adhesion and cell motility. To investigate this effect, mouse embryonic stem cells (mES cells) were cultured on the micro-rough, nano-rough and smooth polyHEMA surfaces for four passages. Stem cell adhesion after seeding on the nano-rough and smooth surface was extremely low and the majority of adhered cells differentiated. On the micro-rough surfaces, however, mES cells formed compact spherical colonies and were able to maintain stem cell pluripotency for four passages. This was confirmed by Alkaline Phosphatase (AP) staining, Western blot analysis and by using a mES-Oct4-eGFP expressing cell line (in cooperation with Prof. Bastmeyer). Additionally, SEM investigation of the cell-surface contact showed that the micro-rough surfaces promoted the formation of cell protrusions and strengthen cell-surface interaction. On the micro-rough surface the stem cell spreading process was inhibited, which might be responsible for the observed inhibition of cell differentiation. Previously, it was shown that surface elasticity and chemistry played major roles in the stem cell differentiation process. However, from the obtained results it can be concluded that surface roughness can be used to control stem cell differentiation and maintain stem cell pluripotency. This makes such surfaces promising for the multiplication of medically relevant but scarce stem cells in-vitro.

Chapter 5

Appendix

5.1 Appendix Figures

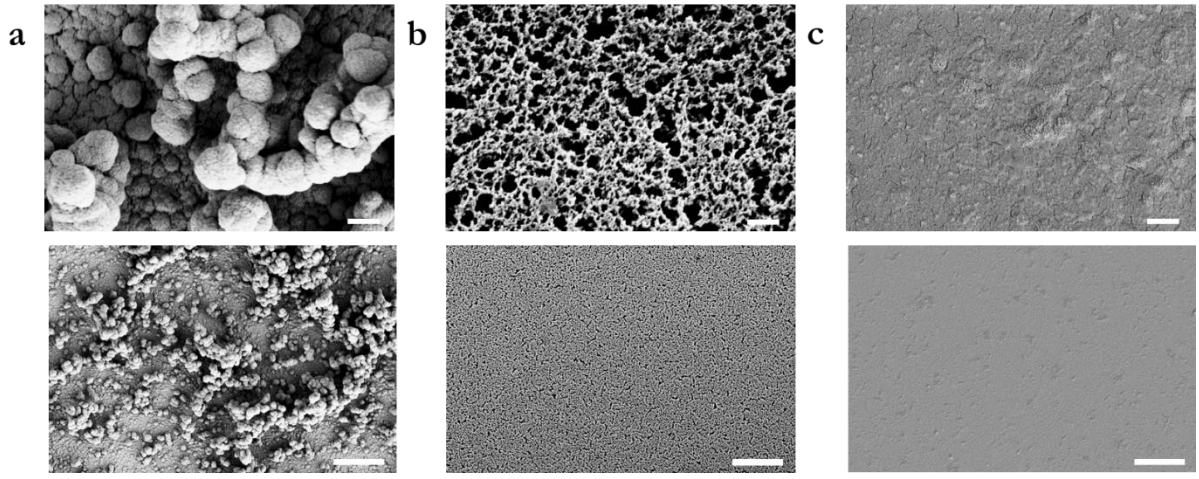

Appendix Figure 5.1: Surface morphology of polyHEMA (a) micro-rough, (b) nano-rough, and (c) smooth surfaces. Top row: high magnification SEM image. Scale bars 500 nm. Bottom row: low magnification SEM image. Scale bars are 5 μm

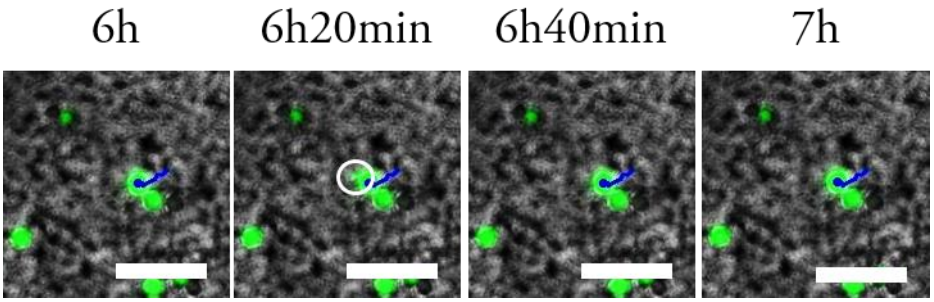

Appendix Figure 5.2: Formation of the filopodia by HeLa-EGFP cells cultured on the microrough surface. Scale bars 100 μm.

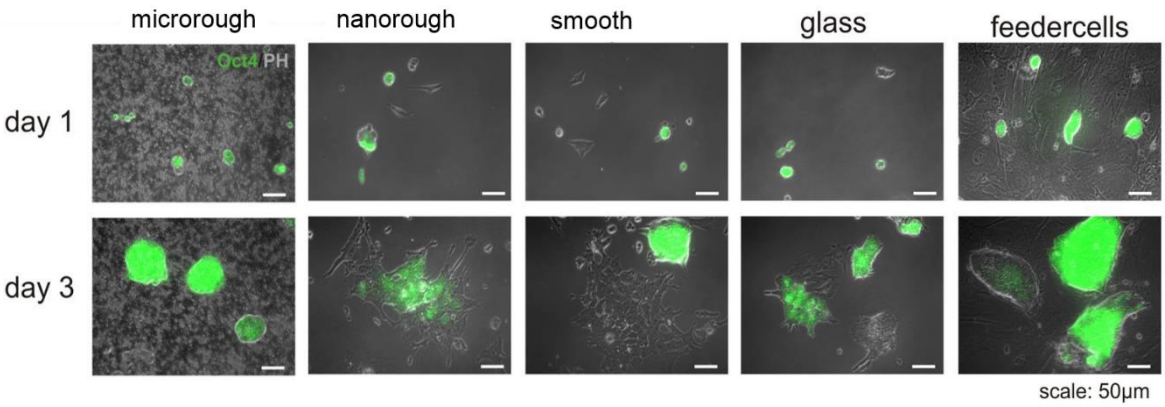

Appendix Figure 5.3: mES-Oct4-eGFP expressing cell lines on the micro-rough, nano-rough, smooth polyHEMA surfaces, on glass and on the feeder cells. Scale bars 50 µm.

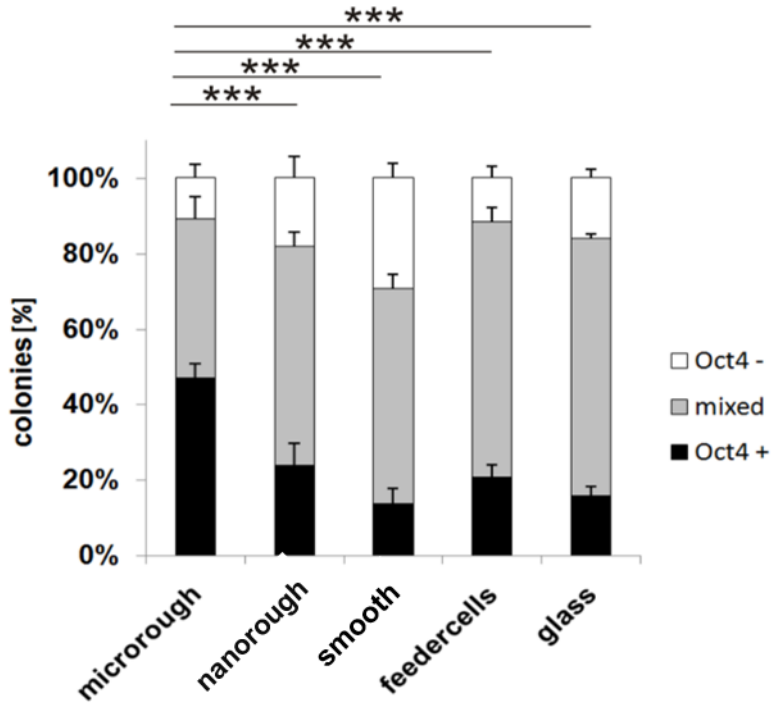

Appendix Figure 5.4: Percentage of the colonies of mES-Oct4-eGPF expressing cells after 3 days culturing on the micro-rough, nano-rough, smooth surfaces, on glass and on feeder cells. The colonies are divided by type as: Oct4 posititive colonies (pluripotent mES), mixed colonies where there are cells expressing and not expressing oct4, and Oct4 negative colonies.

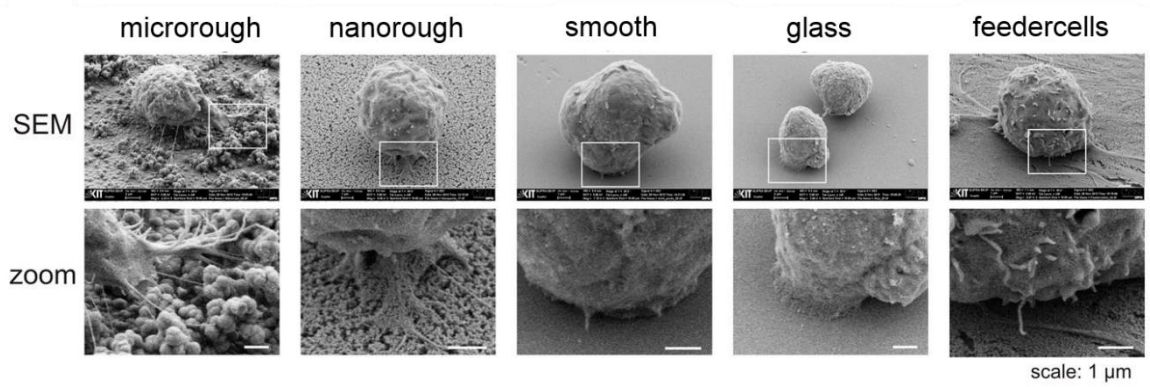

Appendix Figure 5.5: SEM images of the mES cells on the micro-rough, nano-rough, smooth, glass surfaces and on feeder cells.

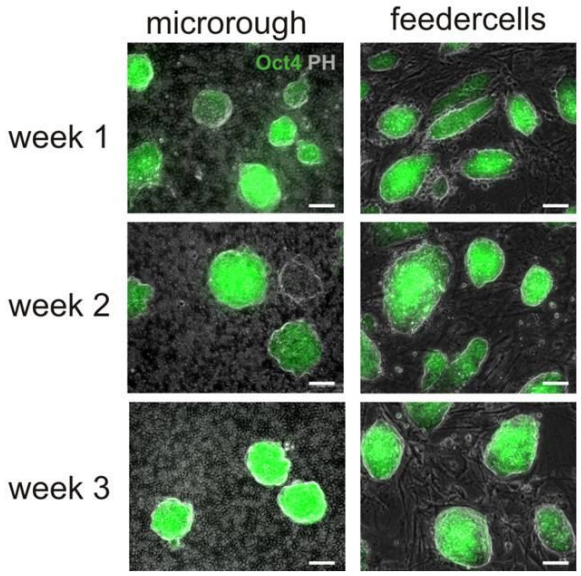

Appendix Figure 5.6: mES cells on the micro-rough surface and on the feeder cells after 3 weeks. Scale bars 50 µm.

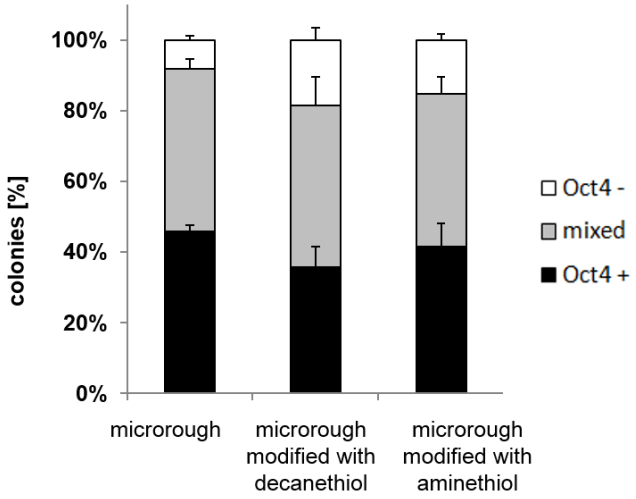

Appendix Figure 5.7: Percentage of the colonies of mES-Oct4-eGPF expressing cells after 3 days culturing on the micro-rough, micro-rough modified with decanethiol, micro-rough modified with aminethiol, on

glass and on feeder cells. The colonies are divided by type as: Oct4 posititive colonies (pluripotent mES), mixed colonies where there are cells expressing and not expressing oct4, and Oct4 negative colonies.

5.2 List of publications

Publications related to the Ph.D. thesis:

Nedashkivska V., Efremov A., Braun F., Gudadhe A., Grunze M., Levkin P. Highly rough superhydrophilic-superhydrophobic surfaces: morphology, wetting properties and cell behavior. *Langmuir* **2014** (in preparation)

Nedashkivska V., Maiwald M., Grunze M., Levkin P. Microfluidic systems based on passive Laplace pump. *Langmuir* **2014** (in preparation)

Jaggy M.‡, Nedashkivska V.‡, Zhang P., Autenrieth T., Greiner A., Bastmeyer M., Blattner C., Grunze M., Levkin P. Micro-rough polymer film for long-term maintenance of stem cell pluripotency. *Nature materials* **2014** (in preparation)

‡ These authors contribute equally to this work.

Other publications:

Ueda E., Geyer F.L., Nedashkivska V., Levkin P.A., DropletMicroarray: facile formation of arrays of microdroplets and hydrogel micropads for cell screening applications., *Lab Chip.* 12 (2012) 5218–24. doi:10.1039/c2lc40921f.

Nedashkivska V., Grunze M., Levkin P. Microparticle assembly through discontinuous dewetting on superhydrophilic-superhydrophobic micropatterns. *Langmuir* **2014** (in preparation)

Works published as master and bachelor student:

Zheltonozhskaya T., Nedashkovskaya V., Khutoryanskiy V., Gomza Y., Fedorchuk S., Klepko V., Partsevskaya, Micelles of PAAm-b-PEO-b-PAAm Triblock Copolymers and Their Binding with Prednisolon, *Molecular Crystals and Liquid Crystals*, 536 (1), **2011**, 148-159

Lyuksyutov S.F., Rackaitis M., Nedashkivska V., Instability of nanostructures patterned in polystyrene under high electric field gradients. *Applied Surface Science*, 257 (10), **2011**, 4581–4585

Bibliography

[1] P.-G. de Gennes, F. Brochard-Wyart, and D. Quere, *Capillarity and Wetting Phenomena: Drops, Bubbles, Pearls, Waves*. Springer, 2004, p. 291.

[2] G. D. Nadkarni and S. Garoff, "An Investigation of Microscopic Aspects of Contact Angle Hysteresis: Pinning of the Contact Line on a Single Defect," *Europhys. Lett.*, vol. 20, no. 6, pp. 523–528, Nov. 1992.

[3] T. Onda, S. Shibuichi, N. Satoh, and K. Tsujii, "Super-Water-Repellent Fractal Surfaces," *Langmuir*, vol. 12, no. 9, pp. 2125–2127, Jan. 1996.

[4] J. Drelich and E. Chibowski, "Superhydrophilic and superwetting surfaces: definition and mechanisms of control.," *Langmuir*, vol. 26, no. 24, pp. 18621–3, Dec. 2010.

[5] Y. C. Jung and B. Bhushan, "Contact angle, adhesion and friction properties of micro-and nanopatterned polymers for superhydrophobicity," *Nanotechnology*, vol. 17, no. 19, pp. 4970–4980, Oct. 2006.

[6] A. E. Rawlings, J. P. Bramble, and S. S. Staniland, "Innovation through imitation: biomimetic, bioinspired and biokleptic research," *Soft Matter*, vol. 8, no. 25, p. 6675, Jun. 2012.

[7] P. Fratzl, "Biomimetic materials research: what can we really learn from nature's structural materials?," *J. R. Soc. Interface*, vol. 4, no. 15, pp. 637–42, Aug. 2007.

[8] W. Barthlott and C. Neinhuis, "Purity of the sacred lotus, or escape from contamination in biological surfaces," *Planta*, vol. 202, no. 1, pp. 1–8, Apr. 1997.

[9] H. J. Ensikat, P. Ditsche-Kuru, C. Neinhuis, and W. Barthlott, "Superhydrophobicity in perfection: the outstanding properties of the lotus leaf.," *Beilstein J. Nanotechnol.*, vol. 2, no. 1, pp. 152–61, Jan. 2011.

[10] C. NEINHUIS, "Characterization and Distribution of Water-repellent, Self-cleaning Plant Surfaces," *Ann. Bot.*, vol. 79, no. 6, pp. 667–677, Jun. 1997.

[11] P. Wagner, "Quantitative assessment to the structural basis of water repellency in natural and technical surfaces," *J. Exp. Bot.*, vol. 54, no. 385, pp. 1295–1303, Apr. 2003.

[12] Z. Guo, W. Liu, and B.-L. Su, "Superhydrophobic surfaces: from natural to biomimetic to functional.," *J. Colloid Interface Sci.*, vol. 353, no. 2, pp. 335–355, Jan. 2011.

[13] H. G. Edelmann, C. Neinhuis, M. Jarvis, B. Evans, E. Fischer, and W. Barthlott, "Ultrastructure and chemistry of the cell wall of the moss Rhacocarpus purpurascens (Rhacocarpaceae): a puzzling architecture among plants," *Planta*, vol. 206, no. 2, pp. 315–321, Aug. 1998.

[14] P. M. Hayward and R. S. Clymo, "Profiles of Water Content and Pore Size in Sphagnum and Peat, and their Relation to Peat Bog Ecology," *Proc. R. Soc. B Biol. Sci.*, vol. 215, no. 1200, pp. 299–325, Jun. 1982.

[15] X. Gao and L. Jiang, "Biophysics: water-repellent legs of water striders.," *Nature*, vol. 432, no. 7013, p. 36, Nov. 2004.

[16] K. Koch, B. Bhushan, and W. Barthlott, "Diversity of structure, morphology and wetting of plant surfaces," *Soft Matter*, vol. 4, no. 10, p. 1943, Sep. 2008.

[17] K. Koch and W. Barthlott, "Superhydrophobic and superhydrophilic plant surfaces: an inspiration for biomimetic materials.," *Philos. Trans. A. Math. Phys. Eng. Sci.*, vol. 367, no. 1893, pp. 1487–509, Apr. 2009.

[18] K. Koch, B. Bhushan, and W. Barthlott, "Multifunctional surface structures of plants: An inspiration for biomimetics," *Prog. Mater. Sci.*, vol. 54, no. 2, pp. 137–178, Feb. 2009.

[19] E. Bormashenko, O. Gendelman, and G. Whyman, "Superhydrophobicity of Lotus Leaves versus Birds Wings: Different Physical Mechanisms Leading to the Similar Phenomena.," *Langmuir*, Sep. 2012.

[20] T. Young, "An Essay on the Cohesion of Fluids," *Philos. Trans. R. Soc. London*, vol. 95, pp. 65–87, Jan. 1805.

[21] T. Nishino, M. Meguro, K. Nakamae, M. Matsushita, and Y. Ueda, "The Lowest Surface Free Energy Based on −CF 3 Alignment," *Langmuir*, vol. 15, no. 13, pp. 4321–4323, Jun. 1999.

[22] R. N. Wenzel, "RESISTANCE OF SOLID SURFACES TO WETTING BY WATER," *Ind. Eng. Chem.*, vol. 28, no. 8, pp. 988–994, Aug. 1936.

[23] A. Lafuma and D. Quéré, "Superhydrophobic states.," *Nat. Mater.*, vol. 2, no. 7, pp. 457–60, Jul. 2003.

[24] A. B. D. Cassie and S. Baxter, "Wettability of porous surfaces," *Trans. Faraday Soc.*, vol. 40, p. 546, Jan. 1944.

[25] A. B. D. Cassie, "Contact angles," *Discuss. Faraday Soc.*, vol. 3, p. 11, Jan. 1948.

[26] A. J. B. Milne and A. Amirfazli, "The Cassie equation: How it is meant to be used," *Adv. Colloid Interface Sci.*, vol. 170, no. 1, pp. 48–55, 2012.

[27] R. Fürstner, W. Barthlott, C. Neinhuis, and P. Walzel, "Wetting and self-cleaning properties of artificial superhydrophobic surfaces.," *Langmuir*, vol. 21, no. 3, pp. 956–61, Feb. 2005.

[28] D. Quéré, "Non-sticking drops," *Reports Prog. Phys.*, vol. 68, no. 11, pp. 2495–2532, Nov. 2005.

[29] J. C. Bird, R. Dhiman, H.-M. Kwon, and K. K. Varanasi, "Reducing the contact time of a bouncing drop.," *Nature*, vol. 503, no. 7476, pp. 385–8, Nov. 2013.

[30] N. A. Patankar, "On the Modeling of Hydrophobic Contact Angles on Rough Surfaces," *Langmuir*, vol. 19, no. 4, pp. 1249–1253, Jan. 2003.

[31] A. Marmur, "Wetting on Hydrophobic Rough Surfaces: To Be Heterogeneous or Not To Be?," *Langmuir*, vol. 19, no. 20, pp. 8343–8348, Sep. 2003.

[32] J. Bico, C. Marzolin, and D. Quéré, "Pearl drops," *Europhys. Lett.*, vol. 47, no. 2, pp. 220–226, Jul. 1999.

[33] E. Bormashenko, R. Pogreb, G. Whyman, and M. Erlich, "Cassie-Wenzel wetting transition in vibrating drops deposited on rough surfaces: is the dynamic Cassie-Wenzel wetting transition a 2D or 1D affair?," *Langmuir*, vol. 23, no. 12, pp. 6501–3, Jun. 2007.

[34] R. J. Vrancken, H. Kusumaatmaja, K. Hermans, A. M. Prenen, O. Pierre-Louis, C. W. M. Bastiaansen, and D. J. Broer, "Fully reversible transition from Wenzel to Cassie-Baxter states on corrugated superhydrophobic surfaces.," *Langmuir*, vol. 26, no. 5, pp. 3335–41, Mar. 2010.

[35] C. W. Extrand, "Criteria for Ultralyophobic Surfaces," *Langmuir*, vol. 20, no. 12, pp. 5013–5018, Jun. 2004.

[36] N. A. Patankar, "Transition between superhydrophobic states on rough surfaces.," *Langmuir*, vol. 20, no. 17, pp. 7097–102, Aug. 2004.

[37] B. Bhushan, M. Nosonovsky, and Y. C. Jung, "Towards optimization of patterned superhydrophobic surfaces.," *J. R. Soc. Interface*, vol. 4, no. 15, pp. 643–8, Aug. 2007.

[38] Y. C. Jung and B. Bhushan, "Wetting transition of water droplets on superhydrophobic patterned surfaces," *Scr. Mater.*, vol. 57, no. 12, pp. 1057–1060, 2007.

[39] Y.-J. Sheng, S. Jiang, and H.-K. Tsao, "Effects of geometrical characteristics of surface roughness on droplet wetting.," *J. Chem. Phys.*, vol. 127, no. 23, p. 234704, Dec. 2007.

[40] H. Kusumaatmaja and J. M. Yeomans, "Modeling contact angle hysteresis on chemically patterned and superhydrophobic surfaces.," *Langmuir*, vol. 23, no. 11, pp. 6019–32, May 2007.

[41] B. He, J. Lee, and N. A. Patankar, "Contact angle hysteresis on rough hydrophobic surfaces," *Colloids Surfaces A Physicochem. Eng. Asp.*, vol. 248, no. 1, pp. 101–104, 2004.

[42] L. Gao and T. J. McCarthy, "Contact angle hysteresis explained.," *Langmuir*, vol. 22, no. 14, pp. 6234–7, Jul. 2006.

[43] J. Wu, J. Xia, W. Lei, and B. Wang, "Advanced understanding of stickiness on superhydrophobic surfaces.," *Sci. Rep.*, vol. 3, p. 3268, Jan. 2013.

[44] R. Tadmor, "Line energy and the relation between advancing, receding, and young contact angles.," *Langmuir*, vol. 20, no. 18, pp. 7659–64, Aug. 2004.

[45] E. Chibowski and K. Terpilowski, "Surface free energy of sulfur--revisited I. Yellow and orange samples solidified against glass surface.," *J. Colloid Interface Sci.*, vol. 319, no. 2, pp. 505–13, Mar. 2008.

[46] M. Nosonovsky and B. Bhushan, "Wetting of rough three-dimensional superhydrophobic surfaces," *Microsyst. Technol.*, vol. 12, no. 3, pp. 273–281, Nov. 2005.

[47] L. Gao and T. J. McCarthy, "How Wenzel and cassie were wrong.," *Langmuir*, vol. 23, no. 7, pp. 3762–5, Mar. 2007.

[48] C. W. Extrand, "Contact Angles and Hysteresis on Surfaces with Chemically Heterogeneous Islands," *Langmuir*, vol. 19, no. 9, pp. 3793–3796, Apr. 2003.

[49] N. Anantharaju, M. V Panchagnula, S. Vedantam, S. Neti, and S. Tatic-Lucic, "Effect of three-phase contact line topology on dynamic contact angles on heterogeneous surfaces.," *Langmuir*, vol. 23, no. 23, pp. 11673–6, Nov. 2007.

[50] M. V Panchagnula and S. Vedantam, "Comment on How Wenzel and Cassie Were Wrong by Gao and McCarthy.," *Langmuir*, vol. 23, no. 26, p. 13242; discussion 13243, Dec. 2007.

[51] M. Nosonovsky, "On the range of applicability of the Wenzel and Cassie equations.," *Langmuir*, vol. 23, no. 19, pp. 9919–20, Sep. 2007.

[52] E. Bormashenko, "Why does the Cassie–Baxter equation apply?," *Colloids Surfaces A Physicochem. Eng. Asp.*, vol. 324, no. 1–3, pp. 47–50, Jul. 2008.

[53] G. Wolansky and A. Marmur, "Apparent contact angles on rough surfaces: the Wenzel equation revisited," *Colloids Surfaces A Physicochem. Eng. Asp.*, vol. 156, no. 1–3, pp. 381–388, Oct. 1999.

[54] A. Marmur and E. Bittoun, "When Wenzel and Cassie are right: reconciling local and global considerations.," *Langmuir*, vol. 25, no. 3, pp. 1277–81, Feb. 2009.

[55] H. Y. Erbil and C. E. Cansoy, "Range of applicability of the Wenzel and Cassie-Baxter equations for superhydrophobic surfaces.," *Langmuir*, vol. 25, no. 24, pp. 14135–45, Dec. 2009.

[56] G. McHale, "Cassie and Wenzel: were they really so wrong?," *Langmuir*, vol. 23, no. 15, pp. 8200–5, Jul. 2007.

[57] B. . Derjaguin and N. . Churaev, "Structural component of disjoining pressure," *J. Colloid Interface Sci.*, vol. 49, no. 2, pp. 249–255, 1974.

[58] G. E. Ewing, "Ambient thin film water on insulator surfaces.," *Chem. Rev.*, vol. 106, no. 4, pp. 1511–26, Apr. 2006.

[59] B. Bhushan, K. Koch, and Y. C. Jung, "Nanostructures for superhydrophobicity and low adhesion," *Soft Matter*, vol. 4, no. 9, p. 1799, Aug. 2008.

[60] A. Marmur, "The Lotus Effect: Superhydrophobicity and Metastability," *Langmuir*, vol. 20, no. 9, pp. 3517–3519, Apr. 2004.

[61] C. W. Extrand, "Repellency of the lotus leaf: resistance to water intrusion under hydrostatic pressure.," *Langmuir*, vol. 27, no. 11, pp. 6920–5, Jun. 2011.

[62] N. A. Patankar, "Mimicking the lotus effect: influence of double roughness structures and slender pillars.," *Langmuir*, vol. 20, no. 19, pp. 8209–13, Sep. 2004.

[63] T. Liu, W. Sun, X. Sun, and H. Ai, "Thermodynamic analysis of the effect of the hierarchical architecture of a superhydrophobic surface on a condensed drop state.," *Langmuir*, vol. 26, no. 18, pp. 14835–41, Sep. 2010.

[64] S. H. Sajadinia and F. Sharif, "Thermodynamic analysis of the wetting behavior of dual scale patterned hydrophobic surfaces," *J. Colloid Interface Sci.*, vol. 344, no. 2, pp. 575–583, 2010.

[65] H. E. Jeong, S. H. Lee, J. K. Kim, and K. Y. Suh, "Nanoengineered multiscale hierarchical structures with tailored wetting properties.," *Langmuir*, vol. 22, no. 4, pp. 1640–5, Feb. 2006.

[66] Y. Su, B. Ji, K. Zhang, H. Gao, Y. Huang, and K. Hwang, "Nano to micro structural hierarchy is crucial for stable superhydrophobic and water-repellent surfaces.," *Langmuir*, vol. 26, no. 7, pp. 4984–9, Apr. 2010.

[67] M. Nosonovsky, "Multiscale roughness and stability of superhydrophobic biomimetic interfaces.," *Langmuir*, vol. 23, no. 6, pp. 3157–61, Mar. 2007.

[68] Y. Yu, Z.-H. Zhao, and Q.-S. Zheng, "Mechanical and superhydrophobic stabilities of two-scale surfacial structure of lotus leaves.," *Langmuir*, vol. 23, no. 15, pp. 8212–6, Jul. 2007.

[69] L. Gao and T. J. McCarthy, "The 'lotus effect' explained: two reasons why two length scales of topography are important.," *Langmuir*, vol. 22, no. 7, pp. 2966–7, Mar. 2006.

[70] E. Bittoun and A. Marmur, "The Role of Multi-Scale Roughness in the Lotus Effect: Is it essential for Super-Hydrophobicity?," *Langmuir*, Sep. 2012.

[71] S.-J. Choi, H. N. Kim, W. G. Bae, and K.-Y. Suh, "Modulus- and surface energy-tunable ultraviolet-curable polyurethane acrylate: properties and applications," *J. Mater. Chem.*, vol. 21, no. 38, p. 14325, Sep. 2011.

[72] M. Heckele and W. K. Schomburg, "Review on micro molding of thermoplastic polymers," *J. Micromechanics Microengineering*, vol. 14, no. 3, pp. R1–R14, Mar. 2004.

[73] X.-M. Zhao, Y. Xia, and G. M. Whitesides, "Soft lithographic methods for nano-fabrication," *J. Mater. Chem.*, vol. 7, no. 7, pp. 1069–1074, Jan. 1997.

[74] C. Greiner, E. Arzt, and A. del Campo, "Hierarchical Gecko-Like Adhesives," *Adv. Mater.*, vol. 21, no. 4, pp. 479–482, Jan. 2009.

[75] H. E. Jeong, R. Kwak, J. K. Kim, and K. Y. Suh, "Generation and self-replication of monolithic, dual-scale polymer structures by two-step capillary-force lithography.," *Small*, vol. 4, no. 11, pp. 1913–8, Nov. 2008.

[76] A. Carlson, A. M. Bowen, Y. Huang, R. G. Nuzzo, and J. A. Rogers, "Transfer printing techniques for materials assembly and micro/nanodevice fabrication.," *Adv. Mater.*, vol. 24, no. 39, pp. 5284–318, Oct. 2012.

[77] L.-R. Bao, X. Cheng, X. D. Huang, L. J. Guo, S. W. Pang, and A. F. Yee, "Nanoimprinting over topography and multilayer three-dimensional printing," *J. Vac. Sci. Technol. B Microelectron. Nanom. Struct.*, vol. 20, no. 6, p. 2881, Dec. 2002.

[78] H. Ooe, M. Morimatsu, T. Yoshikawa, H. Kawata, and Y. Hirai, "Three-dimensional multilayered microstructure fabricated by imprint lithography," *J. Vac. Sci. Technol. B Microelectron. Nanom. Struct.*, vol. 23, no. 2, p. 375, Feb. 2005.

[79] J.-H. Lee, C.-H. Kim, K.-M. Ho, and K. Constant, "Two-Polymer Microtransfer Molding for Highly Layered Microstructures," *Adv. Mater.*, vol. 17, no. 20, pp. 2481–2485, Oct. 2005.

[80] S. Kim, J. Wu, A. Carlson, S. H. Jin, A. Kovalsky, P. Glass, Z. Liu, N. Ahmed, S. L. Elgan, W. Chen, P. M. Ferreira, M. Sitti, Y. Huang, and J. A. Rogers, "Microstructured elastomeric surfaces with reversible adhesion and examples of their use in deterministic assembly by transfer printing.," *Proc. Natl. Acad. Sci. U. S. A.*, vol. 107, no. 40, pp. 17095–100, Oct. 2010.

[81] H.-J. Tsai and Y.-L. Lee, "Facile method to fabricate raspberry-like particulate films for superhydrophobic surfaces.," *Langmuir*, vol. 23, no. 25, pp. 12687–92, Dec. 2007.

[82] Y. Xiu, L. Zhu, D. W. Hess, and C. P. Wong, "Biomimetic creation of hierarchical surface structures by combining colloidal self-assembly and Au sputter deposition.," *Langmuir*, vol. 22, no. 23, pp. 9676–81, Nov. 2006.

[83] W. Ma, H. Wu, Y. Higaki, H. Otsuka, and A. Takahara, "A 'non-sticky' superhydrophobic surface prepared by self-assembly of fluoroalkyl phosphonic acid on a hierarchically micro/nanostructured alumina gel film.," *Chem. Commun. (Camb).*, vol. 48, no. 54, pp. 6824–6, Jul. 2012.

[84] Y. Li, X. J. Huang, S. H. Heo, C. C. Li, Y. K. Choi, W. P. Cai, and S. O. Cho, "Superhydrophobic bionic surfaces with hierarchical microsphere/SWCNT composite arrays.," *Langmuir*, vol. 23, no. 4, pp. 2169–74, Feb. 2007.

[85] W. Ming, D. Wu, R. van Benthem, and G. de With, "Superhydrophobic films from raspberry-like particles.," *Nano Lett.*, vol. 5, no. 11, pp. 2298–301, Nov. 2005.

[86] D. Ebert and B. Bhushan, "Durable Lotus-effect surfaces with hierarchical structure using micro- and nanosized hydrophobic silica particles.," *J. Colloid Interface Sci.*, vol. 368, no. 1, pp. 584–91, Feb. 2012.

[87] K.-Y. Yeh, K.-H. Cho, and L.-J. Chen, "Preparation of superhydrophobic surfaces of hierarchical structure of hybrid from nanoparticles and regular pillar-like pattern.," *Langmuir*, vol. 25, no. 24, pp. 14187–94, Dec. 2009.

[88] B. Cortese, S. D'Amone, M. Manca, I. Viola, R. Cingolani, and G. Gigli, "Superhydrophobicity due to the hierarchical scale roughness of PDMS surfaces.," *Langmuir*, vol. 24, no. 6, pp. 2712–8, Mar. 2008.

[89] C. Viklund, F. Svec, J. M. J. Fréchet, and K. Irgum, "Monolithic, 'Molded', Porous Materials with High Flow Characteristics for Separations, Catalysis, or Solid-Phase Chemistry: Control of Porous Properties during Polymerization," *Chem. Mater.*, vol. 8, no. 3, pp. 744–750, Jan. 1996.

[90] E. Ueda, F. L. Geyer, V. Nedashkivska, and P. A. Levkin, "DropletMicroarray: facile formation of arrays of microdroplets and hydrogel micropads for cell screening applications.," *Lab Chip*, vol. 12, no. 24, pp. 5218–24, Dec. 2012.

[91] A. N. Efremov, E. Stanganello, A. Welle, S. Scholpp, and P. A. Levkin, "Micropatterned superhydrophobic structures for the simultaneous culture of multiple cell types and the study of cell-cell communication.," *Biomaterials*, vol. 34, no. 7, pp. 1757–63, Feb. 2013.

[92] B. Rånby, W. T. Yang, and O. Tretinnikov, "Surface photografting of polymer fibers, films and sheets," *Nucl. Instruments Methods Phys. Res. Sect. B Beam Interact. with Mater. Atoms*, vol. 151, no. 1–4, pp. 301–305, May 1999.

[93] A. Nakajima, K. Hashimoto, T. Watanabe, K. Takai, G. Yamauchi, and A. Fujishima, "Transparent Superhydrophobic Thin Films with Self-Cleaning Properties," *Langmuir*, vol. 16, no. 17, pp. 7044–7047, Aug. 2000.

[94] R. Blossey, "Self-cleaning surfaces--virtual realities.," *Nat. Mater.*, vol. 2, no. 5, pp. 301–6, May 2003.

[95] N. J. Shirtcliffe, G. McHale, and M. I. Newton, "Wet adhesion and adhesive locomotion of snails on anti-adhesive non-wetting surfaces.," *PLoS One*, vol. 7, no. 5, p. e36983, Jan. 2012.

[96] X.-J. Huang, D.-H. Kim, M. Im, J.-H. Lee, J.-B. Yoon, and Y.-K. Choi, "'Lock-and-key' geometry effect of patterned surfaces: wettability and switching of adhesive force.," *Small*, vol. 5, no. 1, pp. 90–4, Jan. 2009.

[97] J. Genzer and K. Efimenko, "Recent developments in superhydrophobic surfaces and their relevance to marine fouling: a review.," *Biofouling*, vol. 22, no. 5–6, pp. 339–60, Jan. 2006.

[98] A. Kazemzadeh, P. Ganesan, F. Ibrahim, S. He, and M. J. Madou, "The Effect of Contact Angles and Capillary Dimensions on the Burst Frequency of Super Hydrophilic and Hydrophilic Centrifugal Microfluidic Platforms, a CFD Study.," *PLoS One*, vol. 8, no. 9, p. e73002, Jan. 2013.

[99] H. Zhang, Y. Lee, K. Leck, N. Kim, and J. Ying, "Recyclable Hydrophilic−Hydrophobic Micropatterns on Glass for Microarray Applications," *Langmuir*, vol. 23, no. 9, p. 4728, 2007.

[100] M. J. Hancock, F. Yanagawa, Y.-H. Jang, J. He, N. N. Kachouie, H. Kaji, and A. Khademhosseini, "Designer Hydrophilic Regions Regulate Droplet Shape for Controlled Surface Patterning and 3D Microgel Synthesis," *Small*, vol. 8, no. 3, p. n–a, Feb. 2011.

[101] P. Levkin, F. Svec, and J. Frechet, "Porous Polymer Coatings: a Versatile Approach to Superhydrophobic Surfaces," *Adv. Funct. Mater.*, vol. 19, no. 12, p. 1993, 2009.

[102] F. L. Geyer, E. Ueda, U. Liebel, N. Grau, and P. A. Levkin, "Superhydrophobic-superhydrophilic micropatterning: towards genome-on-a-chip cell microarrays.," *Angew. Chem. Int. Ed. Engl.*, vol. 50, no. 36, pp. 8424–7, Aug. 2011.

[103] N. Martys and J. Douglas, "Critical properties and phase separation in lattice Boltzmann fluid mixtures," *Phys. Rev. E*, vol. 63, no. 3, p. 031205, Feb. 2001.

[104] J. T. Han, Y. Jang, D. Y. Lee, J. H. Park, S.-H. Song, D.-Y. Ban, and K. Cho, "Fabrication of a bionic superhydrophobic metal surface by sulfur-induced morphological development," *J. Mater. Chem.*, vol. 15, no. 30, p. 3089, Jul. 2005.

[105] P. N. Nge, C. I. Rogers, and A. T. Woolley, "Advances in Microfluidic Materials, Functions, Integration, and Applications.," *Chem. Rev.*, Feb. 2013.

[106] J. C. McDonald and G. M. Whitesides, "Poly(dimethylsiloxane) as a Material for Fabricating Microfluidic Devices," *Acc. Chem. Res.*, vol. 35, no. 7, pp. 491–499, Jul. 2002.

[107] J. Friend and L. Yeo, "Fabrication of microfluidic devices using polydimethylsiloxane.," *Biomicrofluidics*, vol. 4, no. 2, Jan. 2010.

[108] H. Gau, "Liquid Morphologies on Structured Surfaces: From Microchannels to Microchips," *Science (80-.).*, vol. 283, no. 5398, p. 46, 1999.

[109] J. Seo, S. Lee, J. Lee, and T. Lee, "Guided Transport of Water Droplets on Superhydrophobic–Hydrophilic Patterned Si Nanowires," *ACS Appl. Mater. Interfaces*, vol. 3, no. 12, p. 4722, 2011.

[110] A. C. Glavan, R. V Martinez, E. J. Maxwell, A. B. Subramaniam, R. M. D. Nunes, S. Soh, and G. M. Whitesides, "Rapid fabrication of pressure-driven open-channel microfluidic devices in omniphobic R(F) paper.," *Lab Chip*, vol. 13, no. 15, pp. 2922–30, Aug. 2013.

[111] P. Lam, K. Wynne, and G. Wnek, "Surface-Tension-Confined Microfluidics," *Langmuir*, vol. 18, no. 3, p. 948, 2002.

[112] "Download to Citation Manager." [Online]. Available: http://rstl.royalsocietypublishing.org/citmgr?gca=roypt;174/0/935. [Accessed: 25-Aug-2014].

[113] A. B. and J. S. / H. P. B. and F. Romesberg, D. B. Weibel, and G. M. Whitesides, "Applications of microfluidics in chemical biology," *Curr. Opin. Chem. Biol.*, vol. 10, no. 6, pp. 584–591, 2006.

[114] T. Ishizaki, N. Saito, and O. Takai, "Correlation of cell adhesive behaviors on superhydrophobic, superhydrophilic, and micropatterned superhydrophobic/superhydrophilic surfaces to their surface chemistry.," *Langmuir*, vol. 26, no. 11, pp. 8147–54, Jun. 2010.

[115] D. E. Discher, P. Janmey, and Y.-L. Wang, "Tissue cells feel and respond to the stiffness of their substrate.," *Science*, vol. 310, no. 5751, pp. 1139–43, Nov. 2005.

[116] A. J. Engler, S. Sen, H. L. Sweeney, and D. E. Discher, "Matrix Elasticity Directs Stem Cell Lineage Specification," *Cell.*, vol. 126, no. 4, pp. 677–689, 2006.

[117] A. Ranella, M. Barberoglou, S. Bakogianni, C. Fotakis, and E. Stratakis, "Tuning cell adhesion by controlling the roughness and wettability of 3D micro/nano silicon structures," *Acta Biomater.*, vol. 6, no. 7, pp. 2711–2720, 2010.

[118] M. J. Dalby, N. Gadegaard, and R. O. C. Oreffo, "Harnessing nanotopography and integrin-matrix interactions to influence stem cell fate.," *Nat. Mater.*, vol. 13, no. 6, pp. 558–69, Jun. 2014.

[119] R. HYNES, "Integrins: A family of cell surface receptors," *Cell*, vol. 48, no. 4, pp. 549–554, Feb. 1987.

[120] B. Geiger, J. P. Spatz, and A. D. Bershadsky, "Environmental sensing through focal adhesions.," *Nat. Rev. Mol. Cell Biol.*, vol. 10, no. 1, pp. 21–33, Jan. 2009.

[121] R. Ananthakrishnan, "The Forces Behind Cell Movement," *Int. J. Biol. Sci.*, pp. 303–317, 2007.

[122] E. A. Cavalcanti-Adam, T. Volberg, A. Micoulet, H. Kessler, B. Geiger, and J. P. Spatz, "Cell spreading and focal adhesion dynamics are regulated by spacing of integrin ligands.," *Biophys. J.*, vol. 92, no. 8, pp. 2964–74, Apr. 2007.

[123] E. F. Plow, T. A. Haas, L. Zhang, J. Loftus, and J. W. Smith, "Ligand binding to integrins.," *J. Biol. Chem.*, vol. 275, no. 29, pp. 21785–8, Jul. 2000.

[124] A. L. Berrier and K. M. Yamada, "Cell-matrix adhesion.," *J. Cell. Physiol.*, vol. 213, no. 3, pp. 565–73, Dec. 2007.

[125] S. M. Rafelski and J. A. Theriot, "Crawling toward a unified model of cell mobility: spatial and temporal regulation of actin dynamics.," *Annu. Rev. Biochem.*, vol. 73, pp. 209–39, Jan. 2004.

[126] A. J. Ridley, M. A. Schwartz, K. Burridge, R. A. Firtel, M. H. Ginsberg, G. Borisy, J. T. Parsons, and A. R. Horwitz, "Cell migration: integrating signals from front to back.," *Science*, vol. 302, no. 5651, pp. 1704–9, Dec. 2003.

[127] T. J. Mitchison and L. P. Cramer, "Actin-based cell motility and cell locomotion.," *Cell*, vol. 84, no. 3, pp. 371–9, Feb. 1996.

[128] W. Chen, L. G. Villa-Diaz, Y. Sun, S. Weng, J. K. Kim, R. H. W. Lam, L. Han, R. Fan, P. H. Krebsbach, and J. Fu, "Nanotopography influences adhesion, spreading, and self-renewal of human embryonic stem cells.," *ACS Nano*, vol. 6, no. 5, pp. 4094–103, May 2012.

[129] E. K. F. Yim, S. W. Pang, and K. W. Leong, "Synthetic nanostructures inducing differentiation of human mesenchymal stem cells into neuronal lineage.," *Exp. Cell Res.*, vol. 313, no. 9, pp. 1820–9, May 2007.

[130] B. K. K. Teo, S. T. Wong, C. K. Lim, T. Y. S. T. Y. S. Kung, C. H. Yap, Y. Ramagopal, L. H. Romer, E. K. F. Yim, and Y. Ramgopal, "Nanotopography modulates mechanotransduction of stem cells and induces differentiation through focal adhesion kinase.," *ACS Nano*, vol. 7, no. 6, pp. 4785–98, Jun. 2013.

[131] D. S. W. Benoit, M. P. Schwartz, A. R. Durney, and K. S. Anseth, "Small functional groups for controlled differentiation of hydrogel-encapsulated human mesenchymal stem cells.," *Nat. Mater.*, vol. 7, no. 10, pp. 816–23, Oct. 2008.

[132] M. Nagaoka, K. Si-Tayeb, T. Akaike, and S. A. Duncan, "Culture of human pluripotent stem cells using completely defined conditions on a recombinant E-cadherin substratum.," *BMC Dev. Biol.*, vol. 10, no. 1, p. 60, Jan. 2010.

[133] F. Ulloa-Montoya, C. M. Verfaillie, and W.-S. Hu, "Culture systems for pluripotent stem cells.," *J. Biosci. Bioeng.*, vol. 100, no. 1, pp. 12–27, Jul. 2005.

[134] S. P. Palecek, J. C. Loftus, M. H. Ginsberg, D. A. Lauffenburger, and A. F. Horwitz, "Integrin-ligand binding properties govern cell migration speed through cell-substratum adhesiveness.," *Nature*, vol. 385, no. 6616, pp. 537–40, Mar. 1997.

[135] C. Christophis, K. Sekeroglu, G. Demirel, I. Thome, M. Grunze, M. C. Demirel, and A. Rosenhahn, "Fibroblast adhesion on unidirectional polymeric nanofilms.," *Biointerphases*, vol. 6, no. 4, pp. 158–63, Dec. 2011.

[136] C. A. R.-K. Shawn P. Carey, Jonathan M. Charest, "Forces During Cell Adhesion and Spreading: Implications for Cellular Homeostasis," in *Cellular and Biomolecular Mechanics and Mechanobiology*, vol. 4, A. Gefen, Ed. Berlin, Heidelberg: Springer Berlin Heidelberg, 2011.

[137] T. D. Pollard and G. G. Borisy, "Cellular motility driven by assembly and disassembly of actin filaments.," *Cell*, vol. 112, no. 4, pp. 453–65, Feb. 2003.

[138] X. D. Ren, W. B. Kiosses, D. J. Sieg, C. A. Otey, D. D. Schlaepfer, and M. A. Schwartz, "Focal adhesion kinase suppresses Rho activity to promote focal adhesion turnover.," *J. Cell Sci.*, vol. 113 (Pt 2, pp. 3673–8, Oct. 2000.

[139] E. A. Codling, M. J. Plank, and S. Benhamou, "Random walk models in biology.," *J. R. Soc. Interface*, vol. 5, no. 25, pp. 813–34, Aug. 2008.

[140] D. Selmeczi, L. Li, L. I. I. Pedersen, S. F. Nrrelykke, P. H. Hagedorn, S. Mosler, N. B. Larsen, E. C. Cox, and H. Flyvbjerg, "Cell motility as random motion: A review," *Eur. Phys. J. Spec. Top.*, vol. 157, no. 1, pp. 1–15, Apr. 2008.

[141] L. Li, S. F. Nørrelykke, and E. C. Cox, "Persistent cell motion in the absence of external signals: a search strategy for eukaryotic cells.," *PLoS One*, vol. 3, no. 5, p. e2093, Jan. 2008.

[142] D. Selmeczi, S. Mosler, P. H. Hagedorn, N. B. Larsen, and H. Flyvbjerg, "Cell motility as persistent random motion: theories from experiments.," *Biophys. J.*, vol. 89, no. 2, pp. 912–31, Aug. 2005.

[143] A. Czirók, K. Schlett, E. Madarász, and T. Vicsek, "Exponential Distribution of Locomotion Activity in Cell Cultures," *Phys. Rev. Lett.*, vol. 81, no. 14, pp. 3038–3041, Oct. 1998.

[144] A. Upadhyaya, J.-P. Rieu, J. A. Glazier, and Y. Sawada, "Anomalous diffusion and non-Gaussian velocity distribution of Hydra cells in cellular aggregates," *Phys. A Stat. Mech. its Appl.*, vol. 293, no. 3–4, pp. 549–558, Apr. 2001.

[145] R. J. McMurray, N. Gadegaard, P. M. Tsimbouri, K. V Burgess, L. E. McNamara, R. Tare, K. Murawski, E. Kingham, R. O. C. Oreffo, and M. J. Dalby, "Nanoscale surfaces for the long-term maintenance of mesenchymal stem cell phenotype and multipotency.," *Nat. Mater.*, vol. 10, no. 8, pp. 637–44, Aug. 2011.

[146] P. Bianco, "Bone and the hematopoietic niche: a tale of two stem cells.," *Blood*, vol. 117, no. 20, pp. 5281–8, May 2011.

[147] F. M. Watt, "Out of Eden: Stem Cells and Their Niches," *Science (80-.).*, vol. 287, no. 5457, pp. 1427–1430, Feb. 2000.

[148] X. Zhu, M. Ohtsubo, R. M. Böhmer, J. M. Roberts, and R. K. Assoian, "Adhesion-dependent cell cycle progression linked to the expression of cyclin D1, activation of cyclin E-cdk2, and phosphorylation of the retinoblastoma protein.," *J. Cell Biol.*, vol. 133, no. 2, pp. 391–403, Apr. 1996.

[149] D. . Meredith, G. R. Owen, I. ap Gwynn, and R. . Richards, "Variation in cell–substratum adhesion in relation to cell cycle phases," *Exp. Cell Res.*, vol. 293, no. 1, pp. 58–67, Feb. 2004.

[150] D. Lü, C. Luo, C. Zhang, Z. Li, and M. Long, "Differential regulation of morphology and stemness of mouse embryonic stem cells by substrate stiffness and topography.," *Biomaterials*, vol. 35, no. 13, pp. 3945–55, Apr. 2014.

[151] G. Keller, "Embryonic stem cell differentiation: emergence of a new era in biology and medicine.," *Genes Dev.*, vol. 19, no. 10, pp. 1129–55, May 2005.

[152] Y.-H. Loh, Q. Wu, J.-L. Chew, V. B. Vega, W. Zhang, X. Chen, G. Bourque, J. George, B. Leong, J. Liu, K.-Y. Wong, K. W. Sung, C. W. H. Lee, X.-D. Zhao, K.-P. Chiu, L. Lipovich, V. A. Kuznetsov, P. Robson, L. W. Stanton, C.-L. Wei, Y. Ruan, B. Lim, and H.-H. Ng, "The Oct4 and Nanog transcription network regulates pluripotency in mouse embryonic stem cells.," *Nat. Genet.*, vol. 38, no. 4, pp. 431–40, Apr. 2006.

[153] J. Nichols, B. Zevnik, K. Anastassiadis, H. Niwa, D. Klewe-Nebenius, I. Chambers, H. Schöler, and A. Smith, "Formation of pluripotent stem cells in the mammalian embryo depends on the POU transcription factor Oct4.," *Cell*, vol. 95, no. 3, pp. 379–91, Oct. 1998.

[154] D. R. Soprano, B. W. Teets, and K. J. Soprano, "Role of retinoic acid in the differentiation of embryonal carcinoma and embryonic stem cells.," *Vitam. Horm.*, vol. 75, pp. 69–95, Jan. 2007.

[155] W. Chen, W. Jia, K. Wang, Q. Zhou, Y. Leng, T. Duan, and J. Kang, "Retinoic acid regulates germ cell differentiation in mouse embryonic stem cells through a Smad-dependent pathway.," *Biochem. Biophys. Res. Commun.*, vol. 418, no. 3, pp. 571–7, Mar. 2012.

[156] E. K. F. Yim, E. M. Darling, K. Kulangara, F. Guilak, and K. W. Leong, "Nanotopography-induced changes in focal adhesions, cytoskeletal organization, and mechanical properties of human mesenchymal stem cells.," *Biomaterials*, vol. 31, no. 6, pp. 1299–306, Feb. 2010.

[157] E. H. Ahn, Y. Kim, Kshitiz, S. S. An, J. Afzal, S. Lee, M. Kwak, K.-Y. Suh, D.-H. Kim, and A. Levchenko, "Spatial control of adult stem cell fate using nanotopographic cues," *Biomaterials*, vol. 35, no. 8, pp. 2401–2410, 2014.

[158] M. J. Dalby, M. O. Riehle, H. Johnstone, S. Affrossman, and A. S. G. Curtis, "Investigating the limits of filopodial sensing: a brief report using SEM to image the interaction between 10 nm high nano-topography and fibroblast filopodia.," *Cell Biol. Int.*, vol. 28, no. 3, pp. 229–36, Jan. 2004.

[159] W. A. Loesberg, J. te Riet, F. C. M. J. M. van Delft, P. Schön, C. G. Figdor, S. Speller, J. J. W. A. van Loon, X. F. Walboomers, and J. A. Jansen, "The threshold at which substrate nanogroove dimensions may influence fibroblast alignment and adhesion.," *Biomaterials*, vol. 28, no. 27, pp. 3944–51, Sep. 2007.

[160] M. J. Dalby, A. Hart, and S. J. Yarwood, "The effect of the RACK1 signalling protein on the regulation of cell adhesion and cell contact guidance on nanometric grooves.," *Biomaterials*, vol. 29, no. 3, pp. 282–9, Jan. 2008.